Current Reports on Science and Technology

(A Peer Reviewed Research Journal)

Faculty of Sciences
Khalsa College Amritsar

Current Reports on Science and Technology

(A Peer Reviewed Research Journal)
Bi –Annual

ISSN : 2455-023X

Subscription

Life Member	: Rs. 1500/-
Five Years	: Rs. 750/-
Per Copy	: Rs. 125/-

For Subscription write to :
Librarian, Khalsa College Amritsar
Email : chiefeditorjpas@gmail.com, Ph: +91 183 2258097, Fax : +91 183 2255619

Current Reports on Science and Technology Published by Faculty of Sciences, Khalsa College Amritsar and printed at Printwell 146, Focal Point, Amritsar

Current Reports on Science and Technology

(A Peer Reviewed Research Journal)
Bi-Annual

Volume – 03 January - December 2017

Contents

Curr. Rep. Sci. & Tech. 3 (2017) 1-8

Isotopic Fractionation in Atmospheric Water Vapour at 0ºC

Pooja Devi[1]*, A.K. Jain*[2]*, M.S. Rao*[3]*, and Rajan Saini*[4]
[1]*Department of Applied Physics, Gaini Zail Singh Campus College of Engineering & Technology, Bathinda*
[2]*Department of Physics, Indian Institute of Technology, Roorkee -247667*
[3]*National Institute of Hydrology, Roorkee-247667*
[4]*Post Graduate Department of Physics, Khalsa College Amritsar -143005*
pujaiitr09@gmail.com

Abstract

Two method were used to sample atmospheric moisture- ground level water vapour at 0ºC: Liquid Condensation (LC) and Cryogenic Trap (CT) for the complete year 2012 to observe the stable isotopic effects in atmospheric water vapour. Results were also compared with isotopic signature of water vapour at −80ºC. The results show that $\delta_{18}O_{Liquid}$-CT and $\delta_{2}H_{Liquid}$-CT values were enriched in heavy water isotopes than those of the $\delta_{18}O_{Vapour}$ and $\delta_{2}H_{Vapour}$, while $\delta_{18}O_{Liquid}$-LC values showed depleted nature of heavy water isotopes than $\delta_{18}O_{Vapour}$. Also, the slopes and intercepts of moisture sampled at 0ºC by LC and CT methods suggest that cryogenic trap method at 0ºC should be preferred over liquid condensation method where cryogenic trapping of water vapours −80ºC is not feasible. Cryogenic trap method at 0ºC provides better results and less diffusive fractionation than liquid condensation 0ºC.

Keywords: cryogenic trap, liquid condensation, water isotopes, atmospheric moisture, diffusive fractionation.

I. Introduction

Atmospheric moisture contributes about 10^{-5} of the ocean water mass, which can be considered approximately as the total amount of water on the earth's surface [1]. The vertical distribution and amount of water vapour content in various parts of the atmosphere is profoundly affected by temperature of atmosphere. The precipitation arises from the uplifting of an air mass. It continues to cool down till the dew point due to adiabatic expansion. If sufficient number of condensation nuclei are present, cloud droplet formation occurs which is supposed to be in local isotopic equilibrium with the moisture in the warmer part of cloud due to fast exchange between the droplets and air moisture. However, in the colder part, further isotope fractionation takes place as the isotopic vapour molecules diffuse into the solid ice particles [2]. This may remain preserved in the frozen clouds, not subjected to the isotope exchange. As the droplets combine and begin to fall on the ground against the rising air, additional isotope exchange occurs which further enhances the fractionation between liquid and gaseous phase.

So far as atmospheric moisture is concerned, precipitation in terms of its heavy isotopic species has been intensively studied. Dansgaard [3] has reviewed some important features about the isotopic variations in precipitation on a global scale, assuming that evaporation and condensation in nature proceed as Rayleigh distillation and condensation processes. Eriksson (1965) made some attempts to express the isotopic concentrations in precipitation as a function of atmospheric processes which transport atmospheric moisture. However, due to lack experimental data on the isotopic nature of atmospheric vapour, these ideas remained more or less speculative. Later much interest has again been focused on the transport of atmospheric water vapour [4], and its impact on the isotopic composition of precipitation, atmospheric vapour and local climate. Also, much interest has been devoted to the study of ^{18}O in atmospheric moisture, not only in order to study the atmospheric transport processes but also to understand the effect of isotopic exchange between atmosphere and evaporating bodies. Thus, the stable isotopic study of the atmospheric water vapour can be an effective tracer to get microphysical information of cloud formation processes as isotopic fractionation is very sensitive to the phase changes.

In order to trace the short-term variations of ^{18}O and ^{2}H in atmospheric vapour, a suitable method promising a continuous sampling of the vapour is needed. Since any loss of vapour will cause an isotopic fractionation of the condensed mass, therefore, it is also required that a given mass of vapour should be condensed completely. For this purpose, atmospheric moisture is cryogenically trapped at very low (−80ºC) that requires continuous liquid nitrogen supply. It makes sampling process quite expensive and tedious. As an alternative, liquid condensation at 0ºC is being used for few Indian studies. But LC method suffers fractionation during liquid to vapour phase process. With this in consideration, the water vapours in the ambient moisture were also sampled concurrently with the help of cryogenic trapping (at 0ºC) at National Institute of Hydrology (NIH), Roorkee, India and results were compared with cryogenically trapped at 80ºC.

II. Experimental

a) Liquid Condensation Method

The air moisture rapidly condenses as it interacts with a colder surface. The water vapours present in the air moisture were condensed partially on an ice-cooled conical outer surface of aluminium (Al) cone. Ice-cubes were filled in the Al cone and covered with by a polyvinyl chloride (PVC) lid subsequently. A 10ml plastic bottle then was kept in a hole, on the base plate of Al stand. The Al cone was held firmly in the vertical position using the adjustable screws in the stand such that the liquid that condenses on its outer surface fell directly drop wise into the plastic bottle. To reduce the evaporation rate in this process, the tip of Al cone was held exactly above the tip of the plastic bottle. The sampling time was kept from 30−45min subjected on the dew point, in order to collect ~10ml of liquid at ~0ºC. The temperature of the ice and melt in the Al cone was found to lie in the range 0−0.5ºC during the sampling period. The sample collection time was kept from 9:30am till the sample amount reached 8−10ml. The liquid condensate so collected is simply termed as 'Liquid-LC' at 0ºC [5].

b) Cryogenic Trap Method

The ambient atmospheric moisture was concurrently sampled by passing air through the glass condensers using aquarium pump. The glass condensers were pre-cooled at 0ºC by filling the ice cubes and −80ºC using a slush of Methanol + LN2 inside the two Dewar flasks. In order to get fractionation free vapour sample, the air-flow through the glass condenser was kept at nearly 750ml/min. With the average air temperature of ~22ºC (ranging from 11−33ºC) and average relative humidity of ~66% (ranging from 37−95%) during the experimental time, 4−5hrs were requisite to sample ~2ml of the liquefied vapour. The sampling time was kept from 9:30am to 3:30pm twice a week during the year 2012. After water vapour was frozen, the ends of glass condenser were closed and it was allowed to melt at room temperature. The liquefied vapour was subsequently filled in the sample bottles, which were then stored for isotopic analysis. For this purpose, the atmospheric moisture samples so collected at 0ºC are termed as 'Liquid-CT' and −80ºC as 'Vapour' [6]. Data on the daily average air temperature and relative humidity were also recorded from meteorological observatory at NIH Roorkee.

c) Isotopic Analysis

The isotopic analyses ($\delta^{18}O$ and $\delta^{2}H$) of collected moisture samples were carried out at the NIH, Roorkee, by standard equilibration method [7]. The $^{2}H/^{1}H$ ratios were measured by using a dual inlet isotope ratio mass spectrometer (IRMS), whereas $^{18}O/^{16}O$ ratios were measured with a continuous flow-IRMS. The results were expressed by convention as parts per thousand deviations from the Vienna Standard Mean Ocean Water (VSMOW), and the formula is as follows:

$$\delta_{sample} = \left(\frac{R_{sample}}{R_{VSMOW}} - 1\right) \times 1000\ ‰$$

where R is the ratio of $^{2}H/^{1}H$ or $^{1}8O/^{16}O$ measured in sampled water or V-SMOW. The reproducibility of measurements was better than ±0.1 ‰ for $\delta^{18}O$ and ±1 ‰ for $\delta^{2}H$.

III. Results and Discussion

a) Temporal variations of $\delta^{18}O$ and $\delta^{2}H$ in Liquid-LC and vapour

The time series of $\delta^{18}O$ and $\delta^{2}H$ values of moisture sampled by liquid condensation and cryogenic trapping at 0ºC and −80ºC are plotted in Fig. 1 & 2, respectively. According to basic isotope systematics, the water in liquid phase in equilibrium with vapor phase is expected to be isotopically enriched. Contrary to theory, the $\delta^{18}O_{Liquid}$-LC values from our experiment were observed to be depleted than those of the $\delta^{18}O_{Vapour}$ as shown in Fig.1. However, $\delta^{2}H_{\ Liquid}$-LC values were enriched than those of the $\delta^{18}O_{Vapour}$ throughout the experimental period as shown in Fig.2 in accordance to the theory.

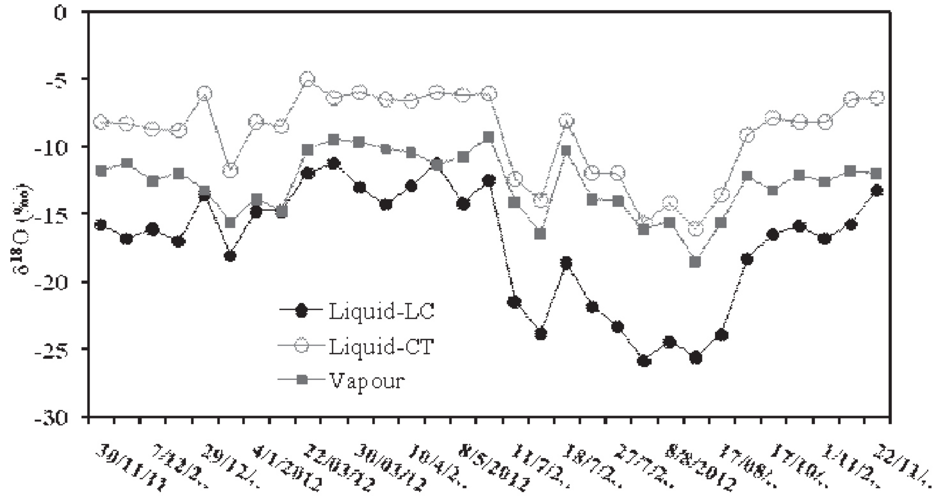

Fig 1. Time series of •18O of atmospheric moisture collected by Liquid Condensation (LC) and by Cryogenic Trapping (CT) at 0 ºC and −80º C, respectively.

Many peaks in $\delta^{18}O$ and δ^2H for both liquid and vapour shows isotopic seasonal effect related to sudden changes in ambient relative humidity. It is also indicated by the fact that difference $\Delta^{18}O = \delta^{18}O_{Liquid\text{-}LC} - \delta^{18}O_{Vapour}$ becomes gradually more negative with increase in saturation index, while the difference $\Delta^2H = \delta^2H_{Liquid}$-LC δ^2H_{Vapour} decreases during rainy period (July-Sept.). The saturation index expresses the extent of water vapor saturation in the air at the condensation surface. Our results agrees well with precious studies [6, 8].

b) Temporal variations of $\delta^{18}O$ and δ^2H in Liquid-CT and vapour

The time series of $\delta^{18}O$ and δ^2H values of moisture sampled by cryogenic trapping at 0ºC and −80ºC are plotted in Fig. 1 & 2, respectively. Interestingly, in accordance with equilibrium fractionation theory, the $\delta^{18}O_{Liquid}$-CT and δ^2H_{Liquid}-CT values from our experiment were found to be enriched in heavy water isotopes than those of the $\delta^{18}O_{Vapour}$ and δ^2H_{Vapour} shown in Fig. 1 & 2, respectively. More negative peak values of $\delta^{18}O_{Liquid}$-CT and δ^2H_{Liquid}-CT during monsoon period show presence of high relative humidity. Also the differences $\Delta^{18}O = \delta^{18}O_{Liquid\text{-}LC} - \delta^{18}O_{Vapour}$ and $\Delta^2H = \delta^2H_{Liquid\text{-}LC} - \delta^2H_{Vapour}$ reduced with increase in saturation index during rainy season.

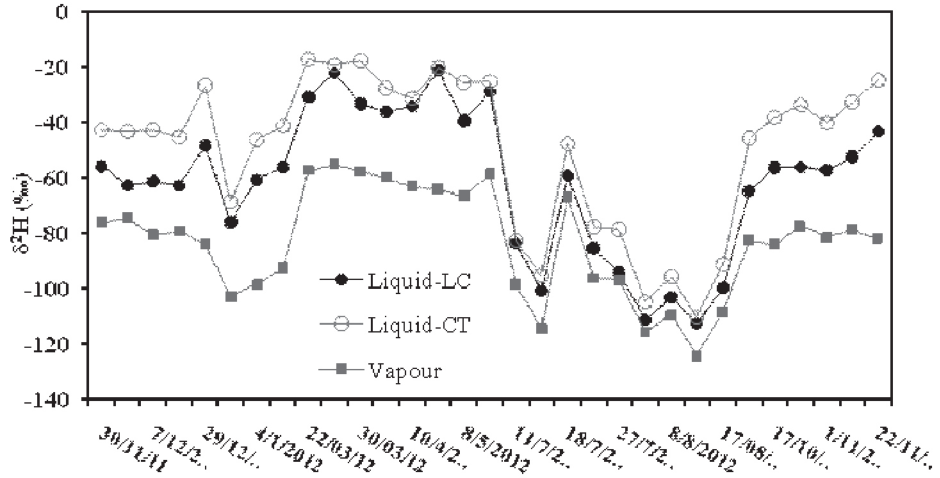

Fig 2. Time series of δ^2H of atmospheric moisture collected by LC and CT methods at 0 ºC and −80 ºC, respectively.

The $\delta^{18}O-\delta^2H$ relations for liquid-LC&CT and vapour are shown in Fig.3. The local meteoric water line (LMWL) has also been plotted [9] for reference. According to Rayleigh distillation model, at a constant temperature under equilibrium conditions, the slopes as well as the intercepts of regression lines for vapour and subsequently generated liquid, are governed by the temperature of evaporation and condensation, respectively [10, 11]. While, the temperature of evaporation has a profound effect on the slope, the intercept can vary substantially with the temperature of condensation. The $\delta^{18}O-\delta^2H$ regression line for atmospheric vapour collected at −80ºC from our experimental study was found to have slope

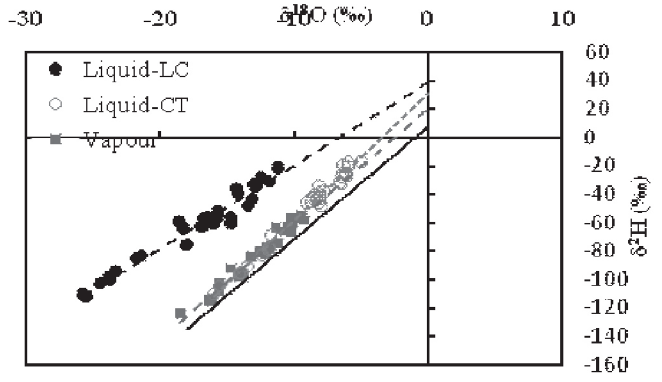

Fig 3. $\delta^{18}O-\delta^2H$ regression lines obtained for liquid-LC&CT and vapour. The solid line represents the LMWL.

(8.8) similar to LMWL (Table 1), while liquid-LC lesser has value of slope (5.8) than that of the vapor which indicates kinetic fractionation of water vapour in course of transportation of moisture from source region to the formation of clouds.

The high intercepts values of $\delta^{18}O-\delta^{2}H$ plot for vapour and that of the liquid condensate signify diffusive fractionation in both cases [11], however the extent of diffusive fractionation is less in case of moisture samples were taken by CT (30.7) method than LC (38.3) method at 0ºC.

Table 1. Regression equations for $\delta^{18}O-\delta^{2}H$ for liquid-LC&CT and vapour

Parameter	**$\delta^{18}O$ vs $\delta^{2}H$**
$Liquid_{LC}$ (0°C)	$\delta^{2}H = 5.81 * \delta^{18}O + 38.38$ ($R^2 = 0.96$; $n = 31$)
$Liquid_{CT}$ (0°C)	$\delta^{2}H = 8.89 * \delta^{18}O + 30.74$ ($R^2 = 0.98$; $n = 31$)
Vapour (−80°C)	$\delta^{2}H = 8.16 * \delta^{18}O + 20.14$ ($R^2 = 0.96$; $n = 31$)

This can be due to the fact that air flow rate through glass condenser was maintained low (~750ml/min) in cryogenic trap method that helped to condense moisture with less fractionation, whereas air flow rate was uncontrolled in case of liquid condensation method. This process is mostly found to depend upon the masses and, hence on the diffusivity of the isotopic molecules ($H_2{}^{18}O$, ${}^{1}H_1{}^{2}H_1{}^{16}O$) present in the system. During this, the diffusivity of the heavy isotopic molecule ($H_2{}^{18}O$, ${}^{1}H_1{}^{2}H_1{}^{16}O$) is lower than that of the lighter isotopic molecule (${}^{2}H^{16}O$), which results in the depletion of the heavier isotopes in the liquid condensate sampled by LC method.

IV. Conclusion

The $\delta^{18}O_{Liquid\text{-}CT}$ and $\delta^{2}H_{Liquid\text{-}CT}$ values from our experiment were found to be enriched in heavy water isotopes than those of the $\delta^{18}O_{Vapour}$ and $\delta^{2}H_{Vapour}$, while $\delta^{18}O_{Liquid\text{-}LC}$ values showed depleted nature of heavy water isotopes than $\delta^{18}O_{Vapour}$. Also, the slopes and intercepts of moisture sampled at 0ºC by LC and CT methods suggest that cryogenic trap method at 0ºC should be preferred over liquid condensation method where cryogenic trapping of water vapours −80ºC is not feasible. Cryogenic trap method at 0ºC provides better results and less diffusive fractionation than liquid condensation method.

V. Acknowledgments

Authors acknowledge the facilities provided by Hydrological Investigation Division of NIH, Roorkee, India for this study.

VI. References

[1] W.G. Mook, "Environmental isotopes in hydrological cycle: principles and applications" UNESCO/IAEA Series (2011).

[2] J. Jouzel and L. Merlivat, "Deuterium and oxygen-18 in precipitation: modelling of the isotopic effects during snow formation". J. Geophys. Res.89 (1984) 11749.

[3] W. Dansgaard, "Stable isotopes in precipitation" Tellus 16 (1964) 436-468.

[4] K. Rozanski and C. Sonntag, "Vertical distribution of deuterium in atmospheric water vapour" Tellus 34(1982) 135-141.

[5] R.D. Deshpande, A.S. Maurya, B. Kumar, A. Sarkar and S.K. Gupta, "Rain-vapor interaction and vapor source identification using stable isotopes from semiarid western India" J. Geophys. Res. 115 (2010) 3311.

[6] R.D. Deshpande, A.S. Maurya, B. Kumar, A. Sarkar and S.K. Gupta, "Kinetic fractionation of water isotopes during liquid condensation under super-saturated condition" Geochim. Cosmochim. Acta 100, (2013) 60-72.

[7] C.A.M. Brenninkmeijer and P.D. Morrison, "An automated system for isotopic equilibration of CO_2 and H_2O for ^{18}O analysis of water" Chem. Geol. 66 (1987) 21-26.

[8] P. Purushothaman, M.S. Rao, B. Kumar, Y.S. Rawat, G. Krishan and P. Devi, "Comparison of two methods for ground level vapour sampling and influence of meteorological parameters on its stable isotopic composition at Roorkee, India" Hydrol. Process. 28 (2014) 882-894.

[9] B. Kumar, S.P. Rai, K.U. Saravana, S.K. Verma, P. Garg, V.S.V. Kumar, R. Jaiswal, B.K. Purendra, S.K. Kumar, N.G. Pande, "Isotopic characteristics of Indian precipitation" Water Resour. Res. 46, (2010) W12548.

[10] I.D. Clark and P. Fritz, "Environmental isotopes in hydrogeology" Lewis Publishers, Boca-Raton, New York (1997) 57-58.

[11] J.R. Gat, "Isotope Hydrology: A Study of Water Cycle" London,

Curr. Rep. Sci. & Tech. 3 (2017) 9-13

Comparative Study of Lead Phosphate and Bismuth Borate Glasses Containing Sodium Tungstate as Gamma ray Shielding Materials

Mridula Dogra, K.J.Singh, Kulwinder Kaur, Vikas Anand and Parminder Kaur
Department of Physics, Guru Nanak Dev University, Amritsar143005, India
kanwarjitsingh@yahoo.com

Abstract :

The present work has been undertaken to study the correlation of gamma ray shielding properties of $PbO-P_2O_5-Na_2WO_4$ and $Bi_2O_3-B_2O_3-Na_2WO_4$ glasses. The selected compositions of glasseshave been prepared by conventional melt-quenching technique. Density has been measured by using Archimedes' principle. It is reported that density increases with increase in the content of heavy metal oxides PbO and Bi_2O_3 in glasses. XRD studies have been undertaken to confirm the amorphous nature of samples. Mass attenuation coefficient has been calculated at photon energies 662, 1173 and 1332 keV using XCOM computer software developed by National Institute of Standards and Technology. These values are further used to calculate half value layer parameter. The mass attenuation coefficient and half value layer are also compared with nuclear reactor shield 'barite concrete'. It has been analyzed from the results that the values of mass attenuation coefficient are greater for bismuth borate glasses than lead phosphate glasses at same photon energy. Thus, bismuth borate glasses containing sodium tungstate may be considered as potential candidates for gamma ray shielding glasses.

Keywords: Glass structure, Gamma Rays, Radiation effects

I. Introduction

Gamma rays are highly penetrating electromagnetic radiations in environment and long term exposure to these radiations can have harmful effects on humans. Concretes are commonly used as shielding material in nuclear reactors but they have various drawbacks [1]. Heavy metal oxides such as PbO, Bi_2O_3 etc. are one of the alternates that can be used for shielding purposes.Keeping this in view, the authors have studied the correlation of gamma ray shielding properties of PbO-P_2O_5 and Bi_2O_3-B_2O_3containing sodium tungstate in terms of mass attenuation coefficient and half value layer parameter. The shielding properties are further compared with barite concrete which is one of concretes commonly used in reactors [2].

II. Experimental Details

Glass samples of the composition xPbO-0.3P_2O_5-(0.7-x) Na_2WO_4 and x Bi_2O_3-0.6 B_2O_3-(0.4 - x) Na_2WO_4 where x = 0.10, 0.15 and 0.20 (in mole fraction) are prepared by melt quenching technique. AR grade chemicals of PbO, $NH_4H_2PO_4$, Bi_2O_3, H_3BO_3 and $Na_2WO_4.2H_2O$ are used to prepare the samples. $Na_2WO_4.2H_2O$,H_3BO_3 and $NH_4H_2PO_4$ are used as source material for Na_2WO_4, $B_2O_3$and P_2O_5component. 20g batch of each composition is mixed well in an agate mortar and then melted in porcelain crucible at 1123K for 2 h followed by annealing at 573K for 30 min. The chemical composition, density and molar volume are tabulated in Table 1.

III. Results and Discussion

a. Density and Molar Volume Studies

The densities of the prepared glassy samples have been determined by the simple Archimedes principle using benzene as an immersion liquid. Density shows an increasing trend for PbO-P_2O_5 and Bi_2O_3-B_2O_3 glasses which may be attributed to increase in mole fraction of heavy metal oxides PbO and Bi_2O_3 in the composition. Molar volume decreases for samples PbW1 to PbW3 and on the other hand, it increases for samples BiW4 to BiW6.This may be due to expansion in the oxide network caused by Bi_2O_3 as compared to compactness in the structure of lead based glasses.

b. XRD Studies

X-ray diffraction studies have been undertaken by BrukerD8 Focus diffractrometer. XRD patterns of prepared glass system do not show sharp

***Table1**.Chemical composition, density and molar volume of the prepared glass.*

Sample code	**Composition (mole fraction)**					**Density (g/cm^3)**	**Molar Volume (cm^3/mol)**
	PbO	**P_2O_5**	**Bi_2O_3**	**B_2O_3**	**Na_2WO_4**		
PbW1	0.10	0.30	-	-	0.60	4.47	68.32
PbW2	0.15	0.30	-	-	0.55	4.52	66.38
PbW3	0.20	0.30	-	-	0.50	4.73	62.31
BiW4	-	-	0.10	0.6	0.3	5.47	34.24
BiW5	-	-	0.15	0.6	0.25	5.49	35.35
BiW6	-	-	0.20	0.6	0.2	5.57	36.07

peaks indicating the absence of crystalline nature as shown in Figure 1. This confirms the amorphous nature of the glasses.

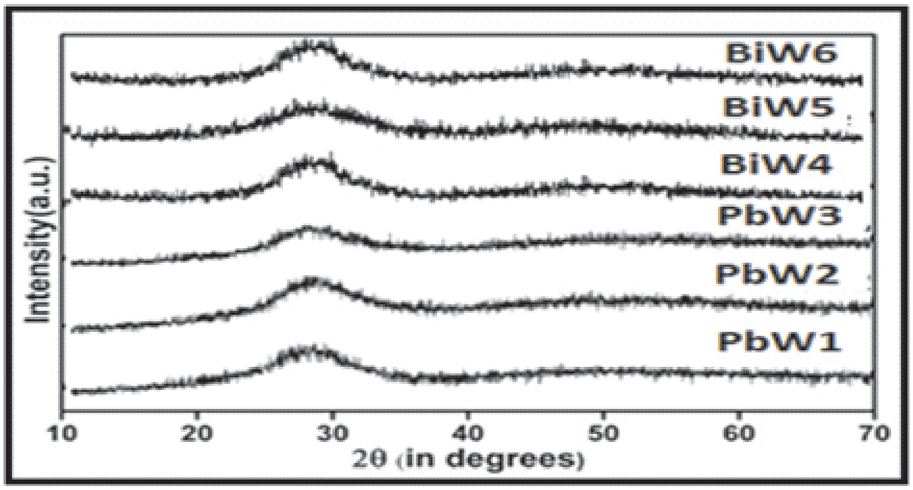

Fig 1.XRD patterns of investigated samples.

c. Gamma Ray Shielding Properties

The values of mass attenuation coefficient are calculated by using XCOM software developed by NIST [3] at photon energies 662, 1173 and 1332 keV. The variation of mass attenuation coefficient with PbO and Bi_2O_3 are shown in Figures 2 and 3. It is seen from the graph that our investigated samples show better results than barite concrete which is considered to be the best radiation shield [4]. Bi_2O_3-B_2O_3-Na_2WO_4 show better values of mass attenuation coefficient in comparison to PbO-P_2O5-Na_2WO_4. The half value layer parameters are measured using density values. These values are also compared with barite concrete at photon energies 662, 1173 and 1332 keV. HVL parameter decreases with increasing mole fraction of Pb and Bi in the glass samples and its values are lower than barite concrete as shown in Figures 4 and 5. HVL of Bi_2O_3-B_2O_3-Na_2WO_4 is lower than PbO-P_2O_5-Na_2WO_4 glasses. Thus, it may be assumed that lesser thickness is required for attenuation of gamma radiations for bismuth based glasses as compared to lead based glass composition.

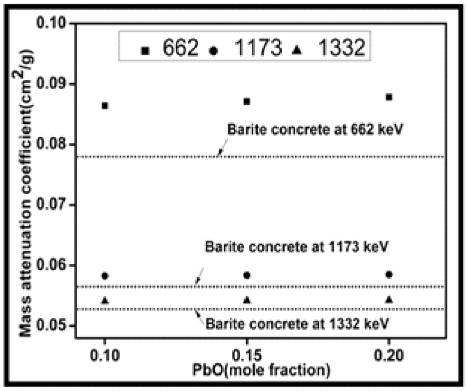

Fig2.Variation of mass attenuation coefficient with PbO

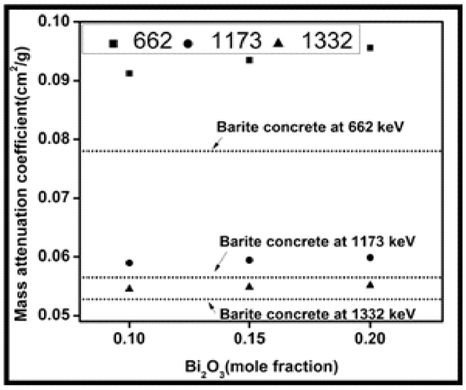

Fig3.Variation of mass attenuation coefficient with Bi2O3

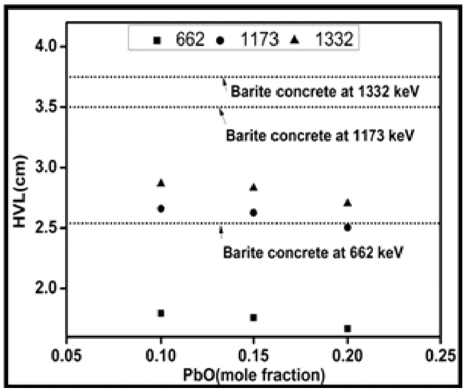

Fig4.Variation of HVL with PbO .

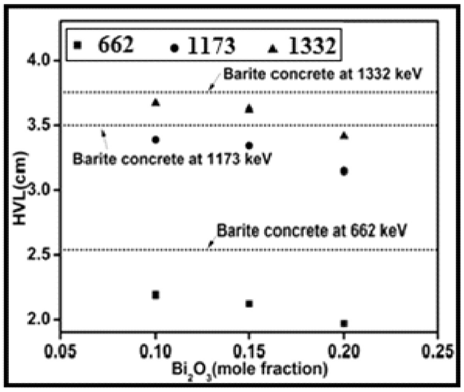

Fig5.Variation of HVL with Bi_2O_3

Gamma-ray shielding properties in terms of mass attenuation coefficient and HVL parameter are better for PbO-P_2O_5-Na_2WO_4 and Bi_2O_3-B_2O_3-Na_2WO_4 than barite concrete. It has been observed that bismuth containing glasses are better than lead based glasses as bismuth based glasses possess higher density, higher mass attenuation coefficient and lower HVL values. Moreover, lead is toxic in nature and its replacement by bismuth in glasses is beneficial to develop environment friendly commercial nuclear reactor shield.

III. Acknowledgements

The authors Kulwinder Kaur and Parminder Kaur are grateful to the financial assistance provided by the Department of Science and Technology, New Delhi (India) through INSPIRE program [IF-120620]and UGC(UPE program) respectively.

IV. References

[1]. Lee, C.-M., Lee, Y.H., Lee, K.J., Cracking effect on gamma-ray shielding performance in concrete structure. Progress in Nuclear Energy49(2007) 303-312.

[2]. K. Kaur, K. J. Singh and V. Anand, Correlation of gamma ray shielding and structural properties of $PbOBaOP_2O_5$ glass system Nucl. Eng. Design 285(2015), 31-38.

[3]. Gerward, L., Guilbert, N., Jensen, K.B., Levring, H., WinXCom-a program for calculating X-ray attenuation coefficients. Radiation physics and chemistry71(2004) 653-654.

[4]. N. Singh, K.J.Singh, K.Singh and H.S Singh, Nuclear Instruments and Methods in Physics Research B225 (2004) 305309.

Curr. Rep. Sci. & Tech. 3 (2017) 14-19 © Khalsa College Amritsar

Analysis of Variation in Activation Energies for Gamma Irradiated Overhead projector Sheet

Neerja[a], *Sameer Kalia*[a] *Meetu Singh*[b], *Surinder Singh*[c]
[a]*Department of Physics, DAV College, Amritsar-143001, India.*
[b]*Department of Applied Sciences, I K Gujral Punjab Technical University, India.*
[c]*Department of Physics, Guru Nanak Dev University, Amritsar-143005, India.*
neerjakalia@yahoo.co.in

Abstract

Here in the present study, an attempt has been made to analyze the effects of gamma irradiation on track registration properties of overhead projector sheet (with average thickness 100µm) as solid state nuclear track detector, exposed to different gamma doses from 0-500 kGy. The changes in the bulk and track etch rates (VB, VT) as well as sensitivity (S), due to gamma irradiation using 6.25N NaOH solution as an etchant at different temperatures (323-353 K) are discussed on the basis of degradation and cross-linking mechanisms. From these measured values of bulk and track etch rates, the activation energies associated with them (EB, ET) have also been calculated.

Keywords: Overhead projector sheet, Gamma irradiation, Etching rates, Sensitivity, Activation Energy.

I. Introduction

Presently, extensive efforts are being made to investigate the modifications induced by ionizing particles/radiations like electrons, ions and photons in various track detectors. Out of these various track detectors, the polymers have been found to be more sensitive. So the importance of polymers has increased significantly because of the their scope of utilization in several diversified research fields.[1,2]. Although a lot of studies have been already done on various polymers irradiated by gamma rays, yet in the present work an attempt has been made to study the modifications induced by gamma-rays on various track registration properties of overhead projector sheet [3-6]. Here we have observed the influence of gamma-rays of Co-60 source with energies in the order of

1.17 and 1.35MeV on overhead projector sheet. This work may be helpful in understanding the track registration response of this polymer after gamma irradiation for its potential use as a solid state nuclear track detector.

II. Experimental details

The polymer in the form of sheet with average thickness 100µm procured from Garware Pvt. Ltd. Mumbai has been used. Basu et. al. in 2005[7] observed that this overhead projector sheet has same structure as PET as given in Figure 1.

The small samples of this polymer were irradiated with different gamma doses from BARC, Trombay, Mumbai using Co-60 as a gamma source. These samples were irradiated repeatedly in order to achieve various doses between 0.5 to 500kGy. Further, these samples were exposed with Cf-252 source to record fission tracks in 2π geometry. Afterwards, exposed samples were etched in 6.25N NaOH solution at different temperatures ranging 323-353K for optimized time intervals. After each etching the bulk etch rate VB and track etch rate VT were measured [8,9]. The activation energies associated with etching rates were determined by Arrhenius equation.

$$VB\ (VT) = A\ \mathrm{Exp}\ (-EB\ (ET)/kT) \qquad (1)$$

where T is a constant , EB(ET) is the activation energy for bulk (and track), k is Boltzmann constant .

III. Results and Discussion

To investigate the effect of gamma dose on the various track registration properties of the detector, the bulk etch and track etch rate of gamma- irradiated samples are compared with un-irradiated sample. The data reveals that there is an increase in both bulk and track etch rates with γ-irradiation (Table 1 and 2). This increase in etching rates with gamma dose may be due to decrease in molecular weight by chain scissioning of the polymeric molecules by γ-irradiation which increase the dissociation rates. In order to calculate the activation energies associated with bulk and track etch rates we have plotted logVB (VT) against the inverse of absolute

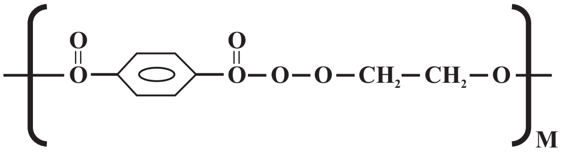

Figure 1: PET Monomer Unit (Here M ranging from 20,000- 40,000)

temperatures for unirradiated and gamma irradiated samples (figures 2 &3).

The values of activation energies for un-irradiated and gamma irradiated samples are given in Table 3. A decrease in activation energies have been observed which indicates the scissioning in gamma irradiated samples. The sensitivity, S, is calculated (=VB /VT) and it has been found that sensitivity has decreased at higher gamma doses at a particular temperature (Table 4). The same type of trend has been reported Portwood and Henshaw[10] and Singh and Neerja [11] for CR-39 track detectors.

Table 1. The variation of the bulk etch rate VB with gamma dose at different temperatures in case of overhead projector sheet.

Temp. (K) → **Dose (kGy)↓**	323	333	343	353
0	0.77±0.02	1.15±0.05	2.31±0.09	8.27±0.34
0.5	0.81±0.02	1.35±0.05	2.40±0.12	8.30±0.35
1	0.85±0.03	1.57±0.04	2.47±0.06	8.47±0.28
10	0.84±0.02	1.95±0.05	2.45±0.09	8.78±0.23
500	1.05±0.03	2.75±0.14	3.55±0.09	8.91±0.24

Table 2. The variation of the track etch rate VT with gamma dose at different temperatures in case of overhead projector sheet.

Temp. (K) → Dose (kGy)↓	323	333	343	353
0	5.19±0.14	11.61±0.49	17.5±0.50	44.12±1.16
0.5	5.35±0.15	11.70±0.33	17.8±0.62	44.80±1.20
1	5.55±0.13	11.74±0.41	21.02±0.73	44.25±1.90
10	6.02±0.16	15.73±0.45	22.33±0.75	45.2±1.13
500	6.25±0.26	17.43±0.66	23.82±0.71	45.51±1.27

Table 3.

-Dose(kGy)	E_B(eV)	E_T (eV)
0	0.76	0.67
0.5	0.73	0.66
1	0.71	0.66
10	0.71	0.63
500	0.65	0.61

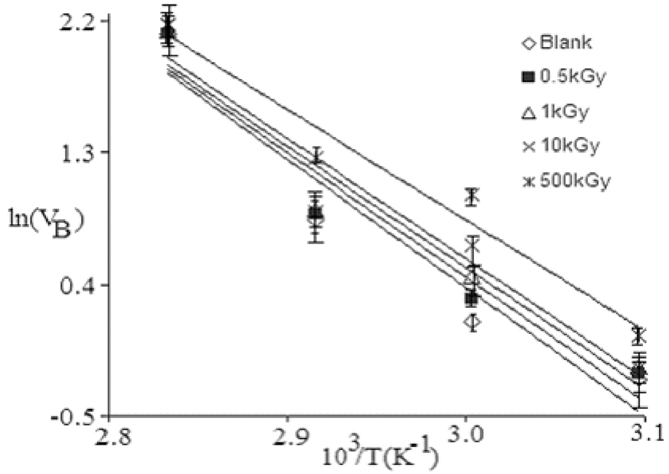

Figure 2 shows the variation of bulk etch rate with respect to temperature for OHP sheet detector

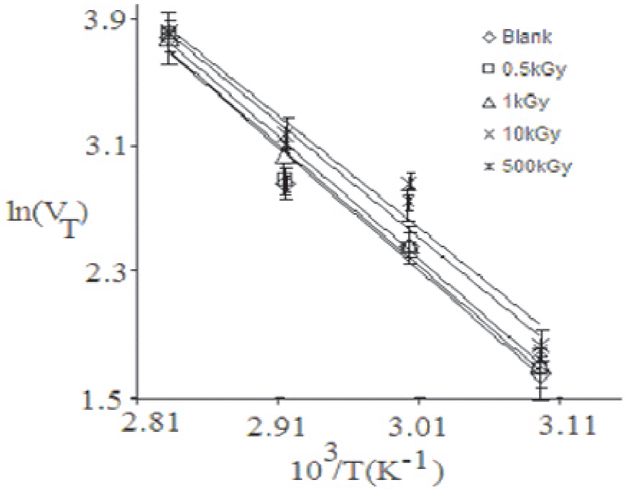

Figure 3 shows the variation of track etch rate with respect to temperature for OHP sheet detector

Table 4. The variation of the sensitivity for different gamma dose at different temperatures in case of overhead projector sheet

-Dose (kGy) → Temp. (K) ↓	. $S=V_T/V_B$				
	Blank	0.5	1	10	□̃
323	6.74	6.60	6.52	7.16	5.95
333	10.09	8.66	7.54	8.06	6.33
343	7.57	7.41	7.20	9.11	6.70
353	5.33	5.39	9.18	5.14	5.10

IV. Conclusions

On the basis of present study, it can be concluded that both bulk and track rates increase with gamma dose whereas the activation energy associated with these bulk and track etch rates decrease with gamma doses which can be explained on the basis of chain scission of the detector due to gamma-irradiation.

V. Acknowledgements

Authors are thankful to the BARC, Mumbai for providing irradiation facilities.

VI. References

[1] Durrani S.A. and Bull,R.K. 1987. Solid State Nuclear Track Detection, 1st ed. Pergamon Press, UK, Chapter 4:48.

[2] Fleischer, R.L. and Price P. B., Walker, R. M., 1975. Nuclear Tracks in solids: Principles and Applications, 1st ed. University of California Press, Berkeley, California.

[3] Kalsi, P.C. , Nadkarni, V.S and Manchanda, V.K.,2008.Radiation Physics and Chemistry 77:1002-1004.

[4] Chavan, V., Kalsi, P.C. and Mhatre, A., 2011. J Radioanal Nucl Chem 287:273-276.

[5] Singh, S and Neerja.,2006. Radi. Effects and defects in solids 161:6,377-381.

[6] Neerja, Kalia, S., Kaur,J., Kuma, S.,and Singh, S., Polymer-Plastics Technology and Engineering, 53:5, 526-530.

[7] Basu,B., Fischer,B., Mazumdar, A., Raha,S., Saha,S., Saha, S.K. and Syam,D., 2005. Indian J. Phys. 79:279 (2005).

[8] Fleischer, R.L., Price P. B. and Woods, R. T. 1969. Phys. Rev. 88:563.

[9] Torreles J., Baixeras C., Damongo C., Ferrandaz F. and Vidal Quadras A., 1988. Nucl. Tracks. Radiat. Meas. 15(1-4):183-186.

[10] Henshaw D.L., Griffiths N., Landen O.A.L. and Benton E. V., 1981. Nucl. Instrum. Methods, 180: 65-77.

[11] Neerja and Singh, S,.2007.Radia.Meas. 42:1507-1509.

Curr. Rep. Sci. & Tech. 3 (2017) 20-28

Radon/Thoron Exhalation Rate in Soil of Three Regions of Punjab, India, by using Active Monitor

Sumit Sharma[a], Lovepreet Kaur[a], Sapna[a], Rohit Mehra and Ajay Kumar[a]
[a]Department of Physics, DAV College, Amritsar, Punjab, India
[a]Department of Physics, Dr. B. R. Ambedkar National Institute of Technology, Jalandhar 144001, Jalandhar, Punjab, India
ajay782@rediffmail.com

Abstract

Measurement of Radon and thoron exhalation rate in three regions- Amritsar, Batala and Gurdaspur of Punjab, India has been carried out. 15 soil samples have been selected randomly for the analysis. Five samples were received from each region. The exhalation rate was measured of selected samples by using Smart RnDuo monitor (Made by BARC, Mumbai). The obtained exhalation rates were compared with geology of the region. Correlation of radon and thoron exhalation rates has also been measured. The geology was, therefore, considered to be an important source to explain the difference among exhalation rates. The results obtained are presented in the Table.

Keywords: Radon, Thoron, Soil, Smart RnDuo monitor.

I. Introduction

Soil is an accumulation of natural bodies (organic, inorganic and radionuclide's) on the surface of earth. Naturally occurring radionuclide's (uranium and thorium series, etc.) are the largest contributor to radiation dosages received by people. Radon and thoron generates from Urainium-238 and thorium-232, exist in all types of soil and rocks. The radon concentration in the ground relies on upon the radium content and the permeability of the soil and emanation power of the soil and rock [1-4]. Radon and thoron exude predominantly from the earth surface through the gap in soil to the air. The rate at which radon and thoron escapes from soil into the surrounding air is known as exhalation rate of the soil into the atmosphere [5].

Radon and thoron exhalation rate is influenced by ecological factors, such as weather element, water content and topography. The distinction of geographical distribution and soil component in the crustal layer may influence the exhalation rate [4]. The estimation of radon exhalation rate in soil is useful to study radon health hazards [6]. Some building materials might be responsible for increased indoor radon levels either because of their higher radon exhalation rates or due to their uranium/radium enrichment as compared to other materials depending on their micro-structure [7, 8]. Exhalation of radon (222Rn) and thoron (220Rn) from soil is of interest since the short-lived decay products of radon are the greatest contributors to the lung dose of inhaled radionuclides [9].

Monitoring of the hazardous effects of exhalation on human health, it was necessary to conduct measurements of radon and thoron content in the soil. Higher values of 226Ra in soil contribute significantly in the enhancement of environmental radon. However, radon exposure shows an extreme variation from location to location and depends primarily on the exhalation rate of radon from the soil.

The aim of this study is to measure the radon mass exhalation rates and thoron surface exhalation rate in surface soils collected from Amritsar, Batala and Gurdaspur regions of Punjab by using Smart RnDuo monitor (made by BARC). This area falls within the agricultural, industrial and urban communities which makes this study worthy.

A. Geology of the Area

Gurdaspur district is located in the northern part of the Punjab state. It has a unique characteristic of sharing the international boundary with Pakistan and river Ravi is separating the district from Pakistan, Hoshiarpur, Kapurthala and Amritsar are situated on the eastern , southern and western side of the district respectively. The district is bounded by river Ravi and Beas. Apart from the above small local nalas and called choes are the frequent features in the northern side of the district which ultimately meets the main khads and aluminates ultimately to the rivers Beas and Ravi. Soil of the district is clays and clay with boulders, pebbles, cobbles drain from the Siwalik along with sand of medium to coarse grained gravel.

Amritsar district is located in northern part of Punjab state and lies between 31^0 28' to $32^0$03' north latitude & 74^0 29' to $75^0$24' east longitude.

Total area of the district is 5056 sq.km. Amritsar district falls in between Ravi river and Beas river. Ravi river flows in north west of the district and forms international border with Pakistan. Beas river flows in the eastern part of the district. Soils of the western part of the city are coarse loamy, calcareous soils, where as in the central part of the city, soils are fine loamy, calcareous and are well drained. The soils are Ustochrepts to Haplustaff type. The district forms part of Uppar Bari Doab and is underlain by formations of Quaternary age comprising of alluvium deposits belonging to vast Indus alluvial plains. Sub surface geological formations comprise of fine to coarse grained sand, silt, clay and kankar. Gravel associated with sand beds occurs along left bank of Ravi. The beds of thin clay exists alternating with thick sand beds.

II. Materials And Methodology

A certain amount of different kinds of soil samples obtained from different locations of the region, which were chosen to understand the migration and exhalation of radon in the naturally occurring soils.

The smart RnDuo is active measurement technique has been used for radon and thoron exhalation rate of the collected soil samples. The soil samples were first dried and then placed in accumulating chamber (also called mass exhalation chamber) of height 8 cm and radius 4.5 cm attached scintillation cell. The advanced SMART RnDuo technique manufactured and calibrated by Bhabha Atomic Research Centre, Mumbai, India. Minimum residual volume in a chamber is maintained for accurate exhalation rate. For radon exhalation rate (Jm), measurement cycle should be 1 hour. The linear fitting method is used for the radon concentration (CR) (Bq/m3) at time t is estimated inside the chamber and radon mass exhalation rate Jm is then obtained by a given equation [10,11]

$$\mathrm{C_R(t)} = \frac{Im\,M}{V\,\lambda_e}\,[1\text{-}e^{-\lambda_e t}] + \mathrm{C_0}\,e^{-\lambda_e t} \tag{1}$$

where C_0 is the ^{222}Rn concentration (Bq m^{-3}) present in the chamber volume at t=0. M is the total mass of the dry sample (in kg). V is the effective volume. λ_e is the effective decay of ^{222}Rn and t is the measuring time in hour.

where C_0 is the ^{222}Rn concentration (Bq m^{-3}) present in the chamber volume at t=0. M is the total mass of the dry sample (in kg). V is the effective

volume. λ_e is the effective decay of ^{222}Rn and t is the measuring time in hour.

To study thoron surface exhalation rate, soil samples are placed in a leak proof chamber (same as above) and analyzed by scintillation based thoron monitor [10]. The exhalation chamber was connected through flow mode. The exhalation chamber is closed with a lid which has two 6 mm pipe openings used as inlet and outlet airflow during measurement of thoron concentration. The ^{220}Rn surface exhalation rate (Js) (Bq/m^2/s) in soil samples can be obtained from equilibrium concentration of thoron (C_T) (Bq/m^3) inside the chamber using following equation [12, 13]:

$$J_s = \frac{V \lambda C_t}{A} \tag{2}$$

where V is the residual air volume (m^3) enclosed by the loop, λ is ^{220}Rn decay constant (0.012464 s^{-1}) and A is the surface area (m^2) of sample.

III. Results And Discussion

The measured results of radon and thoron exhalation rate in soil samples belonging to some areas of Gurdaspur, Batala and Amritsar are presented in Table 1. The local soil of this area is commonly used in brick manufacturing for building construction. The values of the radon mass exhalation rate varies from 33.62±0.47 to 33.83±0.98, with an average value of 25.33±0.84 mBq kg^{-1} h^{-1}, 33.62±1.02 to 57.61±1.90, with an average value of 40.78±152 mBq kg^{-1} h^{-1}, and 18.23±0.74 to 49.23±1.32, with an average value of 35.49±1.18 whereas thoron surface exhalation rate varies from 376.14±52.47 to 688.59±73.94, with an average value of 478.38±69.25 mBq m^{-2} s^{-1}, 225.33±51.43 to 476.94± 88.29, with an average value of 339.77±79.24 mBq m^{-2} s^{-1}, and 91.96±56.66 to 897±98.13, with an average value of 375.02±7782 mBq m^{-2} s^{-1} of Gurdaspur, Batala and Amritsar, respectively. The overall value of the radon and thoron exhalation rates by all 15 samples were 18.33 to 57.61, with an average of 33.86±10.89 mBq kg^{-1} h^{-1} and 91.96 to 897.6, with an average of 397.73±188.79 mBq·m^{-2} s^{-1}, respectively. The maximum values of the radon and thoron exhalation rate were 57.61±1.9 mBq kg^{-1} h^{-1} at B3 and 897.6±98.13 mBq m^{-2} s^{-1} at A3, respectively. Radon exhalation rate varies appreciably from one place to another. This variation may be due to the

Table 1. Radon and Thoron exhalation rate in soil samples of three regions of Punjab.

	Location name	**Radon Mass Exhalation ($mBq\ Kg^{-1}\ h^{-1}$)**	**Thoron Surface Exhalation ($mBq\ Kg^{-1}\ s^{-1}$)**
Gurdaspur	G1	19.86±0.47	526.39±87.32
	G2	21.11±0.98	394.62±65.53
	G3	33.83±0.98	688.59±73.94
	G4	27.94±0.92	376.14±52.47
	G5	23.92±0.83	406.19±66.99
Batala	B1	33.62±1.02	225.33±51.43
	B2	37.57±0.93	406.26±96.34
	B3	57.61±1.90	363.64±87.13
	B4	37.71±1.88	266.70±73.18
	B5	37.38±1.85	436.94±88.29
Amritsar	A1	49.23±1.32	296.74±75.5
	A2	47.57±1.78	358.99±90.74
	A3	18.23±0.74	897.60±98.13
	A4	30.31±0.78	91.96±56.66
	A5	32.09±1.28	229.81±68.05

differences in radium content [14] and porosity of the soil [15]. The maximum and the minimum value of the radon and thoron exhalation rate were compared; ratios of maximum to minimum were taken to be 3.16 times and 9.76 times, respectively. The variation of radon mass and thoron surface exhalation rate with locations are given in figure 1.

The results from this study have revealed that radon is not uniformly distributed in soil. This is evident from the fact we have recorded a wide range of radon exhalation rate (18.23 57.61 mBq kg^{-1} h^{-1}) in soil (Table 1). Although, the presence of uranium and radium bearing minerals in host rocks and their interaction with soil is considered to be the main cause for high radon exhalation rate in soil. The high level of radon exhalation rate in soil samples may be attributed to the geology and soil of the region. On the other hand, the north and north eastern parts of the study area are bordered by Punjab and Pakistan where radon exhalation rate in soil is relatively same [16, 17] which to some extents influences the soil of these regions.

The relation between geology and the exhalation rate has also been studied. Figure 2 gives the variation of average mass and surface exhalation rate in soil samples of three regions Gurdaspur, Batala and Amritsar of

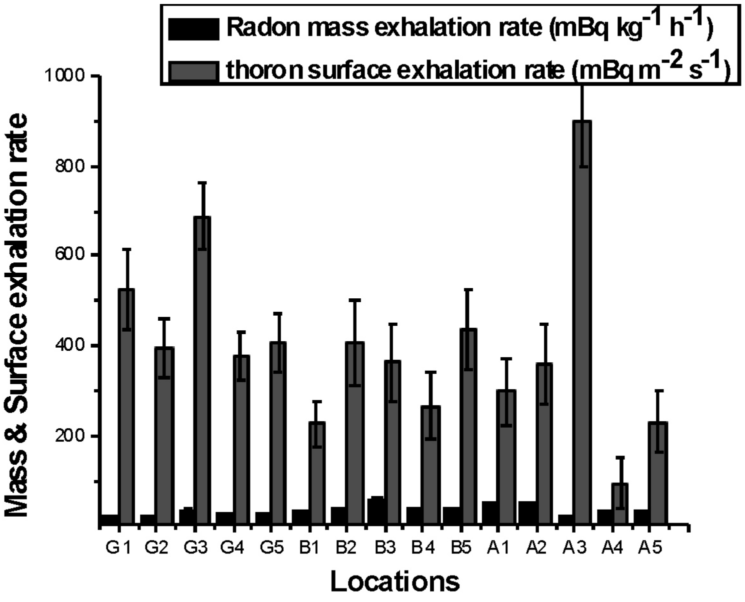

Fig 1. Variation of radon and thoron exhalation rate with locations.

Punjab. The mass exhalation rate has high values in Batala region than Gurdaspur and Amritsar, due to industrial background, agricultural setup and soil of the region, that contain clay with boulders, pebbles, cobbles drain from the Siwalik along with sand of medium to coarse grained gravel. The surface

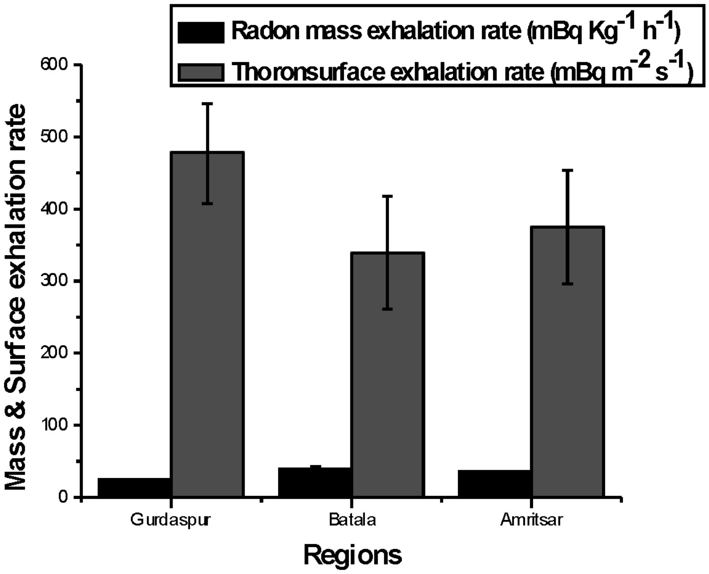

Fig 2. Variation of exhalation rates with different regions.

exhalation rate has high value in Amritsar region. No such correlation has been observed in mass and surface exhalation rate in soil samples.

IV. Conclusions

Radon and thoron exhalation rate was measured in 15 locations of three regions of Punjab. The exhalation rates were obtained and the different among measured values was interpreted by difference of geology. Consequently, the following knowledge was acquired.

(1) The average values of the radon and thoron exhalation rate were 33.86±10.89 mBq kg^{-1} h^{-1} and 397.72±188.79 mBq m^{-2} s^{-1}. The maximum value was compared with the minimum value, the ratio of maximum to minimum radon exhalation and thoron exhalation rate has 3.16 and 9.76.

(2) Exhalation studies are important for understanding the contribution of the soil towards the total concentration found inside the dwellings.

(3) No correlation was found between the radon and the thoron exhalation rates.

(4) Geology of the Batala region appears to be cause for the increased value of average radon mass exhalation rate in soil samples.

V. Acknowledgement

The authors are thankful to the residents of study area for their cooperation during the fieldwork and the Principal of DAV College, Amritsar for their support.

VI. References

[1] S. M. Farid, "Indoor radon in dwellings of Jeddah city, Saudi Arabia and its correlations with the radium and radon exhalation rates from soil" Indoor and Built Environment (2014) DOI: 10.1177/ 1420326 X 14536749.

[2] H. Idriss, I. Salih, S. A. Abdulaziz, M. Y. Abdelgalil, S. A. Salih, A. M. Hasan, M. A. ELtahir and M. O. Mustafa, "A Study of radon in soil gas, trace elements and climatic parameters around South Kordofan state, Sudan" Environ Earth Sci., (2013) DOI 10.1007/s12665-013-2954-2.

[3] R. Mehra, "Use of Gamma Ray Spectroscopy Measurements for Assessment of the Average Effective Dose from the Analysis of 226Ra, 232Th, and 40K in Soil Samples" Indoor and Built environment, 18 (2009) 270275

[4] UNSCEAR, Report to the general assembly with scientific annex, United Nations, New York (2000).

[5] UNSCEAR, Sources and effects of ionizing radiation, Annex A, United Nations, New York, (1988)

[6] R. S. Eaton, "Proceedings of the Workshop on Radon and Radon Daughters in Urban Communities Associated with Uranium Mining and Processing" (Atomic Energy Control Board, Attawa) (1978).

[7] D. M. B. Baruah, P. C. Deka and M. Rehman, "Measurement of radium concentration and radon exhalation rate in soil samples using SSNTDs" The African review of Physics 8 (2013) 215-218.

[8] V. Duggal, R. Mehra, and A. rani, "Study of radium and radon exhalation rate in soil samples from area of Northern Rajestan" J of Geological society of India 86 (2015) 331-336.

[9] C. H. Paredes, W. V. Kessler, R. R. Landalt,P. L. Zimemer and Paustenbach, "Radionuclide Content of 222Rn Emanation from Building Materials made from Phosphate Industry Waste Products" Health Physics, 53 (1987) 22-29.

[10] J. J. Gaware, B. K. Sahoo, B. K. Sapra and Y. S. Mayya, "Indigenous development and networking of online radon monitors in the underground uranium mine" Radiat Protect Environ 34 (2011) 3740.

[11] B. K. Sahoo, B. K. Sapra, J. J. Gaware, S. D Kanse and Y. S. Mayya, "A model to predict radon exhalation from walls to indoor air based on the exhalation from building material samples" Sci Total Environ 409 (2011) 26352641.

[12] B. K. Sahoo, T. K. Agarwal, J. J. Gaware and B. K. Sapra, "Thoron interference in radon exhalation rate measured by solid state nuclear track detector based can technique" J Radioanal Nucl Chem 302 (2014) 14171420

[13] S. D. Kanse, B. K. Sahoo, B. K. Sapra, J. J. Gaware and Y. S. Mayya, "Powder sandwich technique: a novel method for determining the thoron emanation potential of powders bearing high 224Ra content" Radiat Meas 48 (2013) 8287

[14] K. H. Folkerts, G. Keller And R. Muth, “An experimental study of diffusion and exhalation of 222Rn and 220Rn from building materials” Radiat. Prot. Dosim 9 (1984) 27-34.

[15] T. V. Ramachandran, and M. C. Subba Ramu, “Estimation of indoor radiation exposure from the natural radioactivity content of building materials” Oncology 3 (1989) 20-25

[16] S. Rehman, M. Matiullah and B. M. Ghauri, “Effects of moisture on radon exhalation rate from soil, sand & brick samples collected from NWFP and FATA, Pakista”. Radiation Protection and Dosimetry 130 (2008) 172

[17] M. Faheem and M. Matiullh, “Radon exhalation & its dependence on moisture content from samples of soil and building materials” Radiation measurement 43(2008) 1458-1462.

Curr. Rep. Sci. & Tech. 3 (2017) 29-34

Impact of Genre of Alcohol on Biodiesel Production

Meetu Singh[a] *Amit Sarin*[b] *and Neerja*[c]
[a]*Department of Applied Sciences, IK Gujral Punjab Technical University, Jalandhar.*
[b]*Department of Physical Sciences, IK Gujral Punjab Technical University, Jalandhar.*
[c]*PG Department of Physics and Electronics, DAV College, Amritsar.*

Abstract

With the escalated interest in alternative fuels, there has been hype for cleaner and environmentally friendly fuels. Biodiesels are the renewable fuels typically produced by transesterification of vegetable oils and animal fats. The most endorsed approach for transesterification involves reaction of oil with methanol in the presence of a catalyst. Methanol being originated from fossil resources can tarnish the renewable nature of biodiesel. In this study, bio based alcohols viz. ethanol and iso-propanol, are employed for biodiesel production from waste mustard oil and comparison has been made with methanol followed process. The result shows that maximum yield was obtained for methanol and decrease in yield has been observed for ethanol and iso-propanol. Although ethanol and iso-propanol result in declined yield but biodiesel production involving these is completely bio-base, hence renewable.

Keywords : Biodiesels, Renewable, Transesterification, Alcohol, Yield.

I. Introduction

With the progress in technology, mankind has been benefitted in every sphere of living. Energy is the fundamental unit for any living and non living. The consumption of energy from fossil fuels has been the largest constituent of all forms. The energy from fossil sources widened many horizons. However, it has simultaneously faced many environmental concerns, which can threaten the sustainability of our ecosystem. The high demand of diesel in the industrialized world and pollution problems caused by its widespread use make it necessary to develop renewable energy sources of limitless duration and ecofriendly nature. Therefore, another renewable fuel is required to replace diesel fuel and that could be biodiesel [1-2]. Biodiesels are mono-alkyl esters of long chain fatty acids derived from vegetable oils or animal fats through transesterification. There are many feedstocks for the production of biodiesel with edible as well as non edible trait. The usage of non edible oils anticipates the food security. However, blending of straight oils in diesel fuel results into various discrepancies such that poor viscosity and poor density [3, 4]. To keep the properties of biodiesel analogous to diesel fuel, transesterification is typical phenomenon followed up for oils in the presence of certain catalysts. Most of the studies have employed methanol as alcohol in transesterification reaction, which has its origin from fossil resources [5]. Thus biodiesel produced with methanol cannot be considered as completely renewable. Alcohols which are derived from biotic resources ought to be used in order to generate fully renewable biodiesel. In the present study, waste mustard oil has been used to synthesize biodiesel which is reported in many texts as non edible oil due to excessive amount of erucic acid [6]. It has also been seen that the low quality mustard oil, which is not suitable for cooking purposes can be used in the synthesis of biodiesel [7]. Authors investigated the potential of ethanol and iso-propanol for biodiesel production from waste mustard oil and comparison has been made with process followed with methanol.

II. Materials And Methods

The waste mustard oil (WMO) was collected from a local cafeteria and all chemicals were purchased from Sigma Aldrich, were of analytical grade.

A. Free Fatty Acid (FFA) Content of oil

FFA of oil was determined via evaluation of acid number. Acid number of waste mustard oil was found to be 1.8 with titration against KOH and phenolphthalein as an indicator. The method followed for the synthesis of biodiesel is base transesterification, as FFA was observed to be less than unity.

B. Transesterification

Transesterification reaction is a chain reaction in which tri-glyceride (oil) reacts with alcohol in the presence of catalyst (KOH) followed by separation process. Methanol, ethanol and isopropanol were separately added to the potassium hydroxide pellets as catalyst (1.5 wt % of oil) and stirred until the complete dissolution of catalyst in employed alcohols. The above stirred solutions were added to WMO in reactor and the reaction temperature was set at 65°C. The stirring of mixture was carried out for 1 hour at 400 rpm. After completion of the reaction, the material was transferred to separating funnel and kept overnight to settle down, which results in the formation of two phases. Upper phase was waste mustard methyl ester (biodiesel) and lower part was glycerol. Waste mustard biodiesel (WMB) was then washed with the warm water four to five times to remove the traces of glycerin, unreacted catalyst and soap formed during the transesterification [8, 9]. This process has been undertaken for each alcohol genre.

C. Biodiesel Yield

The biodiesel yield has been calculated by using the expression given below:

$$Biodiesel\ yield\ (in\ \%) = \frac{Weight\ of\ Biodiesel}{Weight\ of\ Oil\ used}\ X\ 100$$

The process yield for biodiesel form waste mustard oil was calculated with varying alcohol genre and reaction time was kept same for all the contents i.e. 1 hour. The ratio of catalyst (KOH) was also kept same (1.5 wt. % of oil).

III. Results And Discussions

The experimentation with different alcohol genre viz. methanol, ethanol and isopropanol to analyze the biodiesel yield revealed that maximum yield has been obtained for methanol (78.98%). However, for ethanol yield is 70.87% and 63.41% for isopropanol as shown in figure 1.

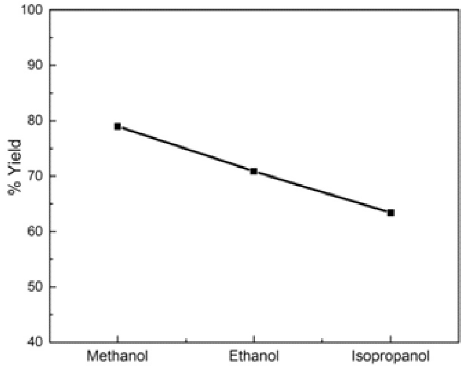

Figure 1: Biodiesel yield for different alcohols.

The biodiesel yield dropped down with increase in chain length of alcohol which has been attributed to lesser reactivity of higher alcohols due to increasing steric hindrance. The chemical structure of three alcohols used for study is given in figure 2.

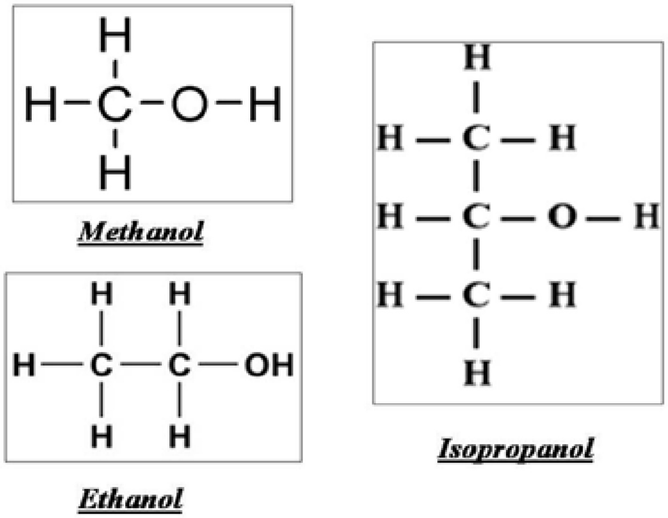

Methanol

Ethanol

Isopropanol

Figure 2: Chemical structure of employed alcohols.

The decrease in yield has been minimized by adding more amount of catalyst (1.75 % wt. of oil) and increasing temperature to 75ºC for reaction as shown in figure 3.

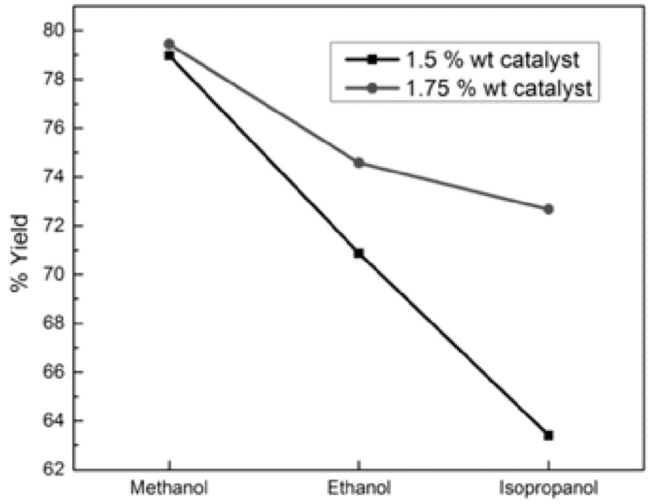

Figure 3: Comparison of alcohol activity for different ratios of catalyst.

There is minimal change in yield for methanol added reaction when amount of catalyst and temperature has been increased. However, change in catalyst and temperature supported the bio based alcohols for better yield of biodiesel.

VI. Conclusion

The use of biotic alcohols has been advantageous in terms of renewable nature of biodiesel. Whether the experimentation shows decrease in yield of biodiesel. This declination can be controlled by increasing temperature of reaction and adding more catalyst during transesterification. The study recommended the usage of bio based alcohols to untarnish the renewable nature of biodiesels.

V. References

[1] Sarin A. Biodiesel Production and Properties: RSC Publications, ISBN: 978-1-84973-470-7, 2012.

[2] Najafi G., Ghobadian, B., Yusaf, T. F. Algae as a sustainable energy source for biofuel production in Iran: A case study. Renewable Sustainable Energy Rev. 2011, 15, 3870-76.

[3] Karmee S.K., Chadha A. Preparation of Biodiesel from crude oil of Pongamia Pinnata. Bioresour. Technol, 96, 1425-1429, 2005.

[4] Agarwal A K. Biofuels (alcohols and biodiesel) applications as fuels for internal combustion engines.Prog Energy Combust Sci 2007, 33, 23371.

[5] Verma P, Sharma MP, Dwivedi G. Impact of alcohol on biodiesel production and properties. Renew Sust Energy Rev 2016, 56, 31933.

[6] Sanjid A., Masjuki H.H., Kalam M.A., Abedin M.J., Rahman S. M. A. Experimental Investigation of Mustard Biodiesel Blend Properties, Performance, Exhaust Emission and Noise in an Unmodified Diesel Engine, ICESD 2014; February 19-21, Singapore.

[7] Lee S.T., Radu S., Ariffin A., Ghazali H.M. Physico-Chemical Characterization of Oils Extracted from Noni, Spinach, Lady's Finger, Bitter Gourd and Mustard Seeds, and Copra, Int. J. of Food Properties, 2015, 18, 2508-2527.

[8] Paras H.S., Hans N.S., Sarin A., Oxidation stability of Mustard

Methyl Ester: Biodiesel made from waste mustard oil, IJARSE, 4, ISSN: 2319-8354.

[9] Qin S., Sun Y., Meng X., & Zhang S. Production and analysis of biodiesel from non-edible seed oil of Pistacia Chinensis. Energy Exploration and Exploitation 2010, 28, 37-46.

Curr. Rep. Sci. & Tech. 3 (2017) 35-40 © Khalsa College Amritsar

Dispersion Coefficients For The Interaction Of Sodium Atom With Dielectric Surfaces

Jasmeet Kaur ,Kiranpreet Kaur and Bindiya Arora
Department of Physics, Guru Nanak Dev University, Amritsar 143005, Punjab, India
Email- jasmeetphy.rsh@gndu.ac.in

Abstract

The C_3 coefficients for the interaction of a sodium atom with various dielectric surfaces such as SiNx, sapphire (ordinary and extra-ordinary) and YAG are determined using accurate dynamic polarizability values of the sodium atom evaluated by taking into account the relativistic coupled cluster method. The retardation coefficients are also studied graphically as functions of separation distance for the interaction of Na atom with the above considered material media. The present work is largely motivated by a number of applications. For the sake of simplification, we formulate a directly accessible functional form to generate the f_3 coefficients at a given distance of separation.

Keywords: Atom-surface interactions; van der Waals forces; retardation; dynamic polarizability

I. Introduction

The long range forces between an atom and surface have a significant interest in studying various domains of physical sciences and contemplating these forces can result in new pathways towards engineering, technology and research areas. Considering unique interactions of atoms or molecules with atomically well defined surface is beneficial for advocating future device applications using nanometer dimensions. Atom-surface interactions are important to study numerous physical, chemical, or biological processes. Research works of Lennard-Jones [1], Bardeen [2], Casimir and Polder [3] and Lifshitz [4] has found increasing interest over last decades. Earlier studies have shown that atoms and molecules which get adsorbed on a solid surface can interact indirectly through electron scattering or elastic distortion of the substrate. In the non-retarded regime, the forces between the fluctuating atomic dipole and its immediate image associated with the polarization charges induced in the surface brings about the atom-surface van der Waals interactions. Thus for the short separation distance 'a' between the atom and surface, the interaction energy scales as $1/a^3$, while for large atom-surface distances as compared to a typical atomic wavelength, the interaction energy scales as $1/a^4$ [3]. Such long range interactions between two atoms or between an atom and a surface of the trapping material are essential for understanding fundamental physics of atomic collisions and exploring ultracold atomic experiments [2]. These atom-surface interactions can cause a shift in the oscillation frequency of the trap which can vary the trapping frequency and hence there is a likewise change in the magic wavelengths for the state-insensitive trapping of the trapped condensate. A comprehensive cognizance of dispersion coefficients is necessary for the experimental studies of photoassociation, evaluation of Bose-Einstein condensates (BECs), fluorescence spectroscopy and determination of scattering lengths.

The dispersion coefficients of interaction between an atom and a wall using various many-body methods have been reported by several groups. The atom-wall interaction potentials have a significant dependence on the dielectric properties of the materials and calculation of these dispersion coefficients is very tedious. The C_3 coefficients can be efficiently expressed in terms of the conducting properties of trapping medium and the dynamic dipole polarizability of the interacting atom using Lifshitz theory [4]. Some of the earlier studies have calculated these material dependent dispersion coefficients by using less accurate dipole polarizabilities.

In the present work, we determine the dispersion coefficients for the sodium atom considering the trapping material as dielectric objects like SiNx, sapphire (ordinary, extraordinary and birefringent) and YAG by using accurate polarizability value of sodium atom. The high precision calculations of the dispersion coefficients can be evaluated by determining principle electric dipole (E1) matrix elements using relativistic coupled-cluster (RCC) approach at the linear approximation (SD method) and evaluating the core and core-valence correlation contributions to the dipole polarizabilities by making use of relativistic random phase approximation (RRPA method) and Dirac-Fock (DF method) respectively [5]. Unless stated otherwise, we use atomic units (a.u.) throughout the paper.

Theory The general expression of interaction potential for the interaction of a polarizable particle interacting with a surface or wall made up of a continuous medium having a frequency dependent permittivity is given in refs. [4,6]. Taking into consideration the retardation effects, a more general expression of interaction potential is conveniently expressed as-

$$V(R) = -\frac{C_3}{R^3} f_3(R) \text{ a)}$$

$$C_3 = -\frac{1}{4\pi}\int_0^\infty d\omega \alpha(i\omega) S(i\omega) \text{ b)}$$

$$S(i\omega) = -\frac{\in (i\omega) - 1}{\in (i\omega) + 1} \text{ c)}$$

and retardation coefficient $f_3(R)$ is expressed as

$$f_3(R) = \frac{1}{4\pi C_3}\int_0^\infty d\omega \alpha(i\omega) e^{-2\alpha_{fs}\omega R} P^{(\infty)}(\alpha_{fs}\omega R) \text{ d)}$$

with $P^{(\infty)}(x) = 1 + 2x + 2x^2$

where the dispersion C_3 coefficient is given by

The C_3 and f_3 coefficients are evaluated by adopting similar approach as was done [6]. The more accurate values of dynamc polarizabilities of ground state of Na atom are determined by applying the CCSD approach as was taken by us in refs. [5,6]. The total polarizability can be divided into three parts, valence, core and core-valence contributions. It is found that the major contribution to the alkali atoms are due to the correlations due to the valence contribution. The complex frequency dependent dielectric permittivities of the above dielectric surfaces are taken from the handbook of Palik [7] except for the case of SiNx for which Tauc-Lorentz model [8] is

$$\overline{\in}\,(i\omega) = \left[\in_{\parallel}(i\omega)\in_{\perp}(i\omega)\right]^{\frac{1}{2}} \text{ e)}$$

used for estimating dielectric constants.

For a uniform birefringent dielectric surface, with the symmetry axis perpendicular to the interface, the interaction potential represented by Eq. (1) is still valid even if □ is replaced by defined as where and are the dielectric permittivities for the electric fields parallel and perpendicular to the interface between the atom and the dielectric medium respectively.

II. Results

The determination of C_3 coefficients requires the accurate evaluation of dynamic polarizabilities of Na atom. Table 1 presents the scalar polarizabilities of the sodium atom in its ground state along with the E_1 matrix elements for various transitions. As can be clearly seen from the table that our calculated polarizability value is in good agreement with the experimentally measured value. Table 2 represents the computed atom-surface dispersion C_3 coefficients for the interaction of Na atom with various dielectric surfaces. It can be seen from the table that the valence correlation contribution is dominant among the core, core-valence and tail correlations. Of all the interacting surfaces, the C_3 coefficients for the extraordinary sapphire is the highest, although there is not much variation

Table 1.The E1 matrix elements and various contributions to the scalar polarizabilities of the ground state in Na atom

Transitions	E1 matrix elements(a.u.)	Polarizability(a.u.)
$3s_{1/2}$-$3p_{1/2}$	-3.531	53.7906
$3s_{1/2}$-$4p_{1/2}$	-0.305	0.2251
$3s_{1/2}$-$5p_{1/2}$	0.107	0.0240
$3s_{1/2}$-$6p_{1/2}$	0.056	0.0062
$3s_{1/2}$-$3p_{3/2}$	-4.993	107.4572
$3s_{1/2}$-$4p_{3/2}$	0.435	0.4581
$3s_{1/2}$-$5p_{3/2}$	-0.154	0.0494
$3s_{1/2}$-$6p_{3/2}$	0.081	0.0130
α_{vc}		-2.159E-002
α_{c}		0.834
α_{tail}		0.089
α_{total}		162.93
α_{total}	[9]	162.9(6)

Table 2. Calculated C3 coefficients for the interaction of the Na atom with the dielectric surfaces SiNx, Ordinary Sapphire,. Extraordinary Sapphire, Birefringent sapphire and YAG along with their contributions from various parts of dynamic polarizabilties

Surface	Core	Valence	Core-Valence	Tail	Total
SiN_x	0.024	0.788	~0	0.001	0.7939, 0.67[8]
Ordinary Sapphire	0.0441	0.7854	-0.00085	0.0015	0.8302
Extraordinary Sapphire	0.0469	0.7852	-0.0009	0.00155	0.8328
Birefringent Sapphire	0.0455	0.7853	-0.00087	0.00152	0.8316
YAG	0.040	0.7638	-0.00078	0.00142	0.8045

We also evaluate the retardation coefficients f_3 for all the dielectric surfaces interacting with Na atom. The Fig 1 shows the comparison of the f_3 coefficients as a function of separation distance for the interaction of Na atom with various dielectric surfaces (SiNx, sapphires and YAG).

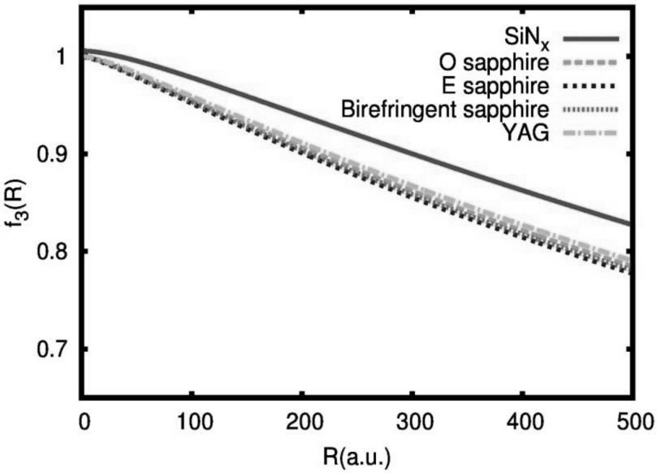

Fig1.The retardation coefficient f3(R) for Na atom as a function of the distance R from the different dielectric surfaces such as SiNx, Sapphire (ordinary, extraordinary, birefringent) and YAG.

***Table 3**. The Fitting parameters a and b for f_3 coefficients with various dielectric surfaces.*

Fitting parameters	SiN_x	Ordinary sapphire	Extraordinary sapphire	Birefringent sapphire	YAG
a	0.9376	0.9876	0.9913	0.9895	0.9798
b	0.0766	0.0789	0.0807	0.0798	0.0791

It can be clearly observed from the figure that as the separation distance (short separations). Furthermore, for future theoretical andexperimental verifications of our results, we devise a logistic functional form in order to compute f_3 coefficients at given separation distance as

$$f_3(R) = \frac{1}{a + b(\alpha_{fs} R)} \tag{6}$$

where a and b are fitting parameters which are tabulated in Table 3 for all the cases of interacting Na atom with dielectric media.

III. Acknowledgments

The work of B.A. is supported by CSIR Grant No. 03(1268)/13/EMR-II, India. K.K. acknowledges the financial support from DST (Letter No. DST/INSPIRE Fellowship/2013/758). J.K. gratefully acknowledges UGC-BSR (Grant No. F.7-273/2009/BSR) for funding.

IV. References

[1] J. E. Lennard-Jones, ”Processes of adsorption and diffusion on solid surfaces,”Trans. Faraday Soc., 28(1932) , 33-359.

[2] J. Bardeen, ”The Image and Van der Waals Forces at a Metallic Surface,”Phys. Rev. 58(1940),727.

[3] H. B. G. Casimir and D. Polder, “The Influence of Retardation on the London-van der Waals Forces”, Phys. Rev. 73(1948), 360.

[4] E. M. Lifshitz, “The theory of molecular attractive forces between solids”, Zh. Eksp. Teor. Fiz. 29(1955), 94.

[5] J. Kaur, D. K. Nandy, B. Arora, and B. K. Sahoo, “Properties of alkali-atoms and alkaline-earth-metal ions for an accurate estimate of their long-range interactions “, Phys. Rev. A91(2015), 012705.

[6] B. Arora and B. K. Sahoo, “van derWaals coefficients for alkali-metal atoms in material media”, Phys. Rev. A 89(2014), 022511.

[7] E. D. Palik, “Handbook of optical constants of solids”, Academic Press, San Diego (1985).

[8] J. D. Perreault, A. D. Cronin and T. A. Savas, "Analysis Of A Material Phase Shifting Element In An Atom Interferometer,Phys. Rev. A71(2005), 053612.

[9] A. J. Thakkar and C. Lupinetti, “The polarizability of sodium: theory and experiment reconciled,” Chem. Phys. Lett402 (2005) , 270-273.

Preparation and Characterization of Reduced Graphene Oxide

Manpreet Kaur[a], Sonika Thakur[a], Simranjeet Kaur[a],
Satvir Singha and Aman Mahajan[b]
[a]Department of Physics, Guru Nanak Dev University College Verka,
Amritsar, Punjab, India
[b]Department of Physics, Guru Nanak Dev University, Amritsar, Punjab, India
thakur.sonika7@gmail.com

Abstract:

The present work is aimed at the synthesis of graphene oxide (GO) and reduced graphene oxide (RGO). GO has been prepared from natural flake graphite by Hummer's method. The RGO has been obtained by chemical reduction of GO using reducing agent hydrazine hydrate (N_2H_4). The synthesized GO and RGO has been characterized by X-ray diffraction and Raman spectroscopy. The XRD results indicate that there is an obvious change in crystal structure due to reduction. These results are well supported by the Raman spectroscopy in which the ID/IG ratio of GO increases notably. It indicates that the structure of GO is altered with high quantity of structural defects. In case of RGO, the G band is shifted to a lower wave number due to decreased size of sp^2carbon atoms.

Keywords: Graphite Powder; Reducing agents; XRD; Raman spectroscopy.
PACS: 81.05.uf; 61.05.C-; 42.65.Dr.

I. Introduction

Graphene is the name given to a flat monolayer of carbon atom tightly packed into a two dimensional sheet of sp^2 hybridized carbon atom.[1-4] Presence of high quality sp^2 conjugated bond in the carbon lattice, electrons were found to move in a graphene layer without scattering with ultra high mobilities at extreme temperature[6-7,12]. Its synthesis has been investigated in many fields with potential applications in biomedicines, reinforced composites, sensors, energy convertor, storage devices and in optoelectronic devices. Recent investigations on graphene have displayed that it can be a suitable material for the development of new technologies in the areas of critical importance [3-9].

Chemical method has become a promising method to produce graphene sheets, although graphene produced by this method could contain a significant functional groups and defects. This process involves three important steps which are graphite oxidation, exfoliation of graphite and reduction of graphene oxide sheets. Graphene oxide has a wide range of oxygen functionalities such as 1, 2-epoxides and alcohol groups on the basal planes. It is well known that the amount of the functional groups are removed by chemical reduction using reductants producing electrically conducting graphene based platelets on a large scale [8-11]. The objective of this work is to synthesize the graphene by low cost method and to investigate its structural changes.

II. Experimental

Materials

Graphite powder, sodium nitrate (N_aNO_3), potassium permanganate (KM_nO_4), 98% sulphuric acid (H_2SO_4), 30% hydrogen peroxide (H_2O_2) aqueous solution.

a) Preparation of graphene oxide (GO)

GO is prepared from natural graphite by the well-known Hummers and Offema method. Typically, 2 g of the natural graphite powder was added into a 250ml beaker and 1g of sodium nitrate and 46 ml of sulphuric acid were added subsequently under stirring in an ice-bath. Then 6 g of potassium permanganate was added slowly into the beaker under stirring condition and the temperature of the system was controlled up to 20°C. After 5 minutes the ice-bath was removed and the system was heated at 35°C for 30 minute. Then 92 ml water was slowly added into the system, the stirring was continued for 15 minutes. Then 80ml of hot water with 60°C and 3% aqueous hydrogen peroxide solution was added sequentially to the mixture solution to terminate the reaction. Finally, the mixture was centrifuged at 7200 rpm for 30 min, and the residue was washed by warm water until the pH value of the upper layer of the suspension arrived at near 7. The resulting product was then dispersed in distilled water, exfoliated by ultrasonic for 30 minutes to remove the unexfoliated graphene ,finally, the stable suspension of black GO was obtained.

b) Reduction of exfoliated GO with hydrazine hydrate (N_2H_4)

Typically, GO was put in a 250ml round bottom flask and water 100 ml was then added, to form inhomogeneous yellow brown dispersion. The dispersion was sonicated using ultrasonic bath cleaner, until it become clear. Hydrazine hydrate of 1ml of 100 mmol concentrations was added to graphene oxide to reduce. The obtained solution was then heated in oil bath at 100°C under a water cooled condenser for 24 hours over which the reduced GO precipitated out as a black solid.

III. Characterization

Crystal features of graphene oxide and reduced graphene oxide were recorded at the room temperature using Cu K_α radiation (λ=1.5418) in XRD -7000 Shimadzu X-Ray Diffractometer at a scanning rate 20 per minute. The layer spacing (d- spacing) calculated with the Bragg's equation and the change of diffraction peak could also be observed. Raman spectra of the samples under investigation were recorded using Reinshaw In-Via Reflex Micro Raman spectrometer using 514.5 nm Argon ion laser over the spectral range 1000-2500 cm-1 at room temperature.

IV. Results And Discussion

X-Ray Diffraction

Fig1.shows the XRD patterns of graphite, graphene oxide (GO) and reduced graphene (RGO) respectively. The diffraction peaks at $2\theta=26.28^0$and 43.97^0 is assigned to the graphite flakes. The XRD pattern of GO powder shows a diffraction peak at $2\theta=11.35^0$. After the reduction of GO, the sharp peak at $2\theta=11.35^0$ of RGO disappeared, but a new peak at $2\theta=25.95^0$ appears which is closer to the diffraction peak of graphite. The interplanar spacing of graphite and GO are found to be 0.338 nm and 0.771 nm for the prominent peaks. An increased interlayer distance between consecutive carbon basal planes shows that there is an intercalation of oxygen functional group and water molecules into carbon layer structure during oxidation. It is further observed that reduction of GO (RGO) causes decrease in inter planar spacing from 0.771 nm to 0.343 nm due to the elimination of oxygen containing groups from the graphene sheets.[9,13] This result supports that during reduction of graphene oxide, parts of the basal planes near the edges becomes reduced and subsequently stack together due to π-π interaction, thus narrowing the interlayer distance.

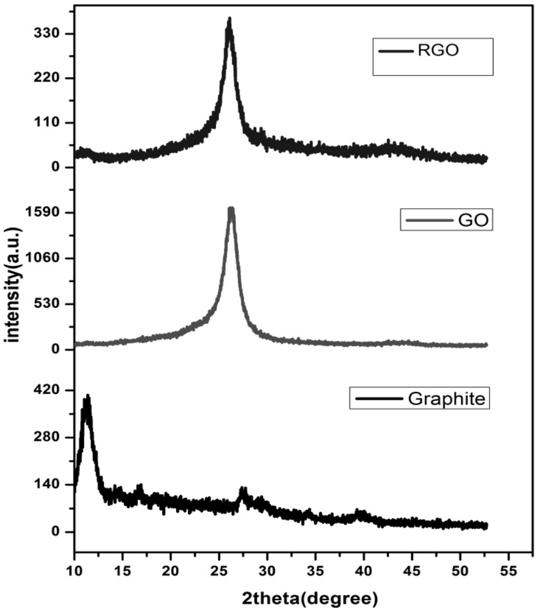

Fig.1. XRD of graphite,graphene oxide(GO),reduced graphene oxide(RGO)

Raman spectra

Fig. 2(a) shows the Raman spectra of graphite flakes and Fig. 2(b) shows Raman spectra of GO and RGO, respectively. In Fig. 2(a), the bands at 1593 cm^{-1} and 1361cm^{-1} are assigned as graphite like G and disorder D bands. The G-band is seen at 1598 cm^{-1}, 1588 cm^{-1} and D-band is at 1356 cm^{-1} and 1354 cm^{-1} for GO and RGO, respectively. The G-band is common for all sp^2 carbon forms, and it arises due to C-C bond stretch. The G- band in GO is shifted to a higher wave number due to oxygenation of graphite, which reveals the formation of sp carbon atoms. The disorder of crystal structure is determined by the intensity ratio between intensity of D-band and G-band (ID/IG). The increase of ID/IG from 0.78 (graphite) to 0.88 (GO) confirms the grafting of oxygen containing functional group to the graphitic layers. During reduction, the D-band intensity is reduced, but not so much as in graphite. This suggests that the newly formed sp^2 carbon atoms in RGO are smaller in size compared to the sp^2 carbon atoms in graphite. Therefore the crystalline size of sp^2 domain is decreased in RGO as compared to GO, but there are an increased number of sp^2 domains on reduction.[8,14]

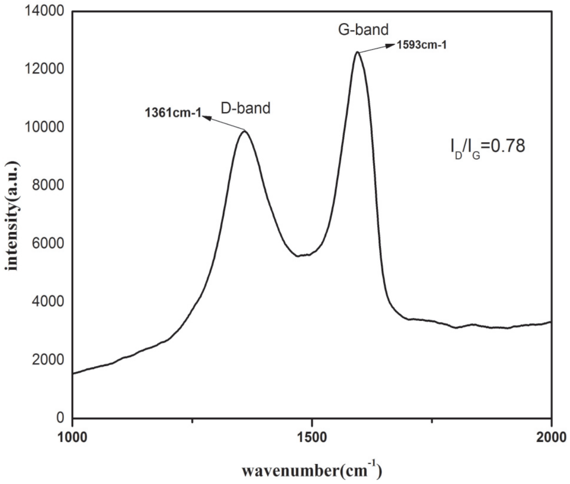

Fig. 2(a) *Raman spectra of graphite*

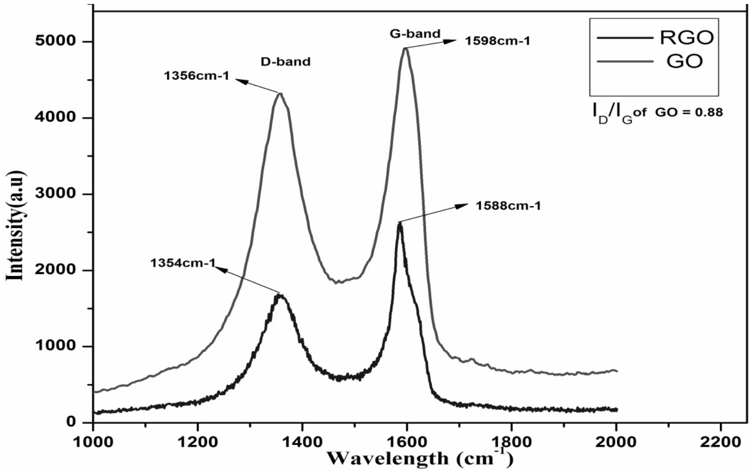

Fig 2.(b) *Raman sperctra of graphene oxide(GO), reduced graphene oxide(RGO)*

V. Conclusion

Graphene oxide has been prepared by Hummer's method and reduced graphene oxide has been synthesized using hydrazine hydrate successfully.The XRD results indicate that the layer spacing of graphene oxide (GO) is longer than that of the graphite which gives the proof of grafting of oxygen functional groups. The C=O groups of GO enable immobilization of various biomolecules through the covalant bond. In addition, Raman charcterization indicates that the hydrazine treatment results in the formation of unsaturated and cojugated carbon atoms, which in turn imparts electrical conductivity. As a result, reduced graphene oxide (RGO) sheets may find use in a variety of applications such as hydrogen storage and in biosensors.

VI. Acknowldgment

The authors wish to thank the Department of Physics and Chemistry, Guru Nanak Dev University, Amritsar, for providing the XRD and Raman facility.

VII. References

1. M. J. Allen, V. C. Tung, and R. B. Kaner, "Honeycomb Carbon: A review of Graphene ," Chem. Rev.110 (2010)132-145.
2. A. Dato, V. Radmilovic, Z. Lee, J. Phillips,and M. Frenklach, "Substrate-Free Gas-Phase Synthesis of Graphene Sheets",Nano Lett.8(7),(2008) 2012-2016
3. T. Rattanaa,, S.Chaiyakuna,e, N.Witit-anuna,e, N. Nuntawongb, P. Chindaudomb,S. Oaewc ,C. Kedkeawd, P. Limsuwand, " Preparation and characterization of graphne oxiode nanosheets". Procedia Engineering 32 (2012) 759 764.
4. N. Cao and Y. Zhang, "Study of Reduced Graphene Oxide Preparation by Hummers' Method and Related Characterization"J.Nanomaterial (2015) Article ID 168125
5. V. Loryuenyong Totepvimarn, P. Eimburanapravat, W. Boonchompoo, A. Buasri1, " Preparation and Characterization of Reduced Graphene OxideSheets via Water-Based Exfoliation and Reduction Methods"Advances in material science and engineering(2013),Article ID 923403,5 pages
6. S. Swain, "Synthesis and Characterization of Graphene BasedUnsaturated Polyester Resin Composites" Transaction on electrical and electronic materials(14) 2013,53-58
7. A. Becerril, Jie Mao, Zunfeng Liu, Randall M. Stoltenberg, Z. Bao, and Y. Chen, "Evaluation of Solution-ProcessedReduced Graphene

Oxide Films asTransparent Conductors"ACS nano2(3)2008 463-470

8. W. Chen, L. Yan, and P. R. Bangal" Chemical Reduction of Graphene Oxide to Graphene by Sulfur-Containing Compounds" J. Phys. Chem. C114(47)(2010)19885-19890
9. S. Park , J. An , Je. R. Potts , A. Velamakanni a, S.Murali ,Rodney S. Ruoff , "Hydrazine-reduction of graphite- and graphene oxide" Carbon. 4 9 (2011) 3019 3023
10. W. Chen and L.Yan "Preparation of graphene by a low-temperature thermal reduction at atmosphere pressure" Nanoscale 2 (2010) 559563
11. W. Chen, L. Yan, Prakriti R. Bangal"Preparation of graphene by the rapid and mild thermal reduction of grapheneoxide induced by microwaves" Carbon48(4) (2010) 1146-1152
12. S. Park,Rodney S. Ruoff1 " Chemical methods for the production of graphenes"N.nanotecnology4 (2009) 217-224
13. S. K. Mishraa, S. N. Tripathib, V. Choudhary, B. D. Gupta "SPR based fibre optic ammonia gas sensor utilizing nanocompositefilm of PMMA/reduced graphene oxide prepared by in situpolymerization" Sensors and Actuators B 199 (2014) 190200
14. S. Perumbilavil, P. Sankar, T. Priya Rose, R. Philip" White light Z-scan measurements of ultrafast optical nonlinearity in reduced grapheneoxide nanosheets in the 400700 nm region" Appl. Physc. Lett.107(2015),051104
15. K. N. Kudin, B. Ozbas, H. C. Schniepp,R. K. Prud homme, I. A. Aksay,and R. Car, "Raman Spectra of Graphite Oxide and Functionalized Graphene Sheets"nanoletters 8 (2008), 36-41

Curr. Rep. Sci. & Tech. 3 (2017) 48-52

Raman Effect of Low Density Polyethylene/Carbon Nanotube Nanocomposites

Kusum Devgan
Department of Physics S.R. Government College for Women, Amritsar, Punjab, India,
kusamdevgan93@yahoo.com

Abstract:

Nano-composites of LDPE and MWCNT are developed in the present study by using solvent mixing method. Xylene has been applied as a solvent which can dissolve low density polyethylene (LDPE) at about 1150C. The solution of LDPE in xylene has been prepared with various percentages of MWCNT (0, 1, 2, 5, 10 wt% of MWCNT) composite to form thin film after drying. Electric arc discharge method has been used to synthesize MWCNT. Raman spectroscopy was used to study the characteristics of these composites and hence variation in intensity of CNT's peak with variation in concentration of CNT was revealed.

Keywords: Polymers, nanocomposites, Raman spectroscopy, nanotubes, Solvent effects

PACS: 81.05Qk; 78.67.Sc; 82.80.Gk; 78.67.Ch; 82.20.Yn

I. Introduction

Carbon nanotubes have a hollow cylindrical structure and are members of fullerene family. Gold rush was created amongst the researches to explore new potentials of CNT due to its extraordinary intrinsic properties like high melting point, high mechanical strength [1] and electrical conductivity [2] and thermal conductivity [3]. Dispersion of CNTs in polymers is difficult due to the forces contributing to the formation of aggregates. These properties make MWCNT capable for production of nano-composites. A number of methods have been used for the production of thermosetting polymer/MWCNT composites which consist of: in situ polymerisation [4-5] solvent mixing [6-8] and melt blending method [9-10]. Recent studies have shown a considerable development in mechanical strength of polymer on CNT addition[11]. Some studies have not only shown a significant improvement of the mechanical and electrical properties but have also provided many benefits such as flexible features, easy processing, and lightweight [12]. In this study, LDPE/MWNTs nano-composites have been fabricated by using solvent mixing method. This study could be further expended to study the mechanical, electrical, thermal properties of the nano-composites prepared in this study.

II. Experimental

For this study low density polyethylene film grade obtained from Indian oil limited and Xylene rectified with 97% purity obtained from fisher scientific were used. CNT used in this study has been developed by liquid arc discharge method having an average diameter of 12 nm and MWCNT have been prepared by using liquid arc discharge method. The sodium chloride solution was used as a medium in preparation of MWCNT. The electrodes made of two graphite rods having purity of 86.5% were used and an arc is formed between them at a current of 50 A and 150 V. MWCNT as well some amorphous carbon were produced with this arc, amorphous carbon was further removed by refluxing the sample with an oxidizing agent like nitric acid. MWCNT produced in this process were around 12 nm in diameter and 11.5m in length [13]. In this study polymer nano-composites have been prepared using solvent mixing method [14]. LDPE was dissolved in xylene by melting low density polyethylene (LDPE) at a temperature of 115◦C in presence of xylene. Simultaneously a measured amount of MWCNT was obtained in a small quantity of xylene solution. The two solutions prepared were combined together and thin layers of sheets of polymer nano-composites were formed on glass sheet. The Raman spectroscopy has been performed on Renishaw micro Raman spectrometer at 785 nm to investigate morphology and distribution of MWCNT in the Nano-Composites.

III. Results And Discussion

In general carbon nanotubes have two peaks. One formed at 1476 cm^{-1} is known as the G Band (Graphitic Band) and other formed at 1295 cm^{-1} is known as the D Band (Defects Band) [15]. The Raman spectra of nano-composites prepared with various percentages of MWCNT (0, 1, 2, 5, 10 wt% of MWCNT) composite is shown in Fig. 1.

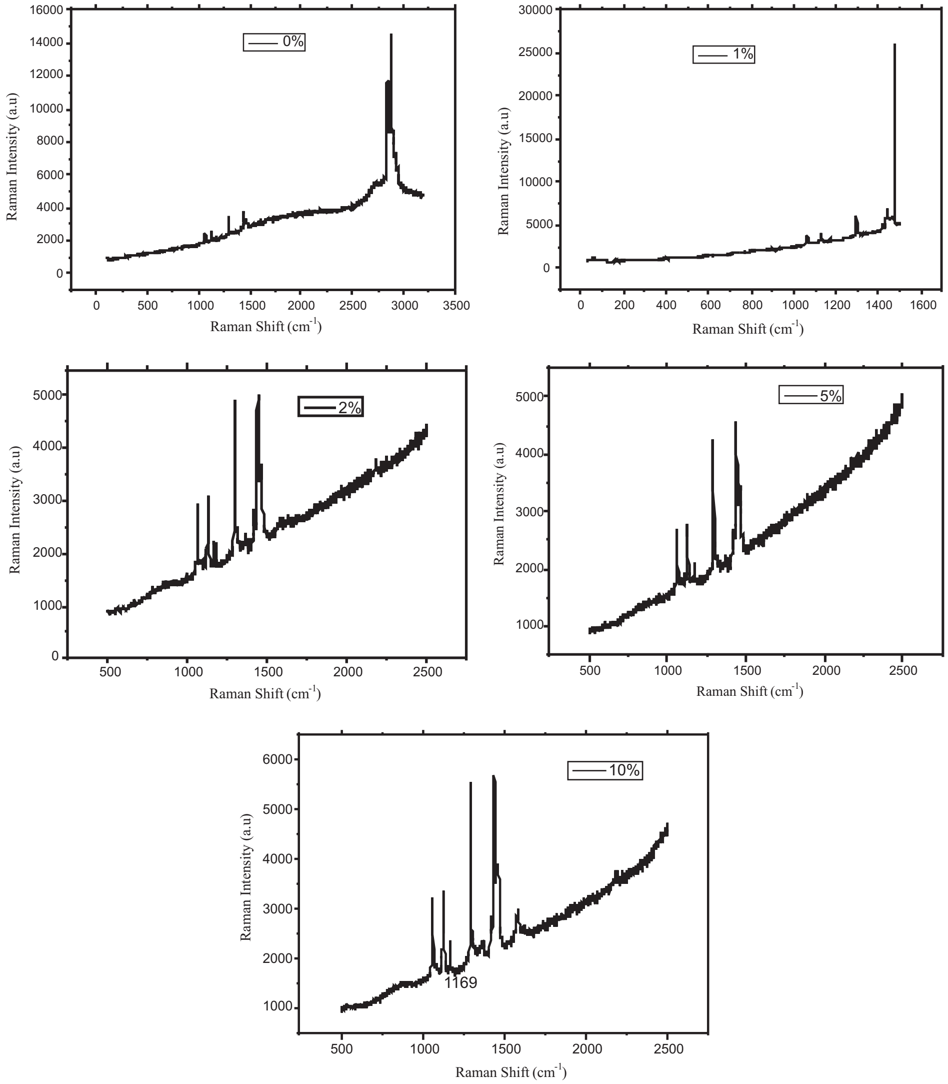

Fig.1. Raman Spectra variation in intensity of CNT's peak with variation in concentration of CNT.

The interaction between nanotubes and polymer is speculated by a peak shift or a peak width change [16]. Fig. 1 divulges the increase in intensity of CNT peaks with the increasing CNT content in the nano-composite. Raman spectra of pure CNT divulged that peaks at 1385.9 cm^{-1} (D Band) and1574 cm^{-1} (G Band) of CNT were formed. Thus in CNT's fabricated in LDPE the D Band and G Band were found to decrease by 90.9 cm−1and 98 cm^{-1} respectively, which may be due to the interaction between LDPE polymer and CNT's.

IV. Conclusions

Since polymers are extensively used for several engineering applications where low weight is a primary necessity, it becomes essential that they possess high mechanical strength. It is predictable that MWCNT will be able to contribute ample strength to LDPE polymers used for various other applications. The results showed that intensity of CNT's peak was found to increase with the increase in concentration of CNT which suggested the interaction occurring between polymer and CNT.

V. Acknowledgments

Guru Nanak Dev University, Amritsar is highly acknowledged for providing Raman Spectroscopy to the author for the experimental work.

VI. References

[1] P. Jindal, and V.K. Jindal, "Strains in axial and lateral directions in carbon nanotubes" J. Comput. Theor. Nanosci. 3 (1) (2006) 148152.

[2] T.W. Ebbesen, "Carbon nanotubes" Annu. Rev. Mater. Sci. 24 (1994) 235.

[3] G.L. Hwang, Y.T Shieh and K.C. Hwang, "Efficient load transfer to polymer grafted multiwalled carbon nanotubes in polymer composites" Adv. Funct. Mater. 14 (2004) 487-491.

[4] Z. Wang, M. Lu, H.L. Li, and X.Y. Guo, "SWNTspolystyrene composites preparations and electrical properties" Research.Mater. Chem. Phys. 100 (1) (2006) 7781.

[5] J. Xiong, Z. Zheng, X. Qin, M. Li, H. Li, and X. Wang, "The thermal and mechanical properties of a polyurethane/multi-walled carbon nanotube composite" Carbon 44 (13) (2006) 27012707.

[6] K.P. Ryan, M. Cadek, V. Nicolosi, S. Walker, M. Ruether, A. Fonseca, J.B. Nagy, W.J. Blau, and J.N. Coleman ".Multiwalled carbon nanotube nucleated crystallization and reinforcement in poly (vinyl alcohol) composites" Synth. Met. 156 (2006) 332335.

[7] L. Qu, Y. Lin, D.E. Hill, B. Zhou, W. Wang, X. Sun, A. Kitaygorodskiy, M. Suarez, J.W. Connell, L.F. Allard, and Y.P. Sun, "Polyimide-functionalized carbon nanotubes: synthe-sis and dispersion in nanocomposite films" Macromolecules 37 (2004) 60556060.

[8] S.L. Ruan, P. Gao, X.G. Yang, and T.X. Yu,. "Toughening high performance ultra high molecular weight polyethylene using multiwalled carbon nanotubes" Polymer (Guildf) 44 (19) (2003) 56435654.

[9] Q. Zhang, S. Rastogi, D. Chen, D. Lippits, and P.J. Lemstra, "Low percolation threshold in single-walled carbon nanotube/high density polyethylene composites prepared by melt processing technique" Carbon 44 (2006) 778785.

[10] T. McNally, P. Pötschke, P. Halley, M. Murphy, D. Martin, S.E.J. Bell, G.P. Brennan, D. Bein, , P. Lemoine, and J.P. Quinn, "Polyethylene multiwalled carbon nanotube composites" Polymer (Guildf) 46 (2005) 82228232.

[11] P. Jindal, M. Goyal, and N. Kumar, "Mechanical characterization of multiwalled carbon nanotubes-polycarbonate composites" .Mater. Des. 54 (2014) 864868.

[12] T. Jin-hua, L. Guo-qin, C. Huang, and S. Lin-jian "Mechanical properties and thermal behaviour of LLDPE/MWNTs nanocomposites" Mater. Res. 15 (2012).

[13] M. Goyal, S.K. Kansal, N. Goyal, A. Khurana, G. Singh, and V. Dhar, "Preparation and characterization of multi-walled carbonnano tubes by liquid arc-discharge method" J. Phys. Chem. 3 (2015) 6264.

[14] S. Jandial, and P. Jindal, "Review of carbon nanotubes/poly(methyl methacrylate) composite fabrication and mechanical characterization techniques" Int. J. Res. Advent Technol 1 (2) (2014) 9294.

[15] P. Jindal, M. Goyal, and N. Kumar, "Modeling composites of multi-walled carbon nanotubes in polycarbonate" Int. J. Com-put. Methods Eng. Sci. Mech. 14 (6) (2013) 542551.

[16] Q. Zhao, and H.D. Wagner, "Raman spectroscopy of carbon-nanotube based composites" Philos. Trans. R. Soc. A Math. Phys.Eng. Sci. 362 (1824) (2004) 24072424.

Curr. Rep. Sci. & Tech. 3 (2017) 53-59

Synthesis and Stability Characteristics of Waste Sunflower Biodiesel

Sandip Bhatta[a], *Dr.Amit Sarin*[b] *and Rajbir singh*[c]
[a]*Department of Mechanical Engineering, Amritsar College of Engineering and Technology, Amritsar, Punjab, India.*
[b]*Department of physical science I.K.G. Punjab Technical University, Kapurthala, Punjab, India.*
[c]*Department of Mechanical Engineering, Amritsar College of Engineering and Technology, Amritsar, Punjab, India.*
Sandipbhatta707@gmail.com

Abstract

Due to the economic development of the world is highly dependent on nonrenewable fuel (fossil fuel) supplies which are constrained not only by limited availability but also generate high levels of pollution. The most promising alternative fuel will be the fuel that has the greatest impact on society. The major impact areas include well-to-wheel greenhouse gas emissions; non-petroleum feed stocks, well-to-wheel efficiencies, fuel versatility, infrastructure, availability, economics, and safety. Compared to some of the other leading alternative fuel candidates biodiesel appears to have the largest potential impact on society, and should be considered as the fuel of choice for eliminating the dependency on petroleum. The depletion of world petroleum reserves and the increased environmental concerns have been started to search for alternative sources for petroleum based fuel like biodiesel. Biodiesel is also reduce the levels of carbon dioxide production worldwide. Bio-fuels to replace fossil fuels will bring the advantages of reduced air pollution and reduced other environmental impacts of fossil fuels. Research in biodiesel production has been motivated by several reasons including consistent increase in prices of petroleum diesel, environmental advantages, security of fuel supply, and employment creation. This paper presents a review of one alternative technological method that can be used to produce this fuel. The possibility of using waste sunflower oil as fuel has been recognized, however, due to its high viscosities and low volatilities makes it inefficient for most combustion engines and thus the need to get them chemically altered or transesterified to obtain fatty alkyl esters of the oil (biodiesel) . The trans-esterification process is used for the production of Biodiesel (fatty acid monoalkayl ester) from waste sunflower oil mixed with methanol (CH_3OH) using potassium hydroxide (KOH) as a catalyst at a temperature of 60° c. This study proposed using waste sunflower oil as an effective way to reduce the raw material cost of producing biodiesel. Sample of waste oils were prepared from Spent Frying oil collected from local hotels and restaurants.

Keywords: Biodiesel; Waste sunflower Oil; methanol; alternative energy research; transesterification.

PACS: Replace this text with PACS numbers; choose from this list: http://www.aip.org/pacs/index.html

I. Introduction

Rapidly increase in the price of petroleum based fuel, the finite nature of fossil fuels, increasing concerns regarding environmental impact, mainly related to greenhouse gas (GHG) emissions, and health and safety [1]. Biodiesel has been touted as a viable alternative to the petroleum-derived fuels (diesel, petrol etc.) due to environmental concern and sustainability issue. There are lot sources of vegetable oil suitable for production of biodiesel such as sunflower oil, jatropha oil, mustard oil and some selected species of forest seeds [2]. In 1912 speech, Rudolf Diesel said: the use of vegetable oil as engine fuels may seem insignificant today, but such oils may become, in the course of time, as important as petroleum and the coal-tar products of the present time [3]. Recently there have environmental impact concerns and a decreasing cost differential made biomass fuels [4]. Biomass derived fuels such as biodiesel, ethanol, and biodiesel are best alternatives to diesel fuels as they are economically feasible, renewable, environmental-friendly and can be produced easily in rural areas where there is an acute need for modern forms of energy [5]. Edible vegetable oils such as sunflower, mustard have been used for biodiesel production and are proven diesel substitutes. To decrease the viscosity of vegetable oil we use Transesterification reaction. Biodiesel production by transesterification reaction in the presence of catalyst

(KOH) [6]. Some countries have so many advantages for biodiesel production because of greater availability of waste land, favorable environment for agriculture and labor cost is not much high like Nepal, India [7]. However, there are many other economic and environmental implications affecting the potential for developing countries to fulfill the increased global demand for biodiesel. In developed countries there is a growing trend towards employing modern technologies and bio-energy conversion using a range of bio fuels, which are becoming cost-wise competitive with petroleum based fuels [8] . From last three/four years, many scientist and student have investigated the economic and environmental impacts of the bio fuels, especially, biodiesel and found that biodiesel is less harmful than fossil fuel [9]. Resent research on bio-fuel is considerably focused on waste vegetable oils for biodiesel production. Production of Biodiesel is a very modern and technological area for researchers due to the relevance that it is winning everyday because of the increase in the price of petroleum product and the environmental advantages [10]. The successful introduction and commercialization of biodiesel in many countries around the world has been accompanied by the development of standards to ensure high product quality and high stability [11]. So in this paper we discuss about stability charactristics of waste sunflower biodiesel. The advantages of biodiesel as compare to diesel fuel are biodiesel is liquid in nature-portability, easily available, renewability, higher Cetane number, less content of sulfur and aromatic compound, and higher biodegradability [12]. Biodiesel offers safety benefits over diesel fuel because it is much less combustible. It has a higher Cetane number (around 50) than diesel fuel, and contains 11% oxygen by weight. The Cetane number determines the burning quality of fuel. The structure of fatty acid methyl ester (FAME) component, determines the Ignition quality of fuel [13].

A) Materials

Required quantities of waste sunflower oil are purchased from local restaurants and oil mill near Amritsar, Punjab State, India. All chemicals such as methanol, KOH pellets had purchased from renewable energy laboratory, Amritsar college of Engineering and technology, Amritsar, Punjab State, India. All chemicals were of analytical grade. For the determination of acid number, Isopropyl alcohol was used in which Phenolphthalein was used as an indicator in the titration

B) Methods

According to chemistry, acid value is the mass of potassium hydroxide (KOH) in milligrams that is required to neutralize one gram of chemical substance. The acid value of any oil calculated by using formula

Acid number =0.1N*molecular weight of catalyst *volume of catalyst used/mass of sample oil.

The acid values (KOH mg/g) were determined by a standard titrimetry method. The experimental result in terms of the acid number is 2.35 for waste sunflower oil hence oil is suitable for production of biodiesel then the oil was taken. The oil was poured in a beaker and heated to 60 degree centigrate by using heater. In the meantime 2 to 2.5% potassium hydroxide (KOH) and 15% methanol was poured in other beaker and stirred to make it perfect solution. After this the solution was poured in oil and heated at constant temperature of 60ºC for one hour. After one hour this solution was poured in seperation flask for 12 hours undisturded.The seperation of methyl esters and glycerine takes place. After which glycerine and methyl esters were seperated. The water at 45 degree centigrate was poured in methyl esters for 2-3 hours for washing process. This process was repeated for 4-5 times in order to remove all the impurities. The obtained methyl esters were heated at 110ºC degree centigrate in order to evaporate the excess methanol and water from the solution.

Chemical Reaction

In this process glyceride is react with alcohol in the presence of

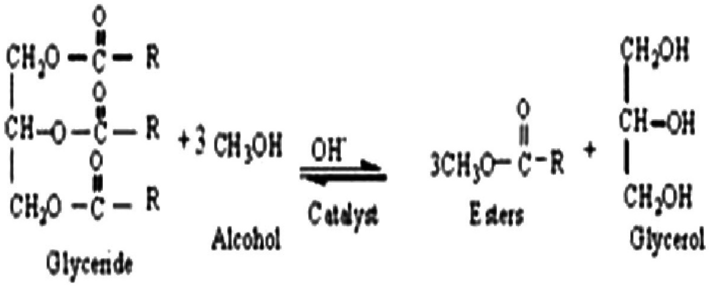

Fig. 1 Transesterification reaction

catalyst (KOH). This has been widely used to reduce the viscosity of the triglycerides. Thus fatty acid methyl ester (also known as biodiesel) is obtained by transesterification. The transesterification is expressed by the following reaction.

II. Result

The waste sunflower methyl ester was synthesized from waste sunflower oil and then its stability characteristics were studied using professional Biodiesel Rancimat 893.After the process of Rancimat, the time versus conductivity graph is obtained, which shows that stability of waste sunflower biodiesel derived from waste sunflower oil is 2.21Hours.

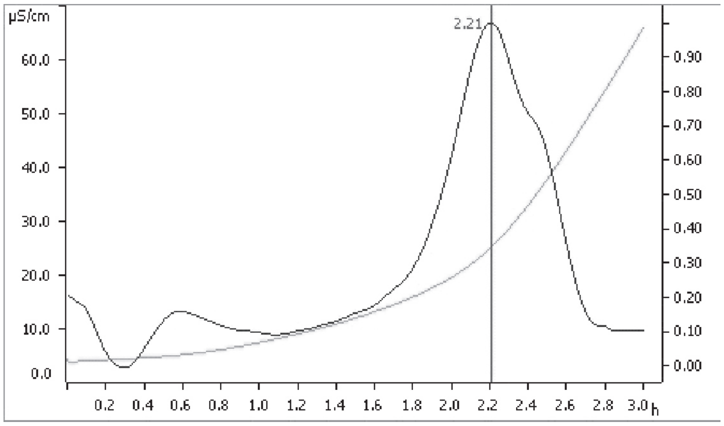

Fig. 2. The graph showing oxidation stability of waste sunflower biodiesel as 2.21 h.

III. Conclusion

In this experiment, the waste sunflower was used as a feedstock and waste sunflower Methyl ester was obtained by the Transesterification of waste sunflower oil. The Oxidation Stability of waste sunflower Biodiesel was tested in Professional Biodiesel Rancimat 893 and it is concluded that:

Biodiesel can be produced from waste sunflower oil using transesterification reaction. Waste sunflower biodiesel showed the Oxidation Stability of 2.21 hours. The Oxidation Stability of waste sunflower Methyl Ester can be increased by using Artificial Antioxidants like TBHQ, TBHT, PG, PY, BHT and BHQ. This experiment also motivates to use natural resources which are less expensive, easy available and environment Friendly. It is possible to run diesel engine with biodiesel blends. It has become clear that when it manages to integrate the production of biodiesel with the other value-added products and integrating with other pollutants and hotel, restaurant with large oil wastes, could bring significant economic benefits. It emits less pollution compare to fossil fuel.

IV. Acknowledgments

The authors express their gratitude to the Department of Research and Development, New Delhi, India for the grant. We also gratefully acknowledge Dr. Rajnish Arora and Madan Paudel for his comments and suggestions.

V. References

[1] S. Prasad, A. Singh, H. C. Joshi, “Ethanol as an alternative fuel from agricultural, industrial and urban residues, Resources”, Conservation and Recycling, vol.50, pp. 139, July 2007

[2] Y. Reyes, G. Chenard, D. Aranda, C. Mesquita, M. Fortes, R. Joao, L. Bacellar, “Biodiesel production by hydro-esterification of microalgae biomass using heterogeneous catalyst”, Natural Science, vol. 4, pp. 778-783, September 2012.

[3] M. Yunus, M. Alsoufi, I. Hussain, “Study and Analysis of Performance Characteristics of Biodiesel Formed by Different Blends of Honge and Mustard Oil using 4 Stroke C.I. Engine”, International Journal of Emerging Research in Management &Technology, vol.4, pp. 220-227, July 2015.

[4] P. Ravindra, S. Saralan, R. Abdulla, “LCA studies for alkaline and enzyme catalyzed biodiesel production from palm oil”, Advances in Biological Chemistry, vol.2, pp. 341-352, November 2012.

[5] V. R. Kattimani, B. M. Venkatesha, S. Ananda, “Biodiesel Production from Unrefined Rice Bran Oil through Three-Stage Transesterification”, Advances in Chemical Engineering and Science, vol.4, pp. 361-366, July 2014.

[6] X. Chen, G. He, Z. Deng, N. Wang, W. Jiang, S. Chen, “Screening of

Microalgae for Biodiesel Feedstock", Advances in Microbiology, vol. 4, pp. 365-376, May 2014.

[7] J. Gimbun, S. Ali, C. Charan, S. C. Kanwal, L. A. Shah, N. H. M. Ghazali, C. K. Cheng, S. Nurdin, "Biodiesel Production from Rubber Seed Oil Using a Limestone Based Catalyst", Advances in Materials Physics and Chemistry, vol. 2, pp. 138-141, December 2012.

[8] B. K. Abdalla, F. O. A. Oshaik, "Base-transesterification process for biodiesel fuel production from spent frying oils", Agricultural Sciences, vol. 4, pp. 85-88, August 2013.

[9] C. Lin, M. Hsiao, P. Liao, "Ultrasonic-Assisted Production of Biodiesel from Waste Frying Oil Using a Two-Step Catalyzing Process", Journal of Sustainable Bio-energy Systems, vol. 2, pp. 117-121, December 2012.

[10] S. Rajvanshi, M. P. Sharma, "Microalgae: A Potential Source of Biodiesel", Journal of Sustainable Bio-energy Systems, vol. 2, pp. 49-59, September 2012.

[11] U. Krishnakumar, V. Sivasubramanian, "Optimization of Lab-Scale Preparation of Biodiesel from Rubber Seed Oil Using Modified Calcium Oxide as Catalyst", Journal of Sustainable Bio-energy Systems, vol. 6, pp. 55-65, September 2016.

[12] B. S. Santos, S. C. Capareda, J. A. Capunitan, "Engine Performance and Exhaust Emissions of Peanut Oil Biodiesel", Journal of Sustainable Bio-energy Systems, vol. 3, pp. 272-286, December 2013.

[13] Y. K. Turinayo, F. Kalanzi, J. M. Mudoma, P. Kiwuso, G. M. Asiimwe, J.F.O. Esegu, P.Balitta, C. Mwanja, "Physicochemical Characterization of Jatropha curcas Linn Oil for Biodiesel Production in Nebbi and Mokono Districts in Uganda", Journal of Sustainable Bio-energy Systems, vol. 5, pp.104-113,september 2015.

Curr. Rep. Sci. & Tech. 3 (2017) 60-66

Investigation of the Structural Properties of Polyaniline-Cobalt Ferrite (PA-$CoFe_2O_4$) composite

Sonika Thakur[a], Manpreet Kaur[a], Simranjeet Kaur[a], Satveer Singh[b] and Lakhwant Singh[b]
[a]Department of Physics, Guru Nanak Dev University College Verka, Amritsar, Punjab, India
[b]Department of Physics, Guru Nanak Dev University, Amritsar, Punjab, India
lakhwant@yahoo.com

Abstract

In the present investigation, Polyaniline-$CoFe_2O_4$ composites with different contents of $CoFe_2O_4$ (0.2 and 0.6 wt %) have been synthesized via in situ chemical oxidation polymerization. The synthesized composite material has been characterized by FTIR and Raman spectroscopic studies to infer the structural changes brought about by the introduction of $CoFe_2O_4$ in the polymer matrix. FTIR results confirm the presence of $CoFe_2O_4$ and polyaniline in all samples. Significant structural modifications induced in the polymer matrix with addition of $CoFe_2O_4$ has been observed and discussed in this manuscript.

Keywords: Polyaniline; Composite materials; FTIR; Raman.
PACS: 81.05.Qk; 75.50.Gg; 78.30.Ly.

I. Introduction

Polyaniline (PA) is a conducting polymer widely studied because of its facile preparation, good environmental stability, processibility, and wide range of tunable optical and electrical properties [1-5]. The composites of PA containing nanoparticles are frequently investigated due to their exclusive electrical and magnetic characteristics. Metal oxides with the spinel structure constitute a special class of materials displaying a large variety of interesting electrical, optical, and magnetic properties [6]. Among magnetic materials, spinel ferrites with a general structure of $[M^{2+}]$tet$[Fe^{3+}]$ octa O4 exhibit remarkable electrical, magnetic, and catalytic characteristics [7-9]. Cobalt ferrite ($CoFe_2O_4$) belongs to the group of spinel-type ferrites and is one of the extremely technologically important ferrites due to its high coercivity, very high magneto crystalline anisotropy, chemical stability, moderate magnetization, and mechanical hardness [10-13].

Recent investigations on $CoFe_2O_4$ have suggested that it can be a suitable material for the development of new technologies in the areas of critical importance [14]. In addition, cobalt ferrite containing composites have been found to exhibit an enhanced magneto-electric effect and a large magneto-optical effect [15,16]. Indeed many publications have appeared in the literature on the nanocomposites of PA with magnetic nanoparticles recently [17,18], still there are very few studies on PA-$CoFe_2O_4$ [19]. Therefore, the present study reports the synthesis, characterizations and effects of spinal ferrites addition on structural properties of polyaniline.

II. Experimental Details

Aniline monomer, procured from Sigma-Aldrich, was distilled twice before use. All other chemicals used were of AR grade. De-ionized water was used throughout the synthesis. The detailed synthesis of polyaniline has been discussed elsewhere [20]. The synthesis of PA- $CoFe_2O_4$ mixture was carried out in accordance to the description listed in Table 1.

Table 1. Composition and coding of prepared samples.

Sample Code	**Polyaniline (wt %)**	**$CoFe_2O_4$ (wt %)**
S_0	100	0
$S_{0.2}$	99.8	0.2
$S_{0.6}$	99.4	0.6

Fourier transformed infrared spectra were recorded in transmission mode using a Perkin-Elmer Fourier Transform Spectrophotometer. The prepared powder samples were finely grounded with potassium bromide (KBr) and compressed into pellets. The FTIR spectra in the range 400-4000 cm^{-1} were measured in order to observe the nature of the chemical bonds formed. Raman spectra of the samples under investigation were recorded using Renishaw In Via Reflex Micro Raman spectrometer over the spectral range 50-2000 cm^{-1} at room temperature.

III. Results & Discussion

FTIR Analysis

Fig 1. displays the FTIR spectra of PA and PA-$CoFe_2O_4$ mixtures. All characteristic bands of polyaniline can also be identified in the IR spectra of the composite material affirming the formation of polyaniline in all samples. The peaks at 1475 cm^{-1} and 1560 cm^{-1} are assigned to the characteristic C=C stretching of the benzenoid and quinoid rings. The peak at 1300 cm^{-1} and 1236 cm^{-1} are attributed to C-N stretching of the benzenoid ring. The peak at about 799 cm^{-1} is assigned to the out of plane deformation of C-H in the p-disubstituted benzene ring [19].The band observed at 1125 cm^{-1} is attributed to in plane bending vibration of C-H mode. For composite samples, there is a broad metal-oxygen (Fe-O) stretching band observed at about 580 cm^{-1} which represent characteristic features of spinel ferrites in single phase. The peak at 1125 cm^{-1} of polyaniline has been shifted to lower wave number in composite samples. Moreover, two new bands at 2852 cm^{-1} and 2310 cm^{-1} have also been observed in the composite samples. The observed results suggest to the presence of some interaction between polyaniline chains and metal ferrite particles.

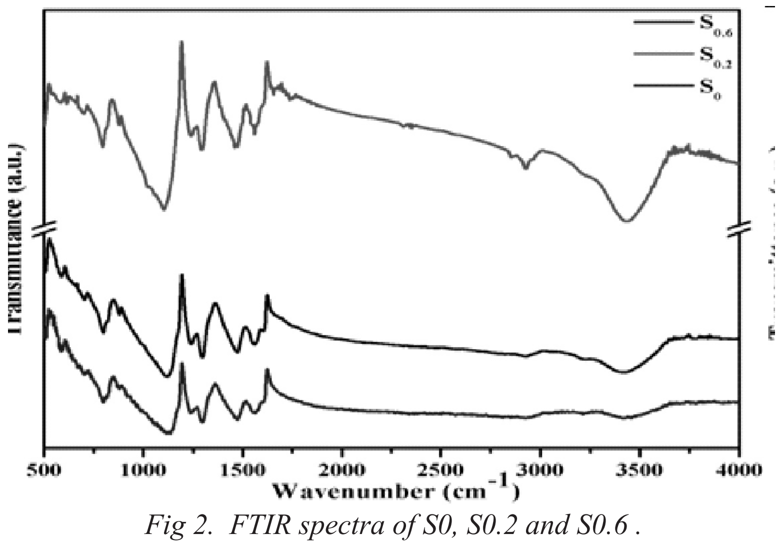

Fig 2. FTIR spectra of S0, S0.2 and S0.6 .

Raman Analysis

Fig 2. shows the Raman spectra of PA and PA-$CoFe_2O_4$ mixtures. The bands at 1580 cm^{-1} and 1348 cm^{-1} are named as graphite like G and disorder

D bands of the disordered carbon structure. The G band is due to in-plane vibrations of sp^2 bonded carbon atoms whereas the D band is a result of out of plane vibrations employed to the presence of structural defects. It has been found from the Raman analysis that firstly the intensity of bands increases with introduction of spinal ferrites and further addition results in overall decrease in the intensity of bands. This decline in intensity may be due to significant creation of unsaturated bonds and the formation of gap states through which electron hole pairs can recombine [21]. The observed result proposes noticeable structural modifications in the polymer matrix due to incorporation of ferrite particles.

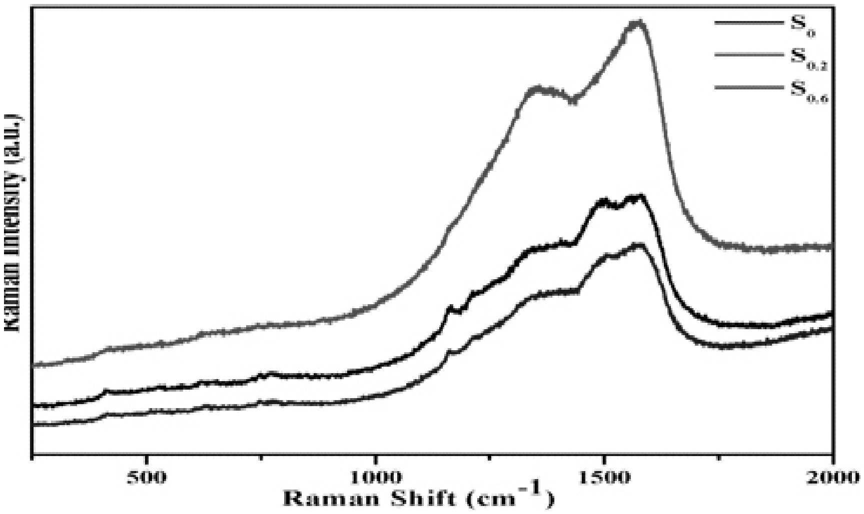

Fig 3. Raman spectra of S0, S0.2 and S0.6 .

IV. Conclusions

In this study, PA-$CoFe_2O_4$ composites have been successfully prepared by in situ polymerization. The combined results of FTIR and Raman have been suggesting to the presence of some interaction between polyaniline and ferrite particles. The addition of cobalt ferrite particles do not affect the backbone structure of polyaniline is concluded from the FTIR studies, referring the presence of $CoFe_2O_4$ as a spinel in the polymer matrix. The results obtained suggest to that different properties can be tailored in the composites by mixing appropriate proportions of polyaniline and ferrite particles.

V. Acknowledgment

The authors wish to thank the Department of Physics and Chemistry, Guru Nanak Dev University, Amritsar, for providing the FTIR and Raman facility.

VI. References

[1] T. H. Qazi, R. Rai, D. Dippold, J. E. Roether, D. W. Schubert, E. Rosellini, N. Barbani, and A. R. Boccaccini, "Development and characterization of novel electrically conductive PANI-PGS composites for cardiac tissue engineering applications," Acta Biomater. 10 (2014) 2434-2445.

[2] I. Duboriz, A. Pud, "Polyaniline/poly (ethylene terephthalate) film as a new optical sensing material," Sens. Actuators B 190 (2014) 398-407.

[3] S. Pramodini, P. Poornesh, Y. N. Sudhakar, M. S. Kumar, "$\chi(3)$ and optical power limiting measurements of Polyaniline and its derivative Poly (o-toluidine) under CW regime," Opt. Commun. 293 (2013) 125-132.

[4] Y. Min, Y. Liu, Y. Poojari, J. C. Wu, B. E. Hildreth, T. J. Rosol, A. J. Epstein, "Self-doped polyaniline-based interdigitated electrodes for electrical stimulation of osteoblast cell lines," Synth. Met. 198 (2014) 308-313.

[5] H. Niu, S. Qin, X. Mao, S. Zhang, R. Wang, L. Wan, J. Xu, and S. Miao, "Axle-sleeve Structured MWCNTs/Polyaniline Composite Film as Cost-effective Counter-Electrodes for High Efficient Dye-Sensitized Solar Cells," Electrochim. Acta 121 (2014) 285-293.

[6] M. J. Iqbal, B. Ismail, "Electric, dielectric and magnetic characteristics of Cr^{3+}, $Mn^{3+}$and Fe^{3+} substituted $MgAl_2O_4$: Effect of pH and annealing temperature," J. Alloys Compd. 472 (2009) 434-440.

[7] P. Siwach, S. Singh, and R. K. Gupta, "Vapor phase alkylation of indole with ethanol and dimethylcarbonate over NiMn based ferrospinels," Catal. Commun. 10 (2009) 1577-1581.

[8] A. R. Shyam, R. Dwivedi, V. S. Reddy, K. V. R. Chary and R. Prasad, "Vapour phase methylation of pyridine with methanol over the $Zn_{1-x}Mn_xFe_2O_4$ (x = 0, 0.25, 0.50, 0.75 and 1) ferrite system," Green Chem. 4 (2002) 558-561.

[9] S. V. Reddy, S. A. Radhe, R. Dwivedi, R. K. Gupta, V. R. Chumbale and R. Prasad, "Ortho-selective vapour phase methylation of phenol over nanocrystalline ferrospinels of varying Zn^{2+}/Mn^{2+}ionic composition," J. Chem. Technol. Biotechnol. 79 (2004) 1057-1064.

[10] S. D. Bhame, P. A. Joy, "Magnetic and magnetostrictive properties of manganese substituted cobalt ferrite," J. Phys. D: Appl. Phys. 40 (2007) 3263.

[11] S. A. Chambers, R. F. C. Farrow, S. Maat, M. F. Toney, L. Folks, J. G. Catalano, T. P. Trainor and G. E. Brown Jr., "Molecular beam epitaxial growth and properties of $CoFe_2O_4$ on MgO (001)," J. Magn. Magn. Mater. 246 (2002)124-139.

[12] M. S. Khandekar, R. C. Kambale, J. Y. Patil, Y. D. Kolekar and S. S. Suryavanshi, "Effect of calcination temperature on the structural and electrical properties of cobalt ferrite synthesized by combustion method," J. Alloys Compd. 509 (2011) 1861-1865.

[13] M. C. Terzzoli, S. Duhalde, S. Jacobo, L. Sterenand, and C. Moina, "High perpendicular coercive field of $CoFe_2O_4$ thin films deposited by PLD," J. Alloys Compd. 369 (2004) 209-212.

[14] M. A. Ahmed, N. Okasha, S. F. Mansour, S. I. El-dek, "Bi-modal improvement of the physico-chemical characteristics of PEG and MFe_2O_4 subnanoferrite," J. Alloys Compd. 496 (2010) 345-350.

[15] J. Ryu, S. Priya, K. Uchino and H. Kim, "Magnetoelectric Effect in Composites of Magnetostrictive and Piezoelectric Materials," J. Electroceram. 8 (2002)107-119.

[16] F. Cheng, C. Liao, J. Kuang, Z. Xu, C. Yan, L. Chen, H. Zhao and Z. Liu, "Nanostructure magneto-optical thin films of rare earth (RE = Gd,Tb,Dy) doped cobalt spinel by solgel synthesis," J. Appl. Phys. 85 (1999) 2782.

[17] Z. Durmus, A. Baykal, H. Kavas, and H. Sozeri, "Preparation and characterization of polyaniline (PANI) Mn_3O_4 nanocomposite," Physica B: Condens. Matter 406 (2011) 1114-1120.

[18] G. D. Prasanna, H. S. Jayanna and V. Prasad, "Preparation, structural, and electrical studies of polyaniline/$ZnFe_2O_4$ nanocomposites," J. Appl. Polym. Sci. 120 (2011) 2856-2862.

[19] E. E. Tanrıverdi, A. T. Uzumcu, H. Kavas, A. Demir, A. Baykal, "Conductivity Study of Polyaniline-Cobalt Ferrite (PANI-$CoFe_2O_4$) Nanocomposite," Nano-Micro Lett. 3 (2011) 99-107.

[20] S. Thakur, A. Singh and L. Singh, "Structural and electrical properties of self-standing polyaniline films modified with gold nanoparticles," Adv. Mater. Lett. 6 (2015) 840-846.

[21] Y. Ali, V. Kumar, R. G. Sonkawade and A. S. Dhaliwal, "Effect of swift heavy ion beam irradiation on Au-polyaniline composite films," Vacuum 90 (2013) 59-64.

Curr. Rep. Sci. & Tech. 3 (2017) 67-75

Optical Properties of Bismuth Borate glasses

Simranjeet Kaur[a] *Sonika Thakur*[a], *Manpreet Kaur*[a], *Satvir Singh*[a]
and Anupinder Singh[b]
[a]*Department of Physics, Guru Nanak Dev University College Verka, Amritsar, Punjab, India*
[b]*Department of Physics, Guru Nanak Dev University, Amritsar, Punjab, India*
thakur.sonika7@gmail.com

Abstract:

Samples of bismuth borate glasses with different Bi_2O_3/B_2O_3 ratios $(xBi_2O_3(1- x)B_2O_3)$, $75B_2O_3.(25\text{-}x)\ Bi_2O_3.xR$.have been synthesised by using melt quenching technique. The structure analysis from XRD indicates that glass samples have pure amorphous, non crystalline structure; the absence of sharp peak indicates the amorphous nature of glass samples. UV-Vis spectroscopy measurements have been performed on the samples to study the optical properties of the samples which shows that optical band gap Eg decreases whereas urbach energy increases by adding the rare earth series like samarium and dysprosium.

Keywords: Glass, Bismuth Borate, Rare earth oxides, Structure analysis, absorption, band gap energy

PACS: 61.05.C-;82.80.Dx;61.43.-j

I. Introduction

Glasses are super cooled liquids, transparent and amorphous in nature. Glasses containing bismuth borate (Bi_2O_3) with a high refractive index are promising material for advance optical and telecommunication and processing devices [1]: B_2O_3 has low melting temperature and high thermal stability which makes the excellent glass former Heavy metal oxide glasses containing bismuth are used in scintillation detector for high energy physics. Rare earth doped bismuth borate glasses shows the luminescence property due to 4f -4f and 4f-4d electronical transitions in the visible light range [2]: Rare earth (RE) ion doped glasses have been investigated for their optical electrical and magnetic properties. These properties confer to them important applications in many fields such as laser technology ,optical communication fiber, light convertor, sensors etc[3-5]:In the recent year glasses doped with rare earth ions have drawn much attention due to their potential applications in solid state laser, optical amplifier, sensors and optical data storage devices[6]: The Dy^{3+} doped borate glasses are the candidate materials for yellow lighting applications in the visible range by studying optical properties[7]:and the Sm^{3+} doped alkaline earth borate glasses are suitable material for UV to visible photon conversion layer for solar cell application[8]:The present work intends to give a description of the optical properties of the bismuth borate glass doped with rare earth elements .

II. Experimental

The undoped bismuth borate xBi_2O_3 (1-x) B_2O_3 and RE-doped samples $(75\text{-}x)B_2O_325Bi_2O_3.xRE$ were prepared by melt quenching technique [9]:Rare earth oxides (Sm_2O_3 and Dy_2O_3) were added (0.5 wt %) to the bismuth borate glass. The weighted quantities of the chemicals were mixed in an agate pestle mortar for one hour. The mixture was melted in alumina crucibles in an electric furnace at 11000C for 2 hours. Then melt was poured into heated graphite moulds of required dimensions. The prepared samples were immediately transferred to furnace which was at 400 for annealing. The furnace was switched off after 2 hours and the glass samples were allowed to remain in the furnace for 12 hours. The samples were finally grinded and polished with different grades of silicon carbide (SiC) emery papers. These prepared samples were then further employed in various studies.

III Characterization

X-Ray diffraction (XRD) studies were performed in order to confirm

Table 1. Composition and coding of prepared samples

Sample Code	Code	Sample	Bi_2O_3 (wt%)	B_2O_3 (wt%)	Dy_2O_3	Sm_2O_3
S_1	S_{1s}	S_1	25	75	0	0
S_2	S_2	S_2	25	72	3	0
S_3	S_3	S_3	25	72	0	3

the amorphous or crystalline nature of prepared samples. X- ray diffraction pattern consisting of sharp diffraction peak corresponds to the crystalline nature of the sample where as the absence of sharp diffraction peak and the presence of broad hump in the pattern indicate the amorphous nature of the sample. In the present work, the X-Ray diffraction patterns for the prepared samples were recorded at the room temperature using Cu-Kα radiations (λ= 1.5418Å) in XRD 7000 Shimadzu X Ray defractrometer at a scanning rate of 2^0 per minute.

For optical properties characterization technique, the fabricated glasses were polished by silicon carbide paper of different grid. Then sample was placed in the sample holder of UV-Vis Spectrometer (Shimadzu). The light source from Xenon light flash was used for characterization process where the optical absorption spectra in the range of 220 to 2600nm were recorded.

IV. Results & Discussions

X-ray Diffraction Analysis

Fig. 1 shows the XRD patterns of undoped and RE doped bismuth borate glass samples. The presence of broad hump indicates that the prepared samples do not have long range periodic lattice arrangement. The

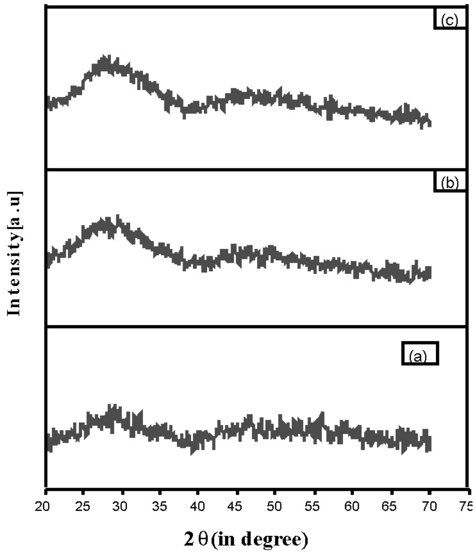

Fig 1. XRD diffraction patterns of (a) S1, (b) S2 and (c) S3 samples.

absence of sharp defined peaks in the given XRD patterns validates the amorphous nature of prepared samples [10]: Since the glasses do not have uniformly space planes of atoms, thus no sharp diffraction pattern will be observed.

UV Analysis

The UV-Vis. optical absorption spectra for the glass samples show that there is an increase in absorption by adding rare earth elements, samarium and dysprosium. The absorption coefficient has been calculated by the relation [11]:

$$\alpha = A/t \tag{1}$$

Where't' is the thickness of the sample and 'A' is the absorbance.

From the Fig 2, the spectra consist of a various absorption level corresponding to the transition between the ground state and the higher energy state. The absorbance peaks of sample S_2 lie at 452 nm, 755 nm, and 803 nm respectively whereas the absorbance peak of sample S_3 lie at 404 nm which suggests that the absorption intensity increases by adding rare earth series. These absorption peaks are due to the presence of few impurities [12]:

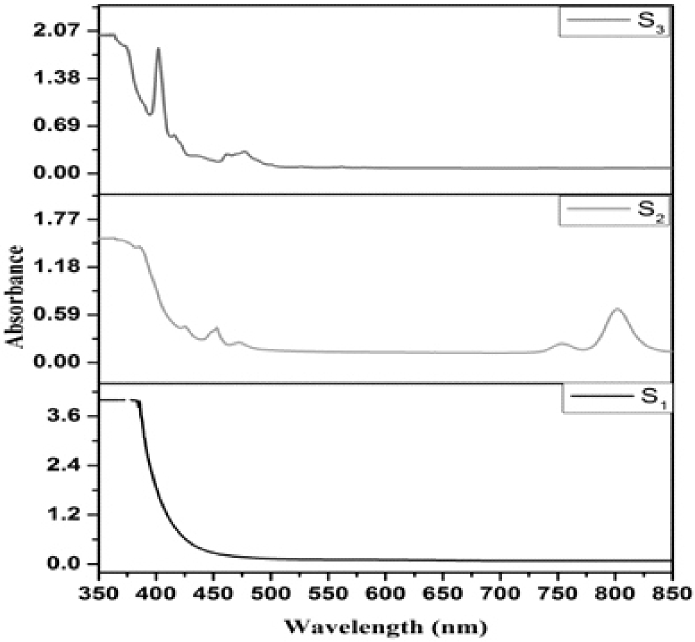

Fig 2. UV spectra of a) S1, (b) S2 and (c) S3 samples.

Tauc's plots have been used for the determination of the optical band gap energies of the samples using the relation [13,14]:

$$\alpha h\nu = B\,(h\nu - E_g)^n \tag{2}$$

where B is the band tailing parameter, hν is the incident photon energy and n is a constant that determine the type of optical transitions . The optical band gap energy provides information about the nature of the chemical bonds and the glass structure. In the present work, indirect optical band gap energies (E_g) have been calculated by using n=2. The plots between $(\alpha h\nu)^{1/2}$ and (hν), known as Tauc's plot have been employed to calculate the optical band gap energies of the synthesized samples.

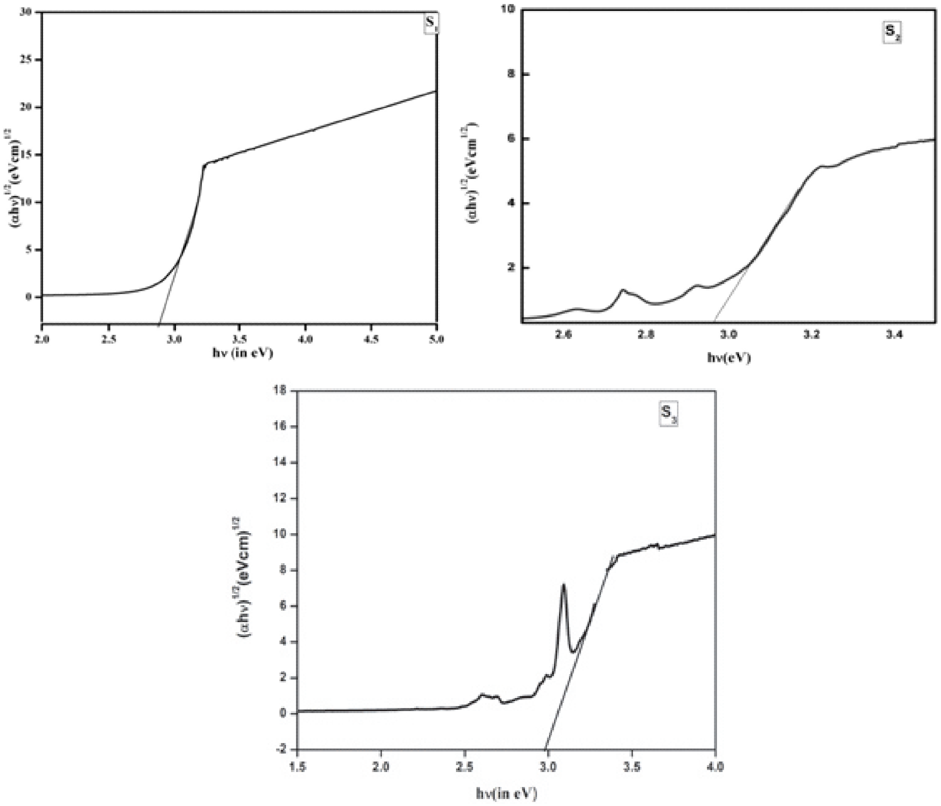

Fig. 3- Tauc's plot for (a) S1 (b) S2 (c) S3 Samples

Fig. 3 shows the Tauc's plot for the samples. The values of band gap energy Eg obtained from the plots are given in Table 2. From the Table 2, it is observed that the band gap energy Eg of rare earth doped glass sample is greater than the Undoped glass sample but band gap decreases by adding rare earth series. The defects are formed in the glass structure by adding the rare earth element so the value of E_g decreases. This decrease in values of E_g may be attributed to the structural changes occurring in the glass system due to addition of rare earth series.

Table2.The variation of band gap energy (Eg), and Urbach energy of undoped and RE doped bismuth borate glass samples.

Sample No	E_g (eV)	ΔE (eV)
S_1	2.89	0.43
S_2	2.95	0.47
S_3	3.07	0.44

The Urbach energy is defined as the energy gap between localized tail states in the forbidden band gap [15]: It provides a measure of disorder in the amorphous and crystalline solids. In the amorphous material, short range of periodic lattice arrangement is linked to the tailing of the density of states into the forbidden energy band [16]: The width of band tails, also known as Urbach energy (E), originating from the electron transition between localized states. Urbach energy (E) is a measure of defects concentration. Materials with higher value of Eu will have higher chance to transform weak bond into defect [17]: E is calculated by the following equation [18]:

$$\alpha(\nu) = B \exp \frac{h\nu}{\Delta E} \tag{3}$$

where B is a constant, hν is the photon energy and α(ν) is the absorption coefficient.

Urbach energy (E) values are determined by taking the reciprocal of the slopes of linear regions of the plots ln α versus hν listed in Table 2.The urbach energy refers to the width of the exponential absorption edge [19]:The increase in the value of E by adding the rare earth series associates with increase number of defects in glass matrix. Defect that produce in the glass network , for instance increasing number of non bridging oxygen and cation-anion vacancy pair, might be the reason behind the increment of E [20]:

V Conclusions

The Dy^{3+} and Sm^{3+} doped bismuth borate glasses have been prepared and characterized for their structural and optical properties. The prepared samples are of amorphous nature, as indicated by XRD results. A decrease in the band gap after adding the rare earth series indicates the defects formation in the glass matrix. The increase in Urbach energy occurs due to incorporation of rare earth elements in glass system that leads to the more creation of non bridging oxygen atoms.

VI Acknowledgement

The authors wish to thank the department of Physics GNDU Amritsar, for providing the XRD or UV/VIS facility.

VI References

[1] Sugimoto,N.J Amer Ceram Soc, " Ultrafast optical Switches and wavelength Division Multiplexing Amplifiers Based on bismuth Oxide Glasses," J. Amer Cer Soc 85 (2002),1083-1088

[2] J. M. Park, H.J Kim,Sunghwan Kim, P.Limsuwan, J.Kaewkhao, " Luminescence properties of Rare eath doped bismuth borate glasses", Procedia Engineering 32(2012) 855-861

[3] C.H.Kam,S.Buddhudu, " Emission analysis of Eu3+: Bi_2O_3- B_2O_3-R_2O (R= Li,K,Na) Glasses" J. Quant. Spectrosc. Radiat. Transfer 87 (2004) 325-337

[4] Y. G Choi, B .J Park, K.H Kim, J.Heo "Crossrelaxation between multiphonon relaxation of near infrared-excited states of Pr 3+ ions in Selenide Glasses" Chem Phys Lett 368(203) 625-629.

[5] I.M.G Dos Santos, R.C.M Moreira, A.G.D. Souza, R.Lebullengar, A.C Hernandes, E.R Leite, C.A. Paskocima, E Longo, "Ceramic crucibles:a new alternative for melting of PbO-BiO1.5 GaO1.5 Glasses" J .Non-Cryst Solid, 319(2003) 304-310

[6] M. Venkateswarlu and B.H. Rudramadevi, "Special analysis of europium doped borate zinc magnessium glass", Int.J.Chem tech Res 7(2015) 607-612

[7] K. Venkata Rao, S. Babu, G.Venkataiah, Y .C.Ratnakaram"Optical Spectroscopy of Dy^{3+} doped borate glasses for luminenscence application",J.Mole.lar Structure 1094 (2015) 274-280.

[8] L. F. Shen, B.J.Chen, E.Y. B Pun,H. Lin,"Sm3+ doped alkaline earth

borate glasses as UV-Visible photon conversion for solar cells", J. Lumin 160 (2015) 138-144.

[9] L. Singh,V.Thakur,R.Punia, R.S. Kundu,A.Singh,' 'Structural and optical properties of barium titanate modified bismuthborate glasses" Solid State Sci. 37 (2014) 6471.

[10] S. Thakur,A. Singh and L. Singh, “Structural and Electrical properties of self-standing Polyaniline films modified with gold nanoparticles,” Adv. Mater. Lett. 6 (2015) 840-846.

[11] R.S Kundu, Sunil Dhankhar , R. Punia, Kirti Nanda, N. Kishore,"Bismuth Modified physical,structural and optical properties of mid-IR transparent zinc boro- tellurite glasses".J. Appl Phy, 587 (2014) 66-73.

[12] D. Kothandhan, R.Jeevan Kumar,"Optical properties of Rare Earth doped Borate Glasses”, Int.J.Chem tech Res, 14(2015) 310-314

[13] R. Punia, R. S.Kundu, J. Hooda,S. Dhankhar, S. Dahiya, N. Kishore,"Effect of Bi2O3 on structural,optical and physical properties of semiconducting zinc vanadate glasses". J.Alloys Compd, 110(2011) 033527

[14] K .S .Samra, S.Thakur.L. Singh ,“ Photoluminescent and thermal behaviour of 120 Mev silicon and 84 Mev oxygen ion irradiated PVDC” J. Lumin, 131(2011) 684-694

[15] C. R. Kesavulu, K. K Kumar, N.Vijaya, Ki-Soo Lim, C. K. Jayasankar, “Thermal, Vibrational,optical properties of Eu3+ doped lead flurophosphate glasses for red laser applications”.Mat.Che.Phy. 14 (2013) 903-911.

[16] L. M. S. El-Dean, M. S. A. Salhi, and M. M. Elkholy,"IR and UV spectral studies for rare earths doped tellurite glasses," J. Alloys Compd. 465 (2008) 333-339.

[17] S.E L-Rabaie,T. A.Taha, and A. A. Higzy,"Non- linear optical and electrical properties of germanate glasses"Physica B: Conden Matter, 429(2013) 1-5

[18] K .S .Samra, S.Thakur.L. Singh ,“ Photoluminescent and thermal behaviour of 120 Mev silicon and 84 Mev oxygen ion irradiated PVDC” J. Lumin, 131(2011) 684-694

[19] M. Caglar, S. Ilican, Y. Calgan, Y. Sahin, F. Yakuphanoglu and D. Hur,

“A Spectro Electrochemical Study on SingleOscillator Model and Optical Constants of Sulfonated Polyaniline Film,”, Spectrochim.Acta.Mol.71(2008), 621-627.

A. Azuraida,M. K.Halimah, C. A. C. Azurahanim, and M. ishak, "Gamma Irradiations effect on structural and optical properties of bismuth boro tellurite glasses,” Adv.Mat.Res.1107(2015). 426-431.

Curr. Rep. Sci. & Tech. 3 (2017) 76-90 © Khalsa College Amritsar

Thiazolidine-2, 4-diones- Synthesis and Anti-diabetic properties

Ranjit Singh and M. S. Batra
Post Graduate College of Chemistry, Khalsa College, Amritsar, Punjab-143001.
ranjitgill63@gmail.com; msbatra_99@yahoo.com.

Abstract

The last three decades have witnessed an enormous work on the synthesis and biological activities of thiazolidine ring compounds. Thiazolidine-2, 4-diones have emerged as an important scaffold, possessing a wide range of promising biological activities. Some of these derivatives have shown superior antidiabetic activity than standard drugs and so have the potential of providing better drugs for the market in future. In this review, we have compiled the synthesis and antidiabetic properties of variousthiazolidine-2, 4-diones.

I. Introduction

Thiazolidine-2, 4-diones (TZDs) are the active skeleton of insulin sensitizing drugs. In addition, these are also known for their wide array of biotic actions such as anti-inflammatory, anti-tubercular, anti-microbial, cytotoxic and anti-oxidant activities. TZDs act as oral anti-diabetic drug, for the treatment of type 2 diabetes mellitus (T2DM), (the most predominant diabetes types).1 They are believed to increase insulin sensitivity by activating the peroxisome proliferator-activated receptor γ (PPAR-γ), also famous as the glitazone receptor, which regulates fatty acid storage and glucose metabolism. This brief review summarizes structure, synthesis and antidiabetic properties ofthiazolidine-2, 4-diones.

II. Structure of thiazolidine-2, 4-diones

Thiazolidine (1) is a saturated five membered heterocyclic organic compound containing thioether (-S-) and amine (NH) groups at 1st and 3rd positions, respectively. Thiazolidine-4-ones have a carbonyl group at 4th position (2) whereas thiazolidine-2, 4-diones (3), has two carbonyl groups in the 2nd and 4th positions as shown below.

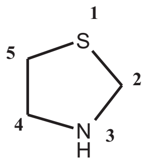

Thiazolidine
(1)

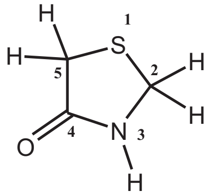

Thiazolidin-4-one
(2)

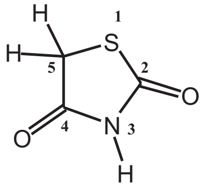

Thiazolidin-2,4-dione
(3)

Introduction of suitable substituents at the 3rd and 5th positions of thizolidine-2, 4-diones results in a variety of TZDs with diverse biological properties.

III. Synthetic methods for thiazolidine-2, 4-diones

Several methods have been reported in literature for the synthesis of 2, 4-thiazolidinediones.

(a) From thiourea

A two component condensation reaction between chloroacetic acid and thiourea provides a simplified route to TZDs. Gaonkar et al reported the synthesis of a series of N-substituted thiazolidine-2,4-dione derivatives bearing potentially bioactive substituents by microwave irradiation method.[2] The reaction process is either a two-step process (Scheme-1) which involves the formation of 2-imino-thiazolidin-4-one in the first step or a one pot condensation reaction (Scheme-2).[3] The resulting 2-imino-thiazolidin-4-one upon irradiation by 200 Watt microwave at 140°C for 10 min gives thiazolidine-2,4-dione.

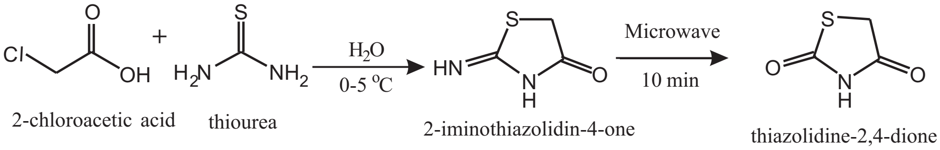

Scheme-1. Two-step process for synthesis of TZD from thiourea with microwave

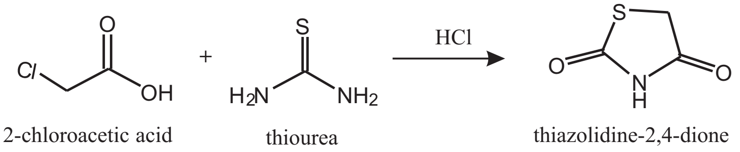

Scheme-2. One pot condensation reaction for synthesis of TZD from thiourea

Alam et al reported the synthesis of TZDs by the reaction of α-chloroacetic acid or chloroacetic ester with thiourea in an aqueous medium. The initially formed 2-imino-thiazolidin-4-one upon acid catalyzed hydrolysis produces 2,4-thiazolidinones (Scheme-3).[4]

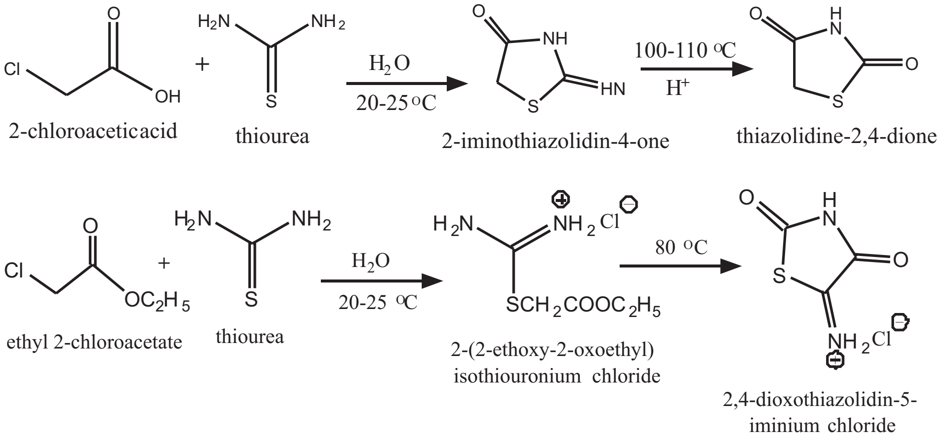

Scheme-3 Synthesis of TZDs from chloroacetic acid or chloroacetic ester with thiourea in an aqueous medium

(b) From alkyl thioncarbamates

The reaction between alkyl thioncarbamates (xanthogenamides) and α-Chloroethanoic acid is another approach for the synthesis of 2, 4-thiazolidinediones via formation of S-Carboxymethylthiocarbamate (Scheme-4).[5]

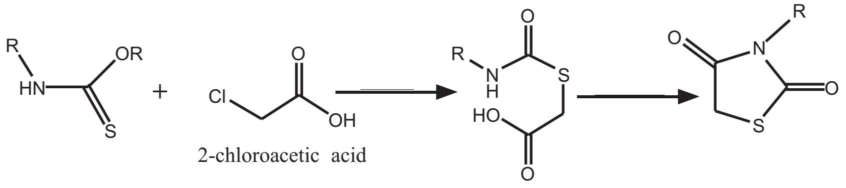

Scheme-4. Synthesis of TZD from alkyl thioncarbamates and Chloroethanoic acid

(c) From Isothiocynate

Isothiocyanate can be used in place of alkyl thioncarbamates for the synthesis of TZDs. The reaction of phenylisothiocyanate with benzilic acid, involves α- carbon atom of benzylic acid to produce an addition product (5) that cyclizes by acid to 3, 5, 5-triphenyl-2, 4-thiazolidinedione **(Scheme-5)**[6]

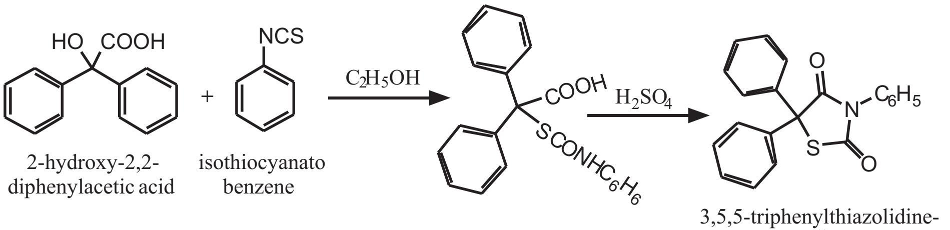

Scheme-5. Synthesis of TZD from isocyanates

(d) From alkali thiocyanates

2, 4-Thiazolidinedione have also been synthesized by treating the product of the reaction of ethyl chloroacetate and potassium or sodium thiocyanate with dilute HCl (Scheme-6).[7]

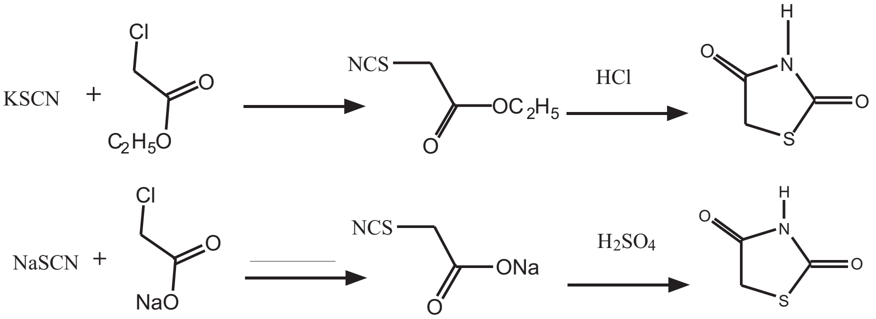

Scheme-6 Synthesis of TZD from alkali thiocyanates

This intermediate of this reaction is identical with that of reaction between chloroacetic acid and ethyl thiocarbamate or ammonium thiocarbamate.[8]

IV. Synthesis of 5-substituted thiazolidine-2, 4-diones

For the preparation of derivatives of TZDs, two ring positions are important, the 5th carbon which acts as an active methylene group and allows condensation reactions and the 3rd position, i.e., N-H which allows an easy replacement of the hydrogen with any other group.9 The synthesis of 5-substituted TZDs have been reported by the following methods.

(a) Knoevenagel condensation of aromatic aldehydes with TZDs

Zhang et al reported the synthesis of 5-arylidene-2, 4-thiazolidinediones by the Knoevenagel condensation of aromatic aldehydes with 2, 4-thiazolidinedione catalyzed by ethylenediamine diacetate (EDDA) under solvent-free conditions (Scheme-7).[10]

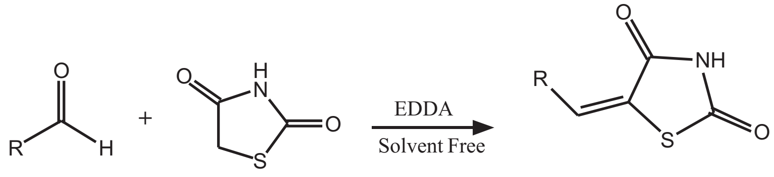

Scheme- 7. EDDA catalyzedsynthesis of 5-arylidene-2, 4-thiazolidinediones.

For the preparation of 5-arylidiene TZD, a mixture of 2, 4-thiazolidinedione, aldehyde, and EDDA were stirred at 80◦C in an oil bath for the appropriate time. After completion of reaction, the reaction mixture was cooled to room temperature, diluted with water and the separated product was filtered, washed and dried.

Ruhemann et al synthesized 5-arylidiene TZD by the Knoevenagel condensation of aromatic aldehydes with 2,4-thiazolidinedione catalyzed by piperidine using ethyl acetate or ethanol as solvent (Scheme-8)11or piperidinium acetate in toluene under reflux conditions.[12]

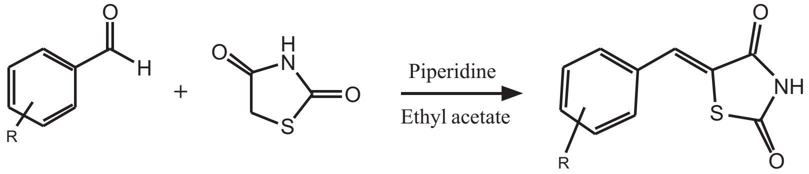

Scheme-8 Synthesized 5-arylidiene TZD by the Knoevenagel condensation

Thirupathi et al reported the green syntheses of substituted-5-arylidene-2, 4-thiazolidinediones using L-tyrosine as an eco-friendly catalyst in aqueous medium **(Scheme- 9)**.[13]

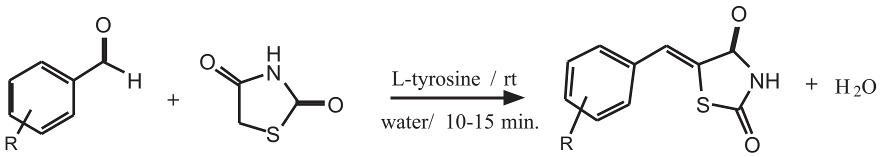

Scheme- 9 Green syntheses of substituted-5-arylidene-2, 4-thiazolidinediones using L-tyrosine

Sandhu et al reported synthesis of 5-arylidene TZDs with aldonitrones using polyethylene glycol as solvent **(Scheme-10)**.[14] The reaction proceeds via addition-elimination way and afforded the desired products in very good to excellent yield.

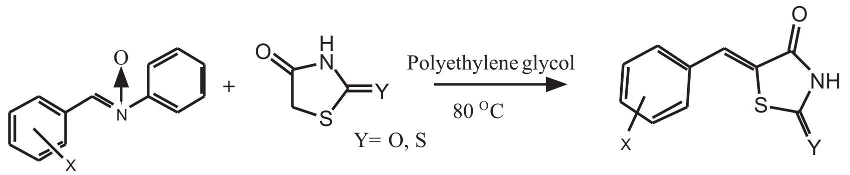

X= H, Cl, Br, NO_2, CH_3, CH_3O & OH

Scheme-10 Synthesis of 5-arylidene TZDs using aldonitrones in polyethylene glycol

In another report, Sandhu et al reported the synthesis of 5-arylidene TZDs by ZnO nanoparticles catalyzed Knoevenagel condensation of aldehydes and active methylene compounds with TZDs under solvent free reaction condition at 90oC **(Scheme-11)**.[15]

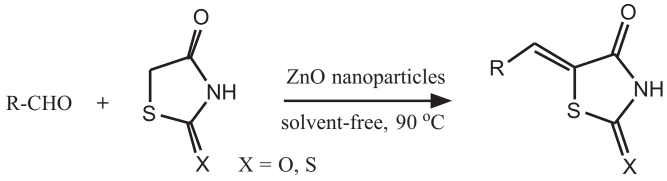

R = C_6H_6 , 4-MeO-C_6H_4 , 4-Cl-C_6H_4 , 2-furyl , 2-thiophene, 3-formylchromone

Scheme11 ZnO Nano-beltsas catalystin Knoevenagelcondensation

Ibrahim et al carried out Knoevenagel condensation of 3-formyl chromone with thiazolidine-2,4-dione in glacial acetic acid and freshly fused sodium acetate for the preparation of 5-arylidene TZD, 5-[4-oxo-4H-chromen-3-yl)methylene]-1,3-thiazolidine-2,4-dione **(Scheme-12)**.[16]

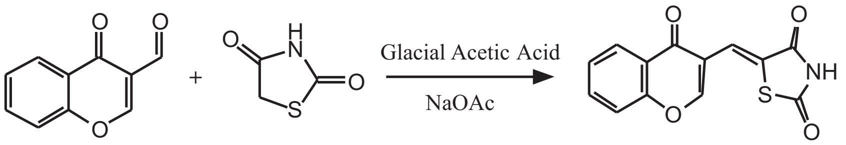

Scheme-12 Knoevenagelcondensationof 3-formylchromonewith thiazolidine-2,4-dione in glacialacetic acid

Khazaei et al reported synthesis of 5-arylidene-2, 4-thiazolidinediones by the Knoevenagel condensation of 2, 4-thiazolidinedione with aromatic aldehydes in the presence of tetrabutylammonium hydroxide/H_2O-EtOH **(Scheme-13)**.[17]

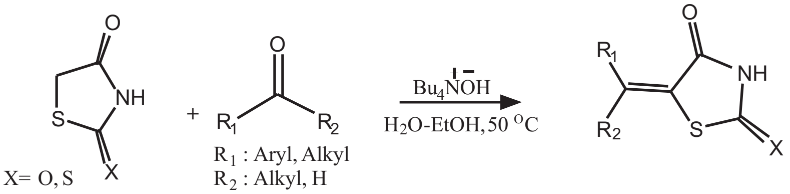

Scheme-13 Knoevenagel condensation of 2, 4-thiazolidinedione with aromatic aldehydes in the presence of tetrabutylammonium hydroxide

Shelkea et al reported an efficient synthesis of 5-arylidine 2,4-thiazolidinediones by the Knoevenagel condensation of aromatic aldehydes with 2,4-thiazolidinedione using 1-benzyl-3-methylimidazolium dihydrogen phosphate ([bnmim]H2PO4) acidic ionic liquid at 70°C **(Scheme-14)**.[18]

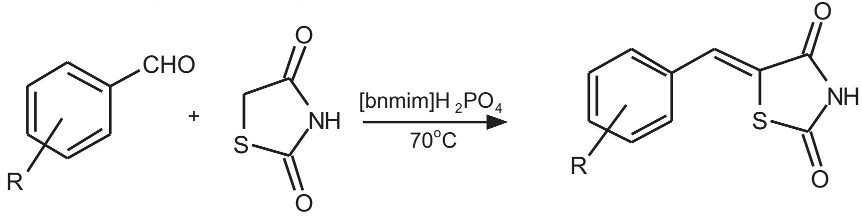

Scheme-14. Knoevenagel condensation of aromatic aldehydes with TZD using 1-benzyl-3-methylimidazolium dihydrogen phosphate

(i) Reaction with diazonium salt

5-Aryldiazo-2,4-thiazolidinediones are prepared by the coupling reaction of diazonium salts with 5-methylene group of 2,4-thiazolidinediones **(Scheme-15)**.[19]

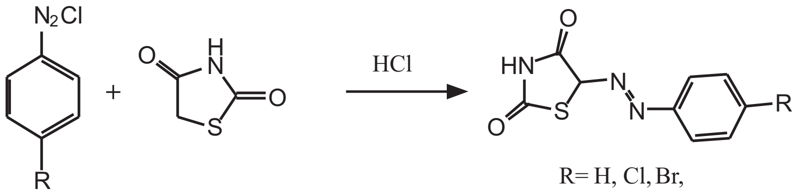

Scheme-15 Diazonium salts undergo a coupling reaction

(i)Reaction with diphenylformamidine

5-Anilinomethylene derivatives of 2,4-thiazolidinediones can be prepared by a reaction between diphenylformamidine and, 4-thiazolidinedione. The reaction involves electrophilic carbon atom of diphenylformamidine and nucleophilic methylene carbon atom of, 4-thiazolidinedione **(Scheme-16)**.[20]

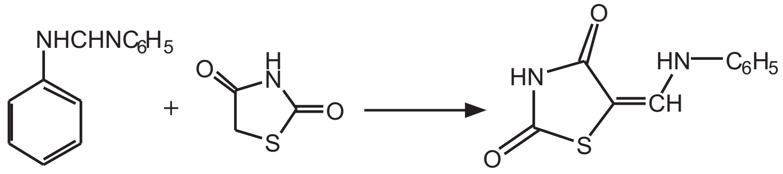

Scheme-16 Reaction with diphenylformamidine

V. Synthesis of 3,5-disubstituted thiazolidine-2, 4-diones

N-substituted 5-arylidinethiazolidine-2,4-diones have been prepared by the reaction of 5-arylidenethiazolidine-2,4-dione and α-halo-ketones. N-substituted-2,4-thiazolidinedione derivatives (TZDs) have also been prepared via N-alkylation of 2, 4-TZD at position 3 using substituted benzyl halides **(Scheme-17)**. [21]

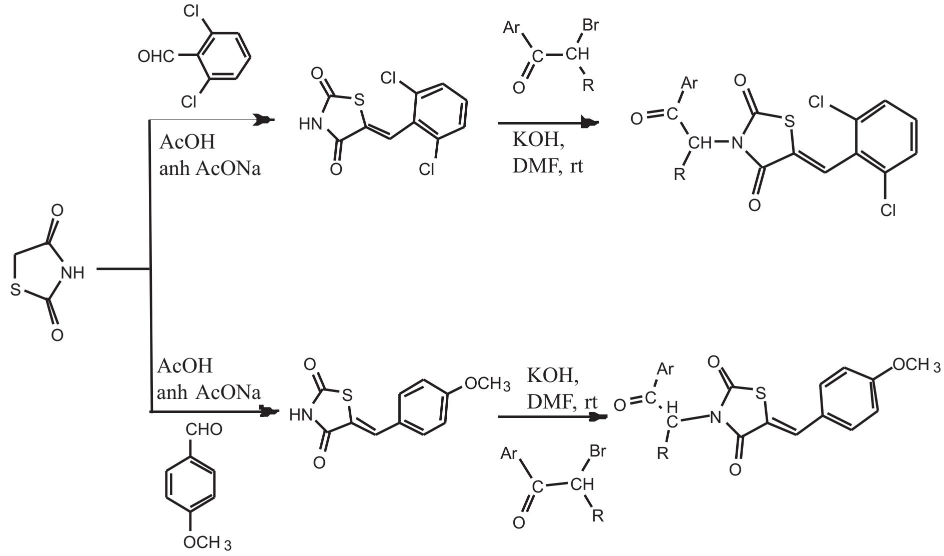

Scheme- 17 SynthesisofN-substituted5-arylidinethiazolidine-2,4-diones

VI. Biological activity of thiazolidine-2, 4-diones

Natural products containing thiazolidine ring are known to possess cytotoxic, anticancer, antiviral, and anti-inflammatory activities.[22] Latrunculin-A, micacocidin and hectochlorin are well known examples of natural products with anticancer activity.[23] Even the core structure of the first antibiotic drug penicillin is thiazolidine ring which is attached with β-lactam ring, and a side chain.

Thiazolidine-2, 4-diones (TZDs) are also known for their wide range of biological activities such as anti-inflammatory,[24] anti-tubercular,[25] anti-microbial,[26] cytotoxic[27] and anti-oxidant[28] activities. The structural variations of TZDs usually involve the relatively more reactive active methylene group at the 5th position, hence most often modifications at this position, exhibit a wide spectrum of pharmacological properties **(Figure-1)**.[29]

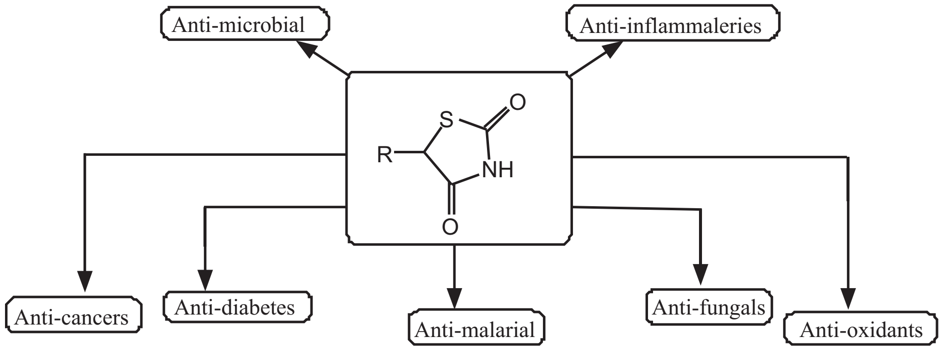

Fig.-1. Biological activity of 5-substituted TZDs

VII. Thiazolidinediones as Antidiabetics

Diabetes mellitus (DM), commonly referred to as diabetes, represents a group of metabolic diseases, leading to high blood sugar levels over a prolonged period. The number of people suffering from diabetics is quite alarming. According to the first WHO global report on diabetes, an estimated of 422 million adults were having diabetes in 2014 compared to 108 million in 1980 and in 2012 alone diabetes caused 1.5 million deaths and high blood glucose was the cause of another 2.2 million deaths.[30] Due to this concern, the theme for World Health Day 2016 was Diabetes.[31] Diabetes was first documented in Ebers Papyrus, which was written in 1552 BC. Physicians from India were discovered this disease at the same time and named as Madhumeha or Honey urine.[32]

Of the two types of diabetes, type 2 diabetes (formerly called non-insulin dependent or adult-onset) is more prevalent (> 90 %).[33] Type 1 diabetes previously known as Insulin dependent, juvenile or childhood-onset) is characterized by deficient insulin production and requires daily administration of insulin. Symptoms may occur suddenly like excessive excretion of urine (polyuria), thirst (polydipsia), constant hunger, weight loss, vision change and fatigue.[34] Type 2 diabetes (formerly called non-insulin dependent or adult-onset) result from the body's ineffective use of insulin.[35] Diabetic patients (> 90 %) suffer from type 2 diabetes. This dramatic rise is largely due to the rise in type 2 diabetes and factors driving it include overweight and obesity.

In the last few years thiazolidinediones (glitazones) have emerged as useful antidiabetic drugs.[36] They have been recognized as a class of insulin sensitizing drugs used in the treatment of type 2 diabetes mellitus (T2DM), which is one of the most predominant diabetes types.[37] They are believed to increase insulin sensitivity by activating the peroxisome proliferator-activated receptor γ (PPAR-γ), also known as the glitazone receptor.38 The first type of TZD drug was Troglitazone, which became available in 1997, but it was subsequently withdrawn from the market in 2000 because of hepatotoxicity. Rosiglitazone and pioglitazone are two TZDs which are currently available but with the side effects such as weight gain and hepatotoxicity.

In fact thiazolidinedione (TZD) nucleus is present in several widely used families of antidiabetic drugs such as Pioglitazone,[39] Rosiglitazone,[40] Troglitazone,[41] Ciglitazone, Darglitazone, Englitazone, Netoglitazone, Rivoglitazone, Balaglitazone and Lobeglitazone **(Figure-2).**

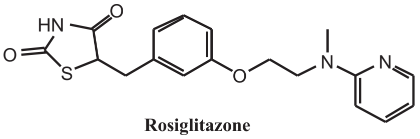

Rosiglitazone

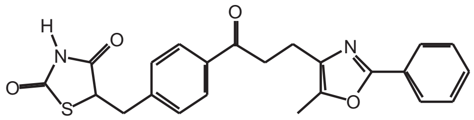

Darglitazone

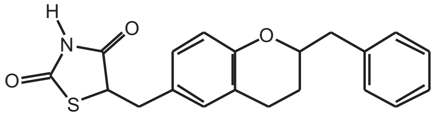

Englitazone

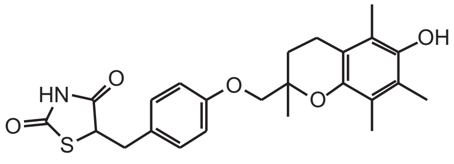

Troglitazone

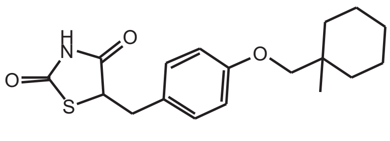

Ciglitazone

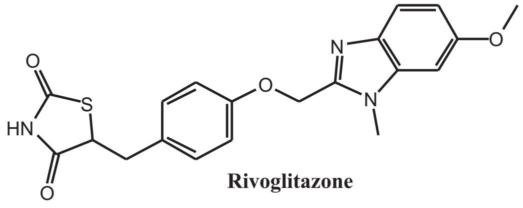

Rivoglitazone

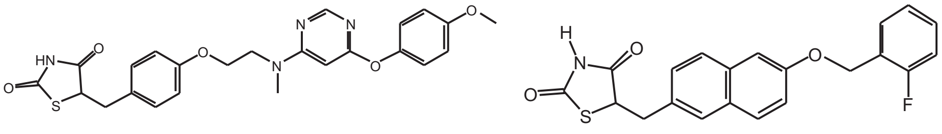

Lobeglitazone **Netoglitazone**

Fig. 2. Some Antidiabetic drugs

There are several reports on the synthesis and evaluation of thiazolidine-2,4-diones as antidiabetic agents.[42] Ramrao et al reported synthesis and biological activity of (Z)-5-[4-(2-chloroquinolin-3-yl)methoxy]benzylidinethiazolidine-2,4-dione derivatives (4) as antidiabetic agents.[43] Shashikant et al described studies on the synthesis and biological activity of 5-(4-(pyridin-1(2H)-ylsulfonyl) benzylidene)thiazolidine-2,4-dione (5) as antidiabetic agent.[44]

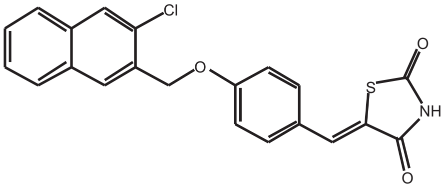

(4)

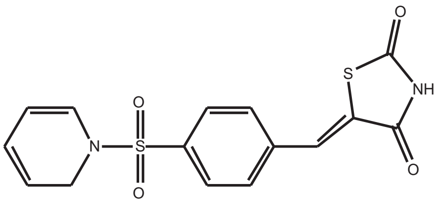

(5)

Thus a wide range of substituted 2,4-thiazolidinediones have been developed as more effective and selective antidiabetic agents, which act by increasing the sensitivity towards insulin and are termed as "insulin sensitizers". Thiazolidinediones activate the peroxisome proliferator-activated receptor (PPARγ) by binding with it, the receptor then migrates to the DNA activating transcription of a number of specific genes ultimately improving the sensitivity of target tissue in insulin and reduces the plasma glucose level in type 2 diabetes patients.[45] A study revealed that in the series of approx. 11 derivatives, naphthalene group is superior to other groups for stimulating anti-hyperglycemic activity. The attachment of 5- sulfonyl -2, 4-thiazolidinedione as [CH2SO2 and SO] moiety to the 2-naphthalene position led to optimum activity. But attachment of other groups like thio, methylene, oxy and sulfonyl between naphthalene and thiazolidinedione rings were found to decrease anti-hyperglycemic activity.[46]

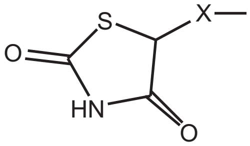

R = 2-naphthyl, 4-Bromophenyl, 4-fluorophenyl
X = O, CH_2, CH_2S, CH_2SO_2, SO, SO_2, S

A series of thiazolidine-2, 4-diones have been synthesized by replacing the ether function of Englitazone (Fig-2) with different functional groups for example ketone, alcohol or olefin moiety[46]. All the compounds were evaluatedfor lowering of blood glucose levels in genetically obese and insulin resistant mouse.

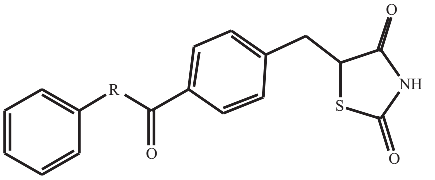

R = CH_2 , OCH_2 , CH=CH

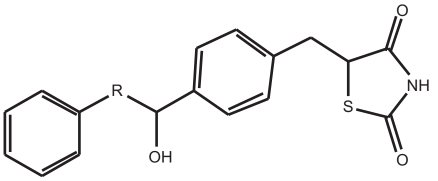

VIII. Conclusion.

Thiazolidine-2,4-dione is an extensively explored heterocyclic nucleus for its role in the development of a wide variety of antidiabetic, anti-inflammatory, anti-tubercular, anti-microbial, cytotoxic and anti-oxidant agents. Various 5-substituted thiazolidine-2,4-diones have been found to be more effective and selective antidiabetic agents, by acting as insulin sensitizers. They are believed to increase insulin sensitivity by activating the peroxisome proliferator-activated receptor γ (PPAR-γ). Thiazolidine-2,4-dione ring system can be conveniently assembled from simple starting materials, and additionally can be suitably substituted with a variety of substituents by employing simple synthetic procedures.

IX. References

1. Rizos CV, Kei A and ElisafMS.ArchToxicol., 2016, 90(8):1861-81.
2. Gaonkar S L, Namratha B, Shetty N S and Shimizu H.Interactive Medicinal Chemistry 2014. doi: 10.7243/2053-7107-2-2.
3. Prashantha, B.R.; Adhikary, L. J. Heterocyclic Chem. 2006, 43, 897.
4. Alam F, Biplab K D and Pallab K. Indian Journal of Pharmaceutical Science & Research Vol. 5 Issue 2, 2015, 67- 71.

5. Allen CF and Vnallan, J A. Organic Synthesis John Wiley and Sons, Inc. New York. III, 1955, 751.
6. Taylor J; J. Chem. Soc.2000, 117, 4.
7. Heintz W; Annulennes1995, 136, 223.
8. Ruhemann S; J. Chem. Soc.1999, 95, 117.
9. Anna P G, Nikalje G, Dipali D and Hemant D. U; European Journal of Experimental Biology, 2012, 2 (2):343-353.
10. Zhang Y and Zhou Z; Organic Chemistry International Volume 2012, Article ID 194784, 5 pages.
11. Xia Z,Knaak C, Ma J, Zanna M B, Campbell M, Wang W, Andrew S. K and Charles D. S; J. Med. Chem., 2009, 52 (1), pp 7486. 11 (a) L. V. Sonawane, S. B. Bari.International Journal of Biological Chemistry, 2011, 5, 1, 6874.
12. Cantello B C C, Cawthorne M A andCottam G P;Journal of Medicinal Chemistry, vol. 37, no. 23, pp. 39773985, 1994.
13. Thirupathi G, Venkatanarayana M, Dubey P K and BharathiKumari Y; Der Pharma Chemica, 2012, 4(5):2009-2013.
14. Kumar D, Narwal S, and Sandhu J S; International Journal of Medicinal Chemistry, Volume 2013 (2013), Article ID 273534.
15. Suresh and Sandhu J S;International Journal of Organic Chemistry, 2012, 2, 305-310.
16. Ibrahim M A, Abdel Hamed M A M and El-Gohary N M;Journal of the Brazilian Chemical Society,2011, 22,6,11301139.
17. Malik N and Prasad D N; Iranian Journal of Pharmaceutical Sciences, 2012: 8(3): 209-214.
18. Shelkea K F, Idholeb S S, Badara A D and Devhadea J B;Der Pharmacia Lettre, 2016, 8 (5):72-75
19. Dains F B and Stephenson A E;J. Am. Chem. Soc. 1996. 38, 1841.
20. ArdeshirK, HojatV, SafaeiM and Ahmadian H; Journal of Sulfur chemistry, 35, 2014, vol 3.
21. Swapna D, Sivagami B, Manasa K, Rajita G and Alagarsamy V; Int. Res. J.Pharm., 2016, 7, 15-19.
22. Nazreen S, Alam MS, HamidH,Yar M S, Dhulap A, Alam P, Pasha M A Q, Bano S, Alam M M, Haider S, Kharbanda C, Ali Y and Pillai K K;Bioorg. Med. Chem. Lett.,2014, 24, 3034-3042.

23. Konishi H, Anticancer Research; June 2009 vol. 29 no. 6 2091-2097.
24. Barros CD, Amato AA, Oliveira TB, Iannini KBR, Silva AL, Silva TG, Leite ES, HernandesMZ,Lima MCA, Galdino SL, Neves FAR and Pitta IR ;Bioorg.Med. Chem., 2010, 18; 3805-3811.
25. Pattan SR, Alagwadi KR, Bhat AR, Reddy VVK, Pattan JS, Khade AB and Bhatt KG;Indian Drugs.2008, 45; 532-535.
26. Oya B,Ozen O, Arzu M, Engin K, Rahmiye E;Bioorg. Med. Chem., 15 (2007) 6012-6017.
27. Shankar GA andKallanagouda RA;Med. Chem. Res., 2012, 21; 816-824.
28. Swath N, Ramu Y, Subrahmanyam CVS and Satyanarayana K;Int. J. Pharm. Sci., 2012, 4; 561-566.
29. Rawal RK, Tripthi RK, Katti SB,Pannecouque C and De Clercq E;Med Chem., 2007, 3; 355363.
30. Global report on diabetes, World Health Organization, Geneva, 2016.
31. World Health Organization- Diabetes country profile, 2016.
32. A Biographical History of Endocrinology, D. Lynn Loriaux, Published Online: 12 Feb 2016.
33. Reaven G M, Diabetes, 37, 1988, 1595-1607.
34. Aboraia, A.; Rahman, H.M.A.; Mahfuz, N.; Mohmoud, A. and Gendy, EL;Bioorg. Med. Chem. Lett.2006, 14, 1246.
35. Diagnosis and Classification of diabetes mellitus. WHO , Geneva, 1999 report number WHO/NCD/NCS/99.2
36. Dadasaheb K and Jain N; Innovational Journal of Chemistry 1, 2016, 50-62.
37. Napoleon A; International Journal of Pharm Tech Research, 2016, 9(3), 429-443.
38. Issemann I and Green S;Nature. 1990, 347, 645650.
39. Cantello, B C C.; Cawthome, M A.; Haig D.; HindleyR.M and Smith S.A; Thurlby P L;Bioorg. Med. Chem. Lett. 1994, 4, 1181
40. Cantello B C C.; Cawthome M A.; Cottam, G.P.; Duff, P.T.; Haig, D.; Hindley, R.M; Lister, C.A. and Smith, S.A and Thurlby, P L; J. Med. Chem.1994, 37, 3977.
41. Cossy J and Menciu C; Bioorganic & Medicinal Chemistry Letters 9, 1999, 3439-3440.

42. (a) Imran M, Ilyas B, Deepanjali & Khan A; Recent Thiazolinediones as antidiabetics; J of Scientific and Industrial Research, 2007, 66, 99-109. (b) Dadasaheb1, K & Jain N, Thiazolidinediones as antidiabetic agents-A Review, Innovational Journal of Chemistry 1 (2016) 50-62. (c) Fathima F & and Lakshmanan B; Thiazolidinediones as a privileged structural scaffold in PPAR agonists: A review; International Journal of Pharmaceutical Chemistry, (2016) 06 (05). (d) Molavi B, Rassouli N, Bagwe S & Rasouli N; A review of thiazolidinediones and metformin in the treatment of type 2 diabetes with focus on cardiovascular complications; Vascular Health and Risk Management 2007:3(6). (e) Suchitra M, Mounica R.V.S & Murali M.; Synthesis, characterization and biological evaluation of some novel Thiazolidinedione derivatives; International Journal of Pharmacometrics and Integrated Biosciences; 2017, 2, 158-164

43. Mane R, Dhanaji V and Umesh R;Bulletin of Korean Chemical Society. 2011, 32, 2171-2176.

44. Pattana S, Kekareb P, Patil A andNikalje A;Iranian Journal of pharmaceutical Sciences. 2009, 5, 225-230.

45. Berger J and Moller D;Annual Revolution of Medicines. 2009, 53, 409435.

46. Lee H.W, Ahn J.B, Kang S.K, Ahn S.K and Ha D.C; Org. Process Res. Dev.2007; 11(2): 190199.

47. Hulin, B.; Clark, D.A. and Goldstein S W;J. Med. Chem.1992, 35, 1853-1864.

Curr. Rep. Sci. & Tech. 3 (2017) 91-107

PEG-400 mediated growth of nanostructured CuO thin/thick films and their gas sensing performance

Iqbal Singh, Gursharan kaur, Taminder Singh, Kamalpreet Khun Khun, Rajan Saini
Department of Physics, Khalsa College Amritsar-143001
iqbalsgh@yahoo.com

Abstract

CuO material presents several applications and in this work it has been synthesized by employing two different routes to compare its properties in thick and thin film based samples. Sol-gel auto-combustion is used as first route in which Poly ethylene glycol (PEG-400) assisted CuO powder has been prepared which assembled on glass substrate using an organic binder to form thick film. In the second route, an aqueous solution of cupric nitrate with PEG-400 is ultrasonically sprayed onto glass substrates at different substrate temperature to deposit CuO thin films.The effect of calcination temperature and molecular weight of PEG on particle size of CuO can be determined. The X-ray diffraction study shows the formation of CuO as dominant phase in both type of samples. Surfactant addition in precursors results in the decrement of crystallite size in powder sample whereas size increases in spray deposited thin film samples. The scanning electron microscope images reveal dispersing nature of surfactant, that helps to improve porosity in the material. The uniform size distribution of CuO particles in powder sample is depicted by transmission electron micrographs. The SEM images of thin film depict an increase in specific surface area with the addition of PEG. The activation energy of thin film samples is found to be comparatively higher than in thick film.

Keywords: adsorption, film deposition, CuO

I. Introduction

The chemical route using surfactants to synthesize metal oxide nanoparticles has attracted considerable attention in last decade. There are various fields where these materials find important applications such as catalyst [1], window material [2], photosensor [3] and gas sensor [4, 5]. CuO being a p-type semiconductor material with a band gap of 1.25-1.51 eV having wide range of applications which makes it promising material in research. This material in the form of nanoribbons [5], nanowires [6, 7], mesoporous dandelion structure [8], urchin-sheet like structure [9], hollow microsphere [10] and nanoneedles [11] etc. has attracted considerable attention due to utilization in diverse technological areas. In the form of a film, it is mainly used in devices like solar cell [12], window material for solar cell [2], photosensor [7], catalytic sensor [13] and gas sensor [14].

Variety of synthesis techniques like chemical [15], polymer precursor [16], and hydrothermal [17] etc. have been used widely for the preparation of nanocrystalline CuO powder. However, despite the excellent progress in afore mentioned techniques, there is one or more drawbacks associated in their procedure. As no sophisticated instrument is required in chemical precipitation and solgel methods and simple processing route, so these methodologies draw considerable attention [18, 19]. Solgel auto combustion route is an interesting and powerful way for producing singlephase ceramics at relatively low temperature with compositional homogeneity, huge porosity and purity [20-22]. The gel combustion process has been extensively employed in the last few years for the synthesis materials, such as SnO_2, NiO, yttria stabilized zirconia and ferrites.

High quality CuO films have been deposited by various techniques such as thermal evaporation [23], thermal oxidation [24], spray pyrolysis [25, 26], sol-gel dip coating [27, 28] and sputtering [29] etc. Among these the spray pyrolysis is preferred over the others routes due to several advantages such as cost effective, easily controllable parameters and most importantly no vacuum is required [25, 26, 30-33].

Surfactant molecules are widely used for controlling size, shape of grains and acts as polymer which plays an important role in synthesizing self assembled nano as well as micro structures. The surfactant molecules absorb on specific crystal planes and initiate an anisotropic grain growth. PEG as non ionic surfactant has been widely used in fabricating nanostructured materials by different routes in interesting morphologies with improved properties [34-41]. In its molecules the hydrophilic oxygen atoms are easily linked with the free hydroxyl ions on the surface of colloid particles by hydrogen bonds. The properties of material can be tailored by selecting different types of PEG series. Han [41] have successfully deposited hexagonal ferrites using PEG 2000 by adopting self propagating combustion technique. Liu [40] have deposit PEG assisted grown ZnO thin films by dip coating method. However as far as the data available, PEG has been widely used in the synthesis of various materials in the powder form but there is no report available related to the deposition of PEG assisted CuO films by using ultrasonic spray pyrolysis technique.

In this paper, the PEG assisted CuO powder and thin films have been synthesized by sol gel auto combustion and ultrasonic spray pyrolysis techniques respectively. The samples are systematically characterized and obtained results have been investigated to study the effect of non-ionic surfactant on CuO based thick and thin films.

II. Experimental

a) Material

All the chemicals (Loba Chemie Mumbai) of analytical reagent grade are used as precursors. The solutions are prepared in doubly distilled water. Corning 7059 borosilicate glass slides (2x4 cm2) are used as substrates and cleaned by standard procedure prior to use.

b) Synthesis process

Sol-gel auto-combustion

Trihydrated cupric nitrate ($Cu(NO_3)_2{\cdot}3H_2O$) and monohydrated citric acid ($C_6H_8O_7{\cdot}H_2O$) are used as starting materials. To prepare 100 mL of precursor solution, with metal nitrate to citric acid (MN:CA) molar ratio of 1:1, required amount of cupric nitrate and citric acid dissolved in water. The pH of the solution is adjusted to 7 using microprocessor based (Naina make NIG 334) pH meter. 10 mL of 0.5 M PEG-400 solution is added drop wise to previously formed citrate complex. The solution is thermally dehydrated in an oven at temperature of 80 ± 5 ˚C to form viscous liquid followed by decomposition on preheated hot plate. The detailed combustion mechanism has been reported earlier [43, 44].

Ultrasonic spray pyrolysis technique

The precursor solution for aerosol generation is prepared by dissolving the required amount of $Cu(NO_3)_2{\cdot}3H_2O$ in water to form 0.2 M, 100 mL solution. To it 10 mL of 0.5 M PEG-400 solution is added drop wise with vigorous stirring. The preparative parameters of the ultrasonic spray setup such as nozzle to substrate distance, solution concentration, solution spray rate etc., are optimized to obtain, pin hole free, adherent films and are kept constant in all experiments. The substrate temperature is varied from 300 to 400˚C, in steps of 50˚C using electronic temperature controller (Model DTC303, Selec make) with accuracy of ± 3 ˚C. The substrates are heated to required temperature by a specially designed electrical heater, and the temperature is measured using K type (chromel□alumel) thermocouple. The distance between the nozzle and the substrate after optimization is maintained at 25 cm. The spray rate is fixed at 1 mL per minute. The aerosol is generated using ultrasonic nebulizer (Omron NE-U17), and subsequently passed through glass nozzle using air as carrier gas onto preheated glass substrate. The detailed procedure of film deposition has been already discussed in detail previously [45, 46]. The powder samples and spray deposited films are named as per terminology indicated in Table 1

Table 1 : Codes for the PEG doped CuO powder/thin films

Material powder/film	Calcination/Substrate temperature	Code
CuO powder without PEG-400	400 ± 2 °C	P1
CuO powder with PEG-400	400 ± 2 °C	P2
CuO thin film (without PEG)	300 ± 3 °C	F1
CuO thin film (0.5M PEG-400)	300 ± 3 °C	F2
CuO thin film (0.5M PEG-400)	350 ± 3 °C	F3

c) Thick film fabrication

A known quantity of calcined PEG assisted CuO powder is thoroughly grounded in an agate pestle mortar to ensure uniform fine powder. The fine powder is converted into thixotropic paste by mixing it with an organic solvent diethnolamine. The ratio of inorganic to organic part is kept equal to 75:25 in all cases. The fluidity of paste depends upon extent of organic part, which goes in its formulation. This particular ratio for paste formation is found to be thixotropic in nature and gives good adhesion to substrate. A uniform layer of the thixotropic paste is then deposited on ultrasonically cleaned glass slides. The films are subjected to spining on a spin coater (Macmillan) under 4000 rpm for five minutes to allow the uniform distribution of the paste. The drying of films is carried out at 400 ˚C in the muffle furnace for 1 hour to burn out the organic binder. The reproducibility in the thickness of the films is possible by maintaining proper rheology and thixotropy of the paste.

d) Structural analysis

The phase identification of the powder and thin film samples is analyzed by X-ray diffraction (XRD) pattern, taken using X'Pert Panlytical diffractometer with Cu Kα radiation (λ = 1.5405 Å , 30 mA , 40 kV) in 2θ range from 30-80˚.

Texture coefficient

Texture coefficient for the thin films is calculated using the equation given as [47, 48]

$$T(hkl) = \frac{I(hkl)}{I_o(hkl)} \; \frac{1}{n} \; {}^{n}_{i=1} \; \frac{I(hkl)}{I_o(hkl)} \; {}^{-1} \tag{1}$$

where I_0 represents the standard intensity, I is the observed intensity of the *(hkl)* plane and n is the reflection number.

Grain size

The average crystallite size (*D*) is obtained from the most prominent peak using Scherrer's formula [49]

$$D = \frac{0.9}{\cos} \tag{2}$$

where β is the FWHM of the powder, θ the Bragg angle, λ the wavelength of X-ray used.

Lattice constants

Lattice parameters ($a \neq b \neq c, \alpha = \gamma = 90^\circ \neq \beta$ for monoclinic structure) and the volume of unit cell for the CuO powder samples and films are calculated using the formulas given below.

$$\frac{1}{d^2} = \frac{1}{\sin^2} \; \frac{h^2}{a^2} + \frac{k^2 \sin^2}{b^2} + \frac{l^2}{c^2} - \frac{2hl\cos}{ac} \tag{3}$$

$$V = abc\sin \tag{4}$$

e) Surface morphology and compositional study

To study the surface topography and compositional analysis of powder and films, field emission scanning electron micrographs (FESEM), energy-dispersive absorption X-ray spectroscopy (EDAX) spectrum respectively are taken on a JEOL JSM-6700F with a beam voltage of 20 kV.

Table 2.
Values of the texture coefficient T(hkl), lattice constant, a (Å), b (Å), c (Å), β (Degree), cell volume (Å3), crystallite size (D) from XRD, particle size from FESEM, and elemental composition from EDAX of P1, P2, F1 and F3 samples

Property/ Sample code	**P1**	**P2**	**F1**	**F3**
T(*hkl*), (002):(111)	-	-	2.072:1.928	2.191:1.809
a (Å)	4.682	4.684	4.699	4.669
b (Å)	3.424	3.427	3.427	3.420
c (Å)	5.114	5.117	5.121	5.090
β (Degree)	99.111	99.306	99.639	97.709
cell volume (Å^3)	80.949	81.087	81.088	81.062
average Crystallite size (nm) XRD	63	51	38	43
SEM (average particle size, nm)	850	100	400	160
EDAX (At %) Cu:O	70.32:29.68	65.69:34.31	42.22:57.78	28.82:71.18

f) Electrical characterization

The activation energy conduction is calculated from the temperature-conductivity measurements using the formula

$$= {}_0 \exp(-\frac{\Delta E_a}{kT}) \tag{5}$$

where ΔE_a is the activation energy which corresponds to the energy difference between the valance band and the conduction band, σ_o is a temperature independent factor and k is the Boltzmann's constant and T is the absolute temperature.

III. Results and discussion

a) Structural properties

XRD diffractogram of P1 and P2 samples are found to be polycrystalline in nature and all prominent reflections can be indexed to monoclinic CuO phase which are in good agreement with those reported by International Center for Diffraction Data (ICDD) card 41-254 of CuO. It has been found that PEG addition slightly decreases diffraction peak intensity of prominent peaks corresponding to (002) and (111) atomic planes of CuO. Interestingly, no other peak corresponding to any of the source material, Cu and Cu_2O is noticed.

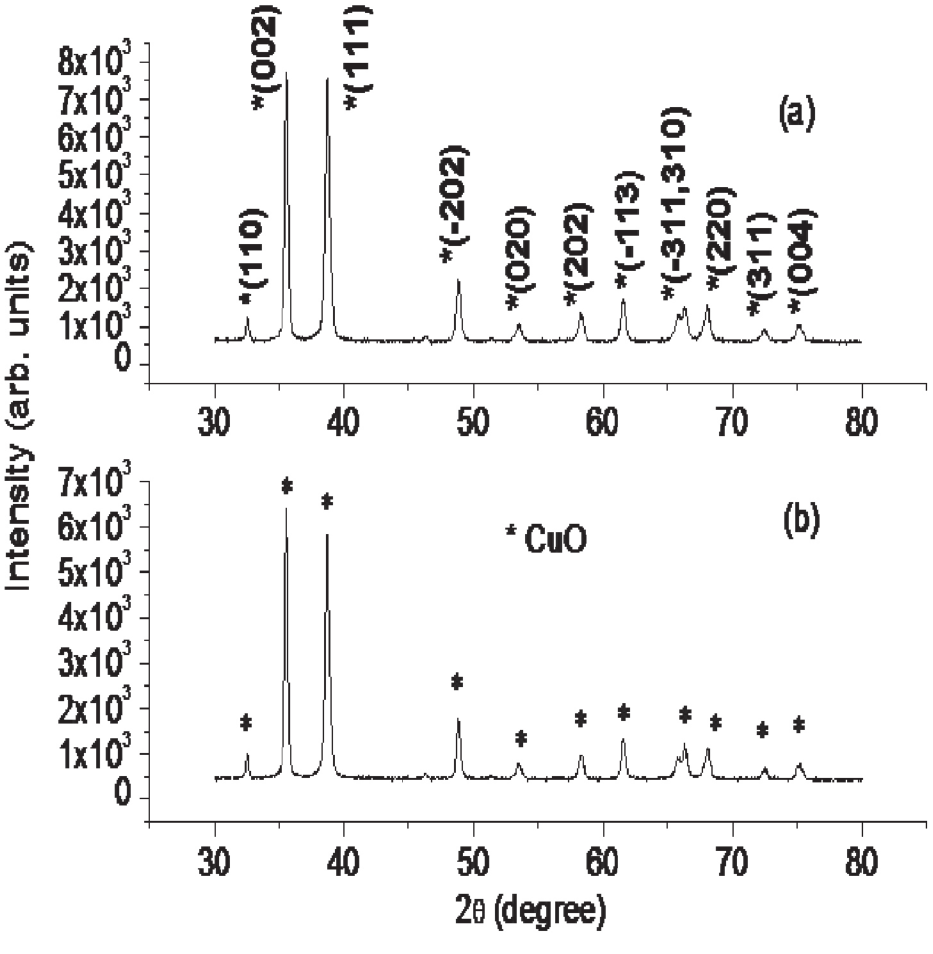

Fig 1 XRD pattern of the CuO powder calcined at 400 °C (a) P1 and (b) P2

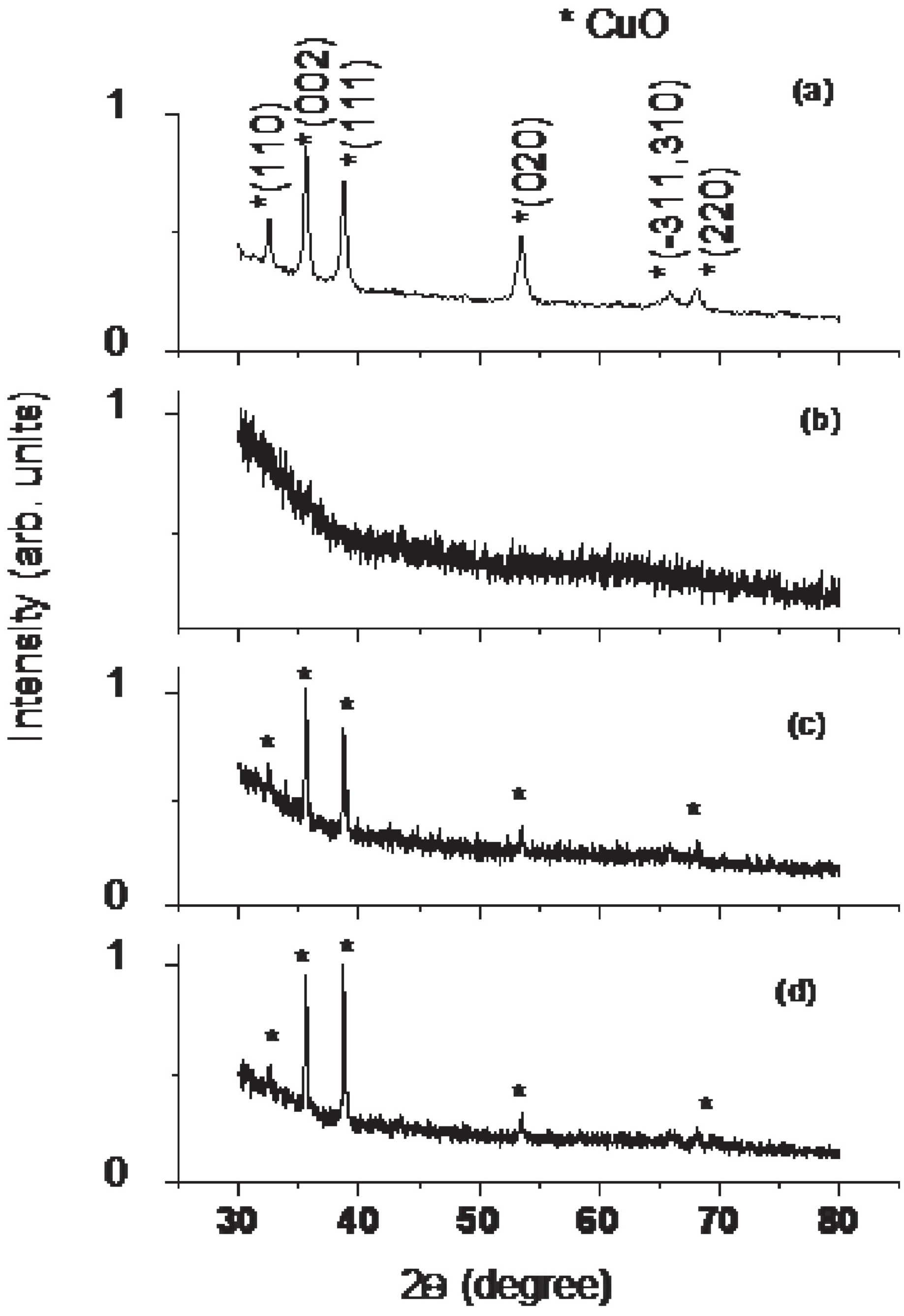

Fig. 1 *XRD pattern of the spray pyrolysis deposited CuO thin films*
(a) F1, (b) F2, (c) F3 and F4

XRD diffractograms of USP deposited films shown in Fig. 2 indicates the film deposited at substrate temperature of 300°C is found to be amorphous whereas rise in substrate temperature to 350 and 400 °C shows characteristic CuO peaks. The strong and sharp diffraction peaks corresponding to CuO phase of (002) and (111) atomic planes appeared at 2θ value of 35.5° and 38.7° respectively. No peak corresponding to Cu_2O phase has been noticed in the diffraction patterns. It has been noticed that addition of PEG strongly affects the crystallinity of CuO films. It has been observed in the XRD analysis that addition of PEG reduces or eliminates the lower intensity peaks corresponding to the atomic planes (110), (020) and (220) of CuO phase as evident in Fig 1(b) and Fig 2(c, d). Findings from this work suggested that the crystalline CuO films with PEG are successfully deposited at substrate temperature of 350°C. Further characterization of films results for the F1 and F3 films are calculated and co-related.

The values of texture coefficient for the F1 and F3 are recorded in Table 2. Its value greater than one for the peak located at 35.5° and 38.7° reveals the preferential orientation of the film. Texture coefficient value for the (002) plane is significantly higher in comparison to (111) plane. This result reveals that CuO particles are anisotropic in shape (non-spherical) [51] and deposited grains tend to possess facet like morphology as directed by the templating nature of surfactant. Zhang [39] have observed the similar effect of PEG doping on the indium doped tin oxide thin films..

Using Scherrer's formula, average crystallite size of samples has been calculated (Table 2) and found to be 51 nm in P2 sample whereas in case of thin film F3 sample it is 43 nm. The lattice parameters of samples (P1, P2, F1 and F3) have been calculated (Table 2) and found to be in good agreement with ICDD data card 41-254. The variation in values of lattice parameters and unit cell volume of samples indicates the evidence of strain. The values of lattice parameters for the samples have been found to be lower in magnitude as compared to one those reported for bulk CuO in literature. This implies that lattice structure in sol gel auto combustion derived and spray pyrolysis deposited CuO films having more number of defects. The amount of defects has been found to be enhanced with PEG addition in precursors which improves the electrical properties of the material.

b) Surface properties

FESEM images as shown in Fig. 3 depict the surface morphology of CuO powder samples and show highly agglomerated particles in P1 sample in comparison to P2

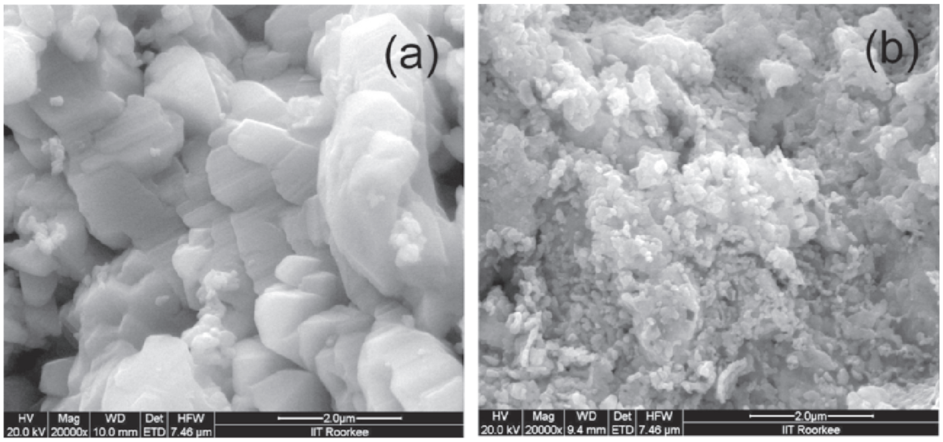

Fig. 3 The FESEM of CuO powder samples (a) P1 and (b) P2 on 2 µm scale

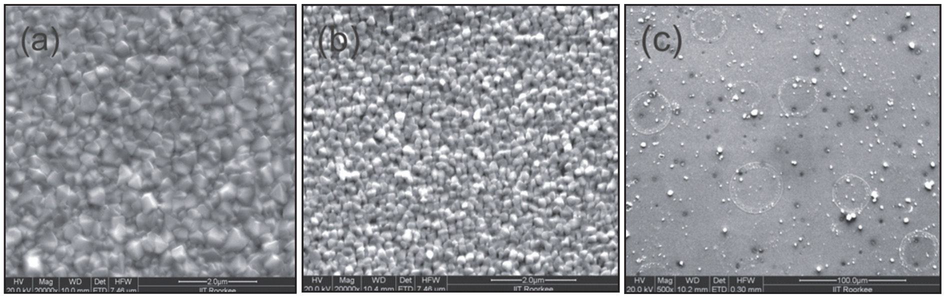

Fig. 4 The FESEM of CuO thin film (a) F1, (b) F3 on 2 µm and (c) F3 on 100 µm scale

Sample thus justifying the templating nature of the PEG. Fig 4 shows FESEM images of spray deposited F1 and F3 films which exhibit uniform, compact, crack free and nano-sized particle agglomerates. Randomly distributed trapezium shaped grains of size 400 nm have been observed in F1 film sample. F3 film sample shows comparatively smooth morphology and possesses more number of pore channels and possess an interesting morphology on the 100 µm scale, in which spherically shaped particles aggregated to form coin like structures. A numbers of coins appeared on different locations film on the micrograph. The transformation of facets like morphology of particles to spherical might be due to templating nature of the non-ionic, polymer type PEG surfactant used in the synthesis of several porous materials [41]. PEG assisted powder and spray deposited CuO samples shows relatively higher specific surface area, which promises its potential applications.

PEG-400 is a non ionic surfactant and able to acts as a dispersing agent in the reaction. It is one of the most flexible water soluble polymer which has hydrophilic and hydrophobic radicals on the long carbon chains. In aqueous medium its flexible ether linkage makes it less sterically hindered and causing more oxygen atom on polymer chain to combine with the metal ion. Feng [52] have also observed the similar effect and reported the detailed mechanism of the PEG assisted hydrothermal growth of ZnO. The dispersing nature of the surfactant keep the sol particles separated due to long chain of molecules. The surfactant addition causes a reduction in surface tension and slows down growth rate of sol particles. Zhang [35] have discussed same concept of the PEG-2000 molecules on the synthesis of ZnO particles by using zinc nitrate and citric acid. Salarian [53] observed the similar effect of PEG-600

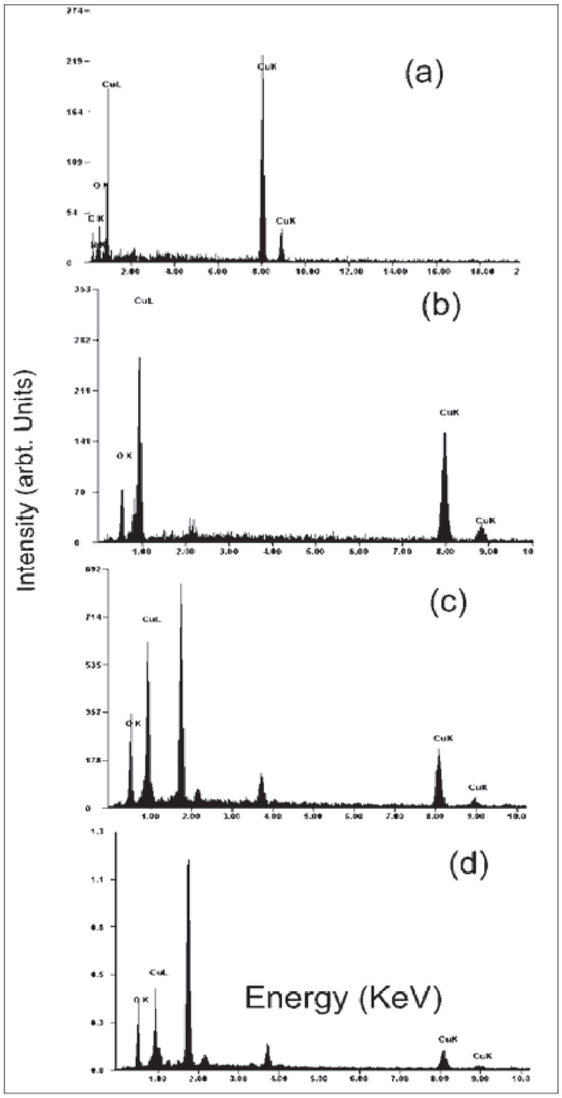

Fig. 5 The EDAX spectrum of CuO samples (a) P1, (b) P2, (c) F1 and (d) F3

along with cetylytrimethy-lammonium bromide (CTAB) in the hydrothermal synthesis of hydroxyapatite.

The elemental composition of P1, P2, F1 and F3 samples has been estimated from EDAX spectrum (Fig. 5) and obtained values are recorded in Table 2. CuO powder samples are found to be oxygen deficient whereas F1 and F3 samples are metal deficient.

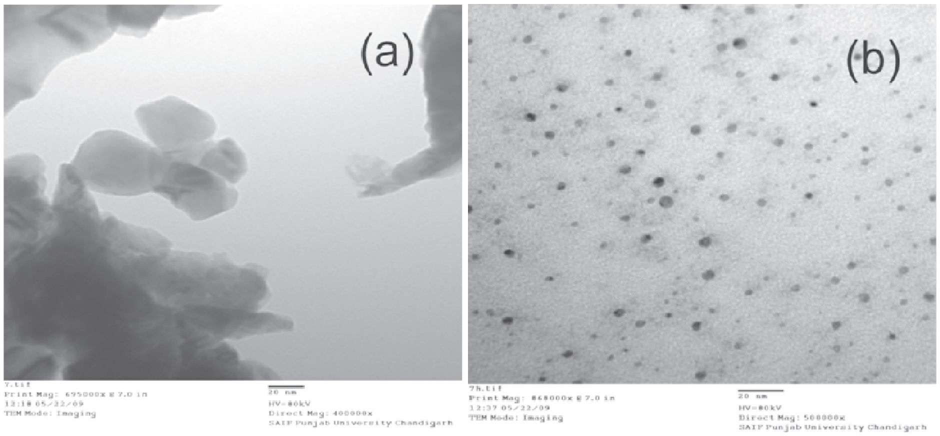

Fig. 6 The TEM images of CuO powder samples (a) P1 and (b) P2 on 20 nm scale

TEM images of P1 and P2 as shown in Fig. 6 depicts the porous, loosely agglomerated and spherical shaped particles. The crystallite size distribution without PEG is found to be broader, whereas its addition

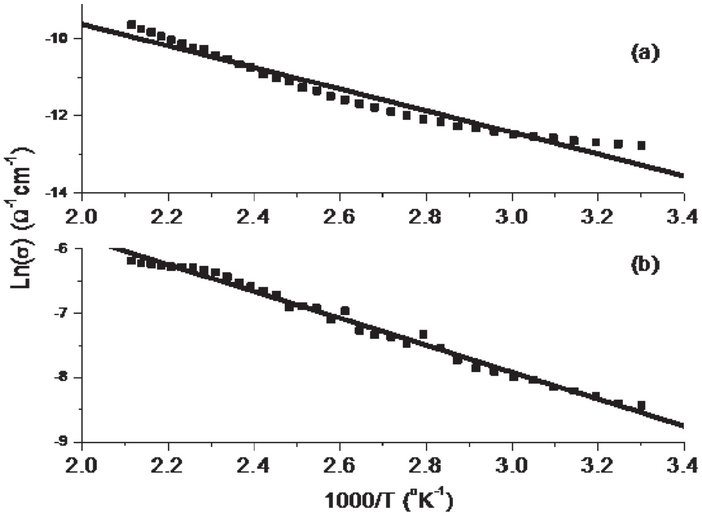

Fig.7 The variation of conductivity with temperature for CuO samples (a) P1, (b) F3

reduces it to a narrow range of 5-8 nm. The formation of spherically shaped CuO crystallite for the P2 samples may be attributed to the formation of micelles in the gel. Hasab [54] discussed the control of micelles on the growth of crystallites as well as agglomeration.

c) Electrical properties

Fig. 7 reports Arrhenious equation plot of P2 and F3 films. The conductivity has been found to increases with temperature indicating, the semiconducting behaviour of the films and suggesting a thermally activated conduction mechanism. From slope of plots, the activation energy of conduction for samples has been calculated and corresponding values are recorded in Table 3. The increase of activation energy in case of P2 and F3 samples can be understood from the increase in large number of grain boundaries. It is expected that increase of defects as suggested by the XRD analysis of the PEG doped samples consequently increases the scattering of charge carrier. The grain boundary and carrier scattering processes at the defect site thus decreases the film conductivity.

IV. Conclusions

Nanocrystalline PEG-400 doped CuO powder based thick and spray deposited thin films are synthesized by using sol-gel auto combustion and ultrasonic spray pyrolysis techniques. The average crystallite size has been found to be 51 and 43 nm in corresponding powder and thin film samples. The lower value of the lattice constants as compared to standard data indicates that the CuO nanocrystallites are subjected to considerable defects in the powder and thin film. Nearly spherically shaped grains are found in PEG doped CuO powder sample. The facets like grains were uniformly distributed on the entire surface of substrate in case of thin film. The activation energy is higher in PEG doped samples which might be due to increased grain boundary scattering with surfactant addition.

V. Acknowledgements

Authors wish to thank UGC for providing financial support in the form of Minor research project, Director IIT Roorkee, STIC, Kochi and RSIC, Panjab University, Chandigarh for providing FESEM, EDAX and XRD facilities. We also gratefully acknowledge Mr. Gurpreet Singh, for his kind assistance in the electrical characterization of the samples.

VI. References

[1] S. M. El-Sheikh, F. A. Harraz, K. S. Abdel-Halim, J. Alloys Compds. 487(1-2) (2009) 716-723

[2] M. Abdel Rafea, N. Roushdy, J. Appl. Phys. D 42 (2009) 015413

[3] Q. Kaung, C. S. Lao, Z. Li, Y. Z. Liu, Z. X. Xie, L. S. Zheng, Z. L. Wong, J. Phys. Chem. C 112 (2008) 11539-11544

[4] J. Zhang, J. Liu, Q. Peng, X. Wang, Y. Li, Chem. Mater. 18 (2006) 867-871

[5] X. Gou, G. Wang, J. Yang, J. Park, D. Wexler, J. Mater. Chem. 18 (2008) 965-969

[6] N. D. Hoa, N. V. Quy, M. A. Taun, N. V. Hieu, Physica E 42(2) (2009) 146-149

[7] J. H. Benjamin, L. Ganhua, C. Junhong, J. Nanomater. (2008) 830474 91-7

[8] S. Manna, K. Das, S. K. De, Appl. Mater. Interface 2(5) (2010) 1536-1543

[9] M. Vaseem, A. Umar, S. H. Kim, A. Al-Hajry, Y. B. Hahn, Mater. Lett. 62 (2008) 1659-1662

[10] S. Wang, H. Xu, L. Qian, X. Jia, J. Wang, Y. Liu, W. Tang, J. Solid State Chem. 182 (2009) 1088-1093

[11] Y. Liu, L. Liao, J. Li, C. Pan, J. Phys. Chem. 111 (2007) 5050-5056

[12] L. Wang, K. Han, G. Song, X. Yang, M. Tao, IEEE (2006) 1-4244-0016-3/06

[13] F. Teng, W. Yao, Y. Zheng, Y. Ma, Y. Teng, T. Xu, S. Liang, Y. Zhu, Sens. Actuat. B 134 (2008) 761-768

[14] Y. Li, J. Liang, Z. Tao, J. Chen, Mater. Research Bull. 43 (2008) 2380-2385

[15] D. Li, Y. H. Leung, A. B. Djurisic, Z. T. Liu, M. H. Xie, J. Gao, W. K. Chan, J. Cryst. Growth 282 (2005) 105-111

[16] A. I. Fernandez, A. Calleja, J. M. Chimenos, M. A. Fernandez, X. G. Capdevila, M. Serarra, H. Xuriguera, F. Espiell, J. Sol-Gel Sci. Techn. 36 (2005)11-17

[17] Y. Zhang, S. Wang, Y. Qian, Z. Zhang, Solid State Sci. 8 (2006) 462-466

[18] L. C. Pathak, T. B. Singh, S. Das, A. K. Verma, P. Ramachandrarao, Mater. Lett. 57(2) (2002)380-385

[19] J. Zhou, Y. Wang, F. Zhao, Y. Wang, Y. Zhang, L. Yang, J. Lumin. 119 (2006) 248-252

[20] M. G. Hasab, S. A. S. Ebrahimi, A. Badiei, J. Mag. Mag. Mater. 316 (2007) e13-e15.

[21] V. A. Hiremath, A. Venkataraman, Bull. Mater. Sci. 26 (2003)391-396

[22] S. Kikkawa, J. Am. Ceram. Soc. 88 (2) (2005) 308-311

[23] G. Papadimitropoulos, N. Vourdas, V. E.Vamvaskas, D. Dava Zoglov, Thin Solid Films 515 (2006) 2428-2432

[24] A. H. Jayatissa, K. Guo, A. C. Jayasuriya, Appl. Surf. Sci. 255 (20090 9474-9476

[25] J. Morales, L. Sanchez, F. Martin, J. R. Ramos-Barrado, M. Sanchenz, Electrochemica Acta, 49 (2004) 4589-4597

[26] S. Kose, F. Atay, V. Bilgin, I. Akyuz, Mater. Chem. Phys. 111 (2008) 351-358.

[27] S. C. Ray, Solar Energy Mater. Solar Cells 68 (2001) 307-312

[28] L. Armelao, D. Barreca, M. Bertapelle, G. Bottaro, C. Sada, E. Tondello Thin Solid Films 442 (2003) 48-52

[29] K. H. Yon, W. J. Choi, D. H. Kang, Thin Solid Films 372 (2000) 25-256

[30] J. H. Lee, B. W. Yeo, B. O. Park, Thin Solid Films 457 (2004) 333-337

[31] C. Luyo, I. Fabregas, L. Reyes, J. L. Solis, J. Rodriguez, W. Estrada, R. J. Candal, Thin Solid Films 516 (2007) 25-33

[32] V. R. Shinde, S. B. Mahadik, T. P. Gujar, C. D. Lokhande, Appl. Surf. Sci. 252 (2006) 7487-7492

[33] R. K. Kawar, P. S. Chigare, P. S. Patil, Appl. Surf. Sci. 206 (2003) 90-101

[34] X. L. Gou, F. Y. Cheng, Y. H. Shi, L. Zhang, S. J. Peng, J. Chen, P. W. Shen, J. Am. Chem. Soc. 128 (2006) 7222-7229

[35] Y. L. Zhang, Y. Yang, J. H. Zhao, R. Q. Tan, P. Cui, W. J. Song, J. Sol-Gel Sci. Techno. 51 (2009) 198-203

[36] M. Salarian, M. Solati-Hashjin, S. S. Shafiei, R. Salarian, Z. A. Nemati, Ceram. Int. 35 (2009) 2563-2569

[37] N. Arconada, A. Duran, S. Suarez, R. Portela, J. M. Coronado, B. Sanchez, B. Sanchez, Y. Castro, Appl. Catalyst B: Environmental 86(1-2) (2008) 1-7

[38] C. Santato, M. Odziemkowski, M. Ulmann, J. Augustynski, J. Am. Chem. Soc. 123 (2001) 10639-10649

[39] J. Zhang, K. H. Au, S. Y. Chang, J. Ceram. Process. Res. 5(3) (2004) 208-213

[40] Z. Liu, J. Li, J. Ya, Y. Xin, Z. Jin, Mater. Lett. 62(8-9) (2008) 1190-1193

[41] M. Han, Y. Ou, W. Chen, L. Deng, J. Alloy Compds. 474 (2009) 185-189

[42] R. K. Bedi, I. Singh, Curr. Nanosci. 5(3) (2009) 273-277

[43] C. S. Barrett, T. B. Massalski, Structure of Metals, Pergamon, Oxford, 1980. pp. 204

[44] V. Bilgin, S. Kose, F. Atay, I. Akyuz, J. Mater. Sci. 40 (2005) 1909-1915

[45] G. K. Williamson, W.H. Hall, Acta Mater. 1 (1953) 22-31

[46] V.M. Nikale, N.S. Gaikwad, K.Y. Rajpure, C.H. Bhosale, J. Mater. Chem. Phys. 78 (2003) 363-366

[47] S. Navaladian, B. Viswanathan, T. K. Varadarajan, R. P. Viswanath, Nanoscale Res. Lett. 4 (2009) 181186

[48] R. K. Bedi, I. Singh, Appl. Mater. Interfaces 2(5) (2010) 1361-1368

[49] Y. Feng, M. Zhang, M. Guo, X. Wang, Cryst. Growth Des. 10(4) (2010) 1500-1507

[50] M. Salarian, M. Solati-Hashjin, S. S. Shafiei, R. Salarain, Z. A. Nemati, Ceram. Inter. 35 (2009) 2563-2569

[51] M. G. Hasab, S. A. Seyyed Ebrahimi, A. Badiei, J. Eur. Ceram. Soc. 27 (2007) 3637-3640

[52] I. Singh, R. K. Bedi, J. Mater. Sci. 46 (2011) 5568-5580

[53] I. M. Richard, Principles of Adsorption and Reaction on solid surfaces, Wiley-Interscience, New York, (1996) pp. 519

[54] R. Tongpool, S. Yoriya, Thin Solid Films 477 (2005) 148-152

[55] K. Khun Khun, A. Mahajan, R. K. Bedi, Chem. Phys. Lett. 492 (2010) 119-122

[56] A. T. Alexey, P. H. Gregory, T. M. Brent, W. A. John Sens. Actuat. B, 93 (2003)126-134

[57] J. H. Bejamin, K. Nikolai, L. Ganhua, L. I-Kuan, C. Junhong, Z. Zin, J. Phys. Chem. C. 114 (2010) 2440-2447

[58] M. S. Wagh, G. H. Jain, D. R. Patil, S. A. Patil, L. A. Patil, Sens. Actuat. B 115 (2006) 128-133

[59] D. R. Patil, L. A. Patil, P. P. Patil, Sens. Actuat. B, 126 (2007) 368-374

[60] H. Tang, M. Yan, H. Zhang, S. Li, X. Ma, M. Wang, D. Yang, Sens. Actuat. B 114 (2006) 910-915

[61] D. N. Suryawanshi, D. R. Patil, L. A. Patil, Sens. Actuat., 134 (2008) 579-584

[62] B. Karunagaran, P. Uthirakumar, S. J. Chug, S. Velumani, E. K. Suh, Mater. Charac. 58 (2007) 680-684

[63] R. B. Kamble, V. L. Mathe, Sens. Actuat. B, 131 (2008) 205-209

[64] N. G. Deshpande, Y. G. Gudage, R. Sharma, J. C. Vyas, J. B. Kim, Y. P. Lee, Sens. Actuat. B, 138 (2009) 76-84

[65] N. V. Hieu, L. T. B. Thuy, N. D. Chien, Sens. Actuat. B 129 (2008) 888-898

[66] V. Srivastava, K. Jain, Sens. Actuat. B 133 (2008) 46-52

[67] Y. M. Zhao, Y. Q. Zhu, Sens. Actuat. B 137 (2009) 27-31

[68] T. Sjciliano, M. Di Giulio, M. Tepore, E. Tepore, E. Filippo, G. Micocci, A. Tepore, Sens. Actuat. B 138 (2009) 550-555

[69] G. N. Chaudhari, S. V. Jagtap, N. N. Gedam, M. J. Pawar, V. S. Sangawar, Talanta 78 (2009) 1136-1140

Curr. Rep. Sci. & Tech. 3 (2017) 108-112 © Khalsa College Amritsar

Metal Phthalocyanines Based Photovoltaic Devices

*Manjit Kaur**[a], *Rajesh Kumar*[b], *Rakesh Dogra*[c], *Narinder Arora*[d]
[a]*Department of Applied Sciences, IK Punjab Technical University, Kapurthala - 144603, India,*
[b]*P.G. Department of Physics, D.A.V. College, Amritsar-143001, India,*
[c]*Department of Applied Sciences, B.C.E.T. Gurdaspur-143521, India*
sainimanjeet.kaur0@gmail.com

Abstract:

Semiconductors play an important role in present day to day life. They are broadly classified into two main classes as inorganic and organic semiconductors. The present electronic industry is based on inorganic semiconductors like germanium and silicon; but in the near future they are expected to be replaced by organic semiconductors. Metal phthalocyanines (MPc) belongs to a group of small molecules with Q-band absorption in the red to near-IR range and they have high chemical stability, optical, light stability and photovoltaic properties. Among all the organic materials, copper phthalocyanine is a semiconductor material with high thermal and chemical stability for thin film fabrication. CuPc is the mostly used organic semiconductor for fabrication of optical and electronic devices like, light emitting diodes, field effect transistors, solar cells and gas sensors. Zinc phthalocyanine (ZnPc) is also an important organic semiconductor for photovoltaic applications. The major part of the incident light in the visible region is absorbed and effectively contributes to photo carrier generation and the excited carriers play an important role in thin film preparation. Metal phthalocyanines (copper and zinc phthalocyanine) have been found to have applications for fabrication of devices like photovoltaic, sensors, light emitting diode etc.

Keywords: organic semiconductors, photovoltaic, sensors, light emitting diodes.

I. Introduction

Organic semiconductors play an important role in present day to day life. They have attracted so much attention because they are light weight, flexible and not fragile; so they are suitable for transportation and portable electronic applications [1,13] .The organic materials have some important advantages over the inorganic materials such as low cost, easy processing, flexibility and low density. Polymers, low molecular weight organic materials, fullerene, carbon nanotubes etc are the examples of organic materials [2]. In the past, organic materials were considered as insulators. In the last few decades the discovery of conducting organic materials has attracted the researchers and scientists to use these materials in optoelectronic devices [3].

Using organic materials as the active layer has a number of advantages and disadvantages. Organic materials are easy to process into large area thin films at a comparatively low cost due to their structure being generally self-organized polycrystalline. However, this polycrystalline nature results in low energy conversion efficiency compared to inorganic solar cells [4]. Inorganic cells made from materials such as silicon are expensive to produce as they have highly crystalline structures which result in high efficiency. Despite substantial progress in solar cell architecture, design and rational choice of the donor-acceptor materials over the past two decades, organic PVs are still unable to overcome the 6-7% barrier of conversion efficiency. In terms of the low conversion efficiency, there are currently at least four major fundamental aspects making organic PVs vulnerable for commercial applications as compared with conventional semi conducting solar cells i.e. low carrier mobility, lack of absorption in the red/NIR part of the spectrum, poor environmental stability and excitonic character of photo carrier generation [5].

Even inorganic semiconductors have capability to perform as a sensor but the organic semiconductors because of their special properties related to physical and electrical parameters have a potential to be used as a sensing materials. Related to electrical parameter, the change in electrical properties of organic materials in response to external agents like temperature, humidity, light, pressure, displacement, gases, electromagnetic radiations etc make the organic materials better as compare to inorganic materials. Also their physical properties such as high absorption coefficient, light weight, greater flexibility and larger surface area make organic materials better than inorganic semiconductors for device applications [6].

Among all the organic materials, copper phthalocyanine is a semiconductor material with high thermal and chemical stability for thin film fabrication [7]. Copper phthalocyanine belongs to a class of metal-organic compounds having a metal atom surrounded by aromatic rings in centre of molecule [8].

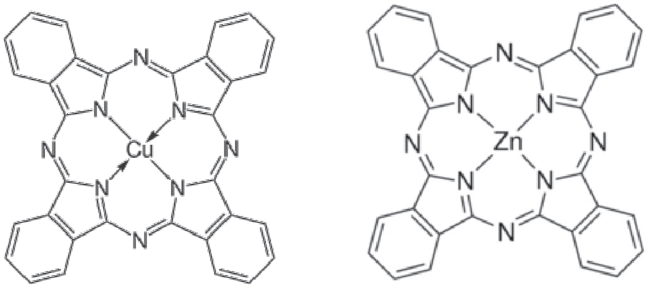

Copper Phthalocynine **Zinc Phthalocyanine**

Fig. 1

CuPc is the mostly used organic semiconductor for fabrication of optical and electronic devices like, light emitting diodes, field effect transistors, solar cells and gas sensors. Mechanism of sensor bases on the changes in electrical conductivity of thin phthalocyanine films induced by the presence of small gaseous molecules. Phthalocyanines materials are used in sensors because of their stability and durability. Also, their sensing properties are determined by the electronic properties of their space charge layers and the sensors made from phthalocyanine materials are capable of working efficiently under unfavourable environment [9].

Zinc phthalocyanine (ZnPc) is also an important organic semiconductor for photovoltaic applications. The major part of the incident light in the visible region is absorbed and effectively contributes to photo carrier generation and the excited carriers play an important role in organic photovoltaic cell [10].

MPc's have been used in P-N junction for applications in photovoltaic cells, resulting good conversion efficiency. Centrally placed metallic atoms in phthalocyanine ring leads to wide range of absorption and emission of these materials ranging in-between UV-Visible Near IR spectrum [11,14].

A. Principle of Organic Photovoltaic Cell:

Five steps to convert solar energy into electrical energy by organic solar cells are-

a) Absorption of light energy & generation of free electron - hole pair, b) Diffusion of free electron -hole pair to an active medium, c) Charge separation, d) Charge transport and e) Charge collection.

To fabricate a working solar cell, two photoactive materials are coupled between two electrodes (one is metallic & other transparent), so that photo generated charges are collected at the two ends of these electrodes. As a result, charge separation process occurs and charge carriers have to be transported to these electrodes without recombination and charges are collected at transparent interface [12].

II. Conclusion

Metal phthalocyanine (copper and zinc phthalocyanine) has been found to have applications for fabrication of devices structures like photovoltaic cells, sensors, light emitting diode etc. Organic photo voltaic materials are light weight, flexible, so they are suitable for transportation and portable electronic applications. Metal phthalocyanine based thin films have been widely used in organic semiconducting devices due to their ease of fabrication, electron conjugated bonding and absorption band lying between ultraviolet to visible region.

III. References

[1] M.C. Scharber, N.S. Sariciftci, Efficiency of bulk-heterojunction organic solar cells. Progress in polymer science (2013), 38(12), 1929-1940.

[2] K. Karimov, I. Qazi, S.A Moiz, I .Murtaza, Electrical properties of organic semiconductor copper phthalocyanine thin films deposited from solution at high gravity. Optoelectronics and advanced materials-Rapid communications (2008), 2(4), 219-223.

[3] A. Tomkeviciene, J.V. Grazulevicius, Glass-forming organic semiconductors for optoelectronics. Materials Science (2011), 17(4), 335-342.

[4] M Wright, A. Uddin, and Organicinorganic hybrid solar cells: A comparative review. Solar energy materials and solar cells (2012), 107, 87-111.

[5] A. M. Bagher, Comparison of organic solar cells and inorganic solar cells. International journal of renewable and sustainable energy (2014), 3(3), 53-58.

[6] Y. S. Zhao, H. Fu, A. Peng, Y. Ma, D. Xiao, J. Yao, Low dimensional nanomaterials based on small organic molecules: preparation and optoelectronic properties. Advanced Materials, (2008), 20(15), 2859-2876.

[7] S. M. Khan, M. Kaur, J.R. Heflin, M.H. Sayyad, Fabrication and characterization of ZnTPP: PCBM bulk heterojunction (BHJ) solar cells. Journal of Physics and Chemistry of Solids, (2011), 72(12), 1430-1435.

[8] M. Kraus, S. Richler, A. Opitz, W. Brütting, S. Haas,T. Hasegawa, F. Schreiber . High-mobility copper-phthalocyanine field-effect transistors with tetratetracontane passivation layer and organic metal contacts. Journal of Applied Physics (2010), 107(9), 094503.

[9] Y. Zhang, W.Hu. Field-effect transistor chemical sensors of single 1 nanoribbon of copper phthalocyanine. Science in China Series B: Chemistry (2009), 52(6), 751-754.

[10] K. Rajesh, V. Kannan, M.R Kim, Y.S. Chae, J.K. Rhee, High mobility polymer gated organic field effect transistor using zinc phthalocyanine. Bull. Material science, (2014), 37(1), 95-99.

[11] A. M. Saleh, S.M. Hraibat, R.M. Kitaneh, M.M. Abu-Samreh, S.M. Musameh, Dielectric response and electric properties of organic semiconducting phthalocyanine thin films. Journal of Semiconductors, (2012) 33(8), 082002.

[12] G. Chamberlain, "Organic solar cells: A review," Sol. Cells, (1983), (8), 4783.

[13] A. Chowdhury, B. Biswas,, M. Majuumder, M. Sanyal, B. Mallik, Studies on phase transformation and molecular orientation in nanostructure znpc thin films. Thin solid films (2012), 520, 6695-6704.

[14] A. Zanfolim, D. Volpati, C. Olivati, A., Constantino, Structural and electrical optical properties of Zinc phthalocyanine Evaporated Thin Films- Temperature and Thickness Effects, J.Phys.Chem (2010), 114, 12290-12299.

Curr. Rep. Sci. & Tech. 3 (2017) 113-120 © Khalsa College Amritsar

Self-assembled zinc phthalocyanine based nanostructures for gas sensing application

Pooja Devi[a]*, Rajan Saini*[b]*, Kamalpreet Khun Khun*[b]*, Iqbal Singh*[b]*,*
Gursharan Kaur[b]*, Taminder Singh*[b]*, Rajinder Singh*[c] *and R.K. Bedi*[c]
[a]*Department of Applied Physics, Giani Zail Singh Campus College of Engineering & Technology, Bathinda*
[b]*Post Graduate Department of Physics, Khalsa College Amritsar-143005*
[c]*Materials Science Research Laboratory, Department of Physics, Guru Nanak Dev University, Amritsar-143005*
pujaiitr09@gmail.com

Abstract

Zinc phthalocyanine based nanowires have been grown onto glass substrate using solution processing technique under different experimental conditions. The results revealed that the density and dimensions of nanostructures to be strongly dependent on the concentration of solution. It has been demonstrated that these nanowires were highly sensitive and selective towards Cl_2 with minimum detection limit as low as 5 ppb. The response of nanowires sensor was found to increase linearly (80-600%) with increase in Cl_2 concentration (5-500 ppb). Raman spectroscopic and XPS studies revealed that central zinc ions of were the predominant sites of Cl_2 absorption. Our results emphasized that these nanowires can be promising candidates for room temperature Cl_2 sensing applications.

Keywords: Phthalocyanine, gas sensors, self-assembly, nanowires.

I. Introduction

One dimensional nanostructures with high surface to volume ratio possess high sensitivity and faster sensing action as compared to bulk and thin films. Therefore, research on one dimensional nanostructures based gas sensors has been increased in the last few years. In this field, metal oxides and inorganic materials based nanostructures have already shown their potential for the detection of various harmful gases. While nanostructures of inorganic materials and metal oxides have been the center of attraction for many years, organic nanostructures have also emerged as a promising category with several advantages over their inorganic counterparts, such as unlimited choices of molecular structures for property optimization, low cost of material's fabrication, high flexibility, ease for large area processing and compatibility with flexible and light-weight plastic substrates [1]. Among organic materials, phthalocyanines are well established room temperature gas sensors but sometime we encounter their slower sensing characteristics so we need to fabricate their one dimensional nanostructures possessing high sensitivity and faster sensing characteristics [2]. Due to the poor solubility of unsubstituted phthalocyanines in organic solvents, their nanostructures have been fabricated by organic molecular beam epitaxy (OMBE), organic physical vapour deposition (OPVD), electrochemical method and vacuum evaporation technique with a limitation of higher cost of fabrication. Whereas substituted phthalocyanine are soluble in organic solvents so their conventional as well as hierarchical nanostructures have been fabricated by solution processing based techniques. Although these techniques are much simpler and cost effective than physical deposition techniques yet some of them have a few limitations. For example, recently nanowires, nanotubes and nanoflowers of substituted phthalocyanines have been fabricated by anodic aluminium oxide (AAO) template assisted method. But this method has a limitation of harshening the nanostructures while removing the template. Similarly 2,9,16,23-tetranitrophthalocyanine iron (TNFePc) based nanoflowers and zinc phthalocyanine (ZnPc) based hierarchical nanostructures have been grown by solvo-thermal method with a disadvantage of heat treatment at high temperature for several hours [3]. However, self-assembly technique is the simplest way to grow long range nanostructures for large area coverage [4]. Chlorine (Cl_2) is a toxic gas (OEL=0.5 ppm) which is widely used in various industries related with plastics, textiles, agrochemicals, pharmaceuticals, water purification and household cleaning products etc. It has several harmful effects on human body like skin irritation, suffocation, sensory irritation, bronchospasm etc. [5]. Because of increasing concern over the safety and health hazards related with this gas, there is an increasing demand of Cl_2 sensors. Keeping these reports into consideration, we have fabricated zinc phthalocyanine based nanowires by using low cost self-assembly technique and demonstrated their application as room temperature ppb level Cl_2 sensor.

II. Experimental

Substituted zinc phthalocyanine powder has been procured from Sigma Aldrich Pvt. Ltd. Glass substrates were washed with lab detergent solution and deionized water in order to remove dust particles. After this, substrates were ultrasonically and chemically cleaned with acetone, methanol and ultrapure water. The substrates were dried and kept in desiccator for further use. We have dissolved substituted zinc phthalocyanine powder into toluene. The concentration of this solution was approximately 10^{-3} M. The samples were prepared by depositing a droplet of the solution on the substrates in a closed environment. To study the surface morphology of the films, SEM images were taken by using Carl Zeiss Supra 55 scanning electron microscope with beam voltage 10 kV. Before SEM investigations, 20 nm thin gold layer was sputtered onto the film surface by using the Hind High Vacuum SEM Sputter Coater Model: 6SPT in order to avoid charge accumulation on the surface of film specimen. Film structure was examined by Bragg-Brentano (θ-2θ) scan of Bruker X-ray diffractometer (operated at 30mA and 40 kV) with CuK_α radiation (λ = 1.5418 Å) in the range 3º 40º. To study the gas sensing properties of films, sensor was fabricated by depositing two gold pads (50 nm thick, dimensions 5mm x 5mm with separation of 1 mm) onto the film sample by using a shadow mask. The sensor was then placed in a home built gas sensing chamber (1000ml) containing sample holder geometry and silver wires were connected to the gold electrodes by using silver paste. The dc conductance of the sensor was measured by applying a constant bias of 5 V. Cl_2 , NO_2, NO and NH_3 gases were commercially procured from M/s Chemtron Science Pvt. Ltd., India in the gas filled canister of volume 0.5 liters with a concentration of 1080ppm. A desired concentration of Cl_2 in the gas sensing chamber was achieved by injecting a known quantity of the gas using a micro-syringe. Air was used as carrying gas. Once a steady state was achieved after exposure, sensor conductance was recovered by opening the lid of the chamber. The sensor conductance was recorded continuously during both dosing and purging cycles as a function of time by using computer interfaced Keithley electrometer 6517A. The gas response of sensor was calculated by using the equation:

$$R(\%) = \left(\frac{C_g - C_a}{C_a}\right) \times 100\ (\%) \tag{1}$$

Here C_a and C_g is the sensor conductance in air and gas environment respectively. The response time was taken as the time required for sensor conductance to reach 90% of its equilibrium value after the gas was introduced in the test chamber and recovery time was measured as the time necessary for the sensor to regain 90% of its original value in the absence of gas. X-ray photoelectron spectroscopy (XPS) measurements were carried out using Mg K_α (1253.6 eV) source and a DESA-150 electron analyzer (Staib Instruments, Germany).The binding energy scale was calibrated to Au $4f_{7/2}$ line of 84.0 eV. From the XPS data, the surface composition (Ci) can be quantified using the following equation [4-6]:

$$C_i = (I_i/S_i)/\Sigma\,(I_i/S_i) \text{ where i = C, N, O and Zn.} \tag{2}$$

Here I_i represents the intensity of C, N, O and Zn is determined by finding the total area under the core level peak using the least-squares fitting of Gaussian line shape. S_i the atomic sensitivity factor and has values of C, N, O and Zn as 0.296, 0.477, 0.711 and 3.726 for C-1s, N-1s, O-1s and Zn-2p peaks respectively. The films were exposed to 25 ppm Cl_2 in the test chamber and XPS data were taken about 1 hour later.

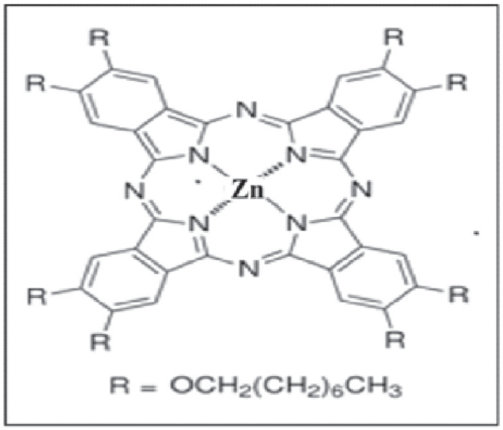

Fig 1. Chemical structure of substituted ZnPc molecule.

III. Results And Discussion

Figure 2(a) shows the uniformly grown network of substituted zinc phthalocyanine based nanowires (NWs) lying parallel to substrate surface.

The average diameter of NWs was 90 nm. The lateral growth of NWs can be attributed to the strong molecule substrate interactions and Π-Π interactions among phthalocyanine cores [6,7]. Figure 2(b) represents the XRD diffractogram of NWs with a diffraction peak at 5.4° due to inter-columnar order of phthalocyanine molecules [7]. Besides this, a broad diffraction band between 15° to 40° has also been observed which may be due to the reflection from glass substrate.

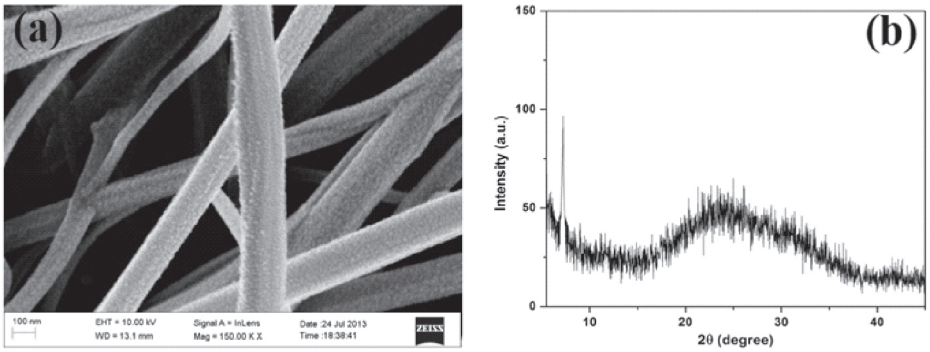

Fig. 2. (a) SEM image and (b) XRD pattern of NWs grown over glass substrate.

Now we shall discuss the room temperature (25^0c) gas sensing characteristics of NWs. It is well established that oxygen present in the ambient air get adsorbed on the phthalocyanine film surface, forming MPc^+ and O_2^- species which are responsible for p-type semiconducting nature of the film [4-6].

$$MPc + O_2 \rightarrow MPc^+ + O_2^- \qquad (3)$$

The presence of adsorbed oxygen (O^-_2) was confirmed from the binding energy peak at 533 eV in the XPS analysis of film sample [6]. We kept the NWs sensor in test chamber under a constant bias of 5V for few hours and the base line conductance of NWs was $4 \times 10^{-8}\ \Omega^{-1}$. Before studying the room temperature Cl_2 sensing characteristics of NWs sensor, we have exposed the sensor to 500 ppb of different gases (Cl_2, NO_2, NO and NH_3) to check its selectivity. Figure 3(a) shows the selectivity histogram of NWs sensor for different gases at room temperature. As seen in fig. 3(a), NWs sensor exhibited a higher response for Cl_2 while the response for NO_2, NO and NH_3 gases was comparatively much lower which confirmed the selectivity of NWs sensor for Cl_2 gas at room temperature. It has been observed that on exposing the sensor to Cl_2, there was a drastic increase in sensor conductance and it again started approaching its initial baseline value as soon as Cl_2 was shut off which showed the good reversibility of NWs sensor. Phthalocyanines are generally of electron donor nature and Cl_2 molecules are electron acceptors. Phthalocyanine film contained adsorbed oxygen (O_2^-) sites and free metal co-ordination sites [6]. Once the sensor was exposed to Cl_2, it replaced the adsorbed oxygen as well as got adsorbed at free metal co-ordination sites on the film surface as described by following reactions:

$$2MPc + Cl_2 \rightarrow 2MPc^+ + 2Cl^- \tag{4}$$

$$Cl_2 + 2O_2^- \rightarrow 2Cl^- + 2O_2 \tag{5}$$

In this way, Cl_2 took electrons from phthalocyanine film surface and increased the number of holes which resulted in the increase of sensor conductance. When we opened the lid of test chamber for recovery process, the adsorbed Cl_2 was replaced by the atmospheric oxygen due to its abundance in the surrounding and resulted in the lowering of sensor conductance. It is interesting to note that NWs sensor has detected Cl_2 concentration as low as 5 ppb with a response of 80%. It was observed that for 1500 ppb, the response of NWs sensor was 600% within 15 seconds. There was a monotonic increase in sensor response with increase in Cl_2 concentration as shown in figure 3(b).

In order to get information about the interaction between substituted ZnPc molecule and Cl_2, XPS analysis was carried out on the film samples before and after exposure to 25 ppm of Cl_2. The XPS spectra of Zn-2p, N-

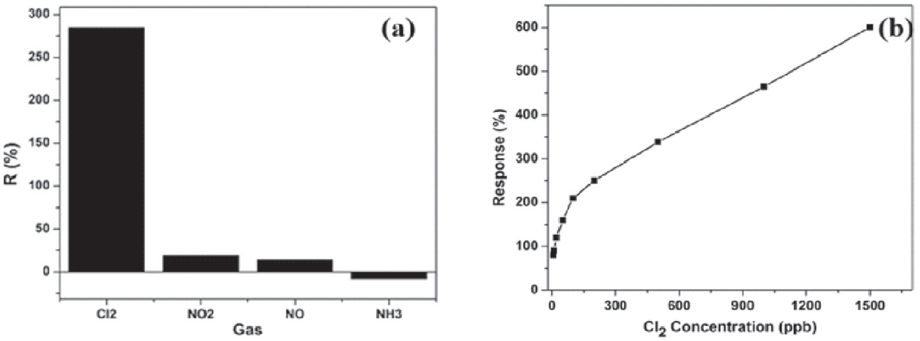

Fig. 3. (a) Selectivity histogram and (b) variation of NWs sensor response with Cl_2 concentration.

1s, O-1s and C-1s before and after exposure to 25 ppm of Cl_2 is shown in figure 4. The peak at 1022 and 1045 eV corresponds to the Zn-$2p_{3/2}$ and Zn-$2p_{1/2}$ level respectively. The peak at 286 eV and 399 eV corresponds to the core levels C-1s and N-1s while the peak at 533 eV represents the core O-1s level. There is no change in the spectrum of core level C-1s after gas exposure, so it rules out the possibility of gas reaction at carbon sites whereas O-1s peak shows a shift of 0.4 eV. But the major changes in the XPS spectrum occurred at Zn-2p peak with a shift of 0.6 eV towards higher BE side (i.e. decrease in electron density which indicates that the electrons are being transferred from ZnPc molecule to Cl_2). So it was evident that central Zn ions were the predominant sites for Cl_2 interaction. Since zinc ions were directly connected to nitrogen atoms hence a similar shift was observed in N-1s peak after Cl_2 exposure.

In conclusion, we have fabricated a low cost, highly sensitive and Cl_2 selective sensor based upon substituted ZnPc nanowires and studied its response kinetics as well as Cl_2 sensing mechanism.

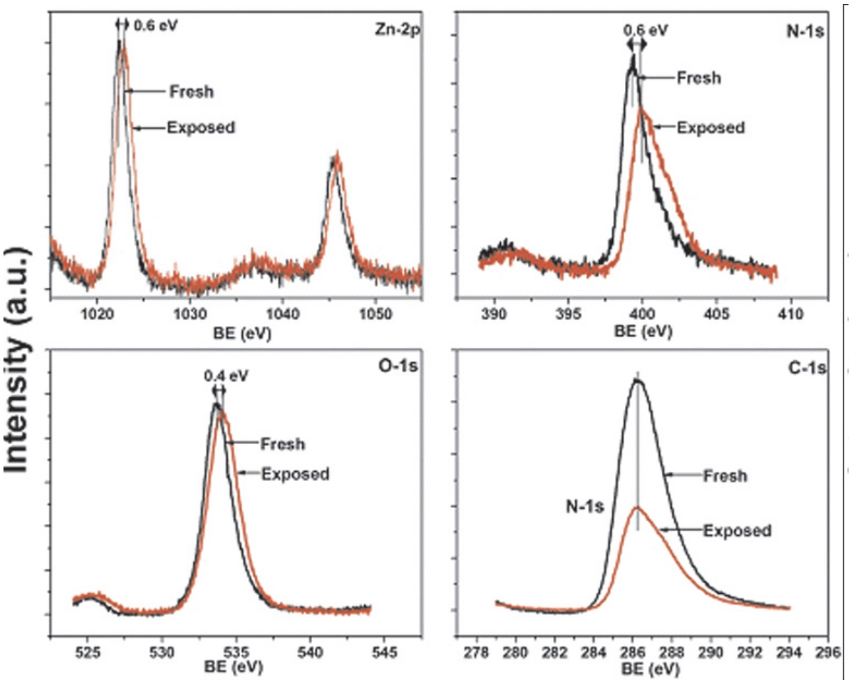

Fig. 4. XPS spectrum of Zn-2p, N-1s, O-1s and C-1s peaks of substituted ZnPc molecule recorded before and after exposure to 25 ppm of Cl_2.

III. References

[1] F. S. Kim, G. Ren and S. A. Jenekhe, "One-dimensional nanostructures of conjugated molecular systems: assembly, properties, and applications from photovoltaics, sensors, nanophotonics to nanoelectronics" Chem. Mater. 23 (2011) 682-732

[2] G.J. Cadena, J. Riu and F.X. Rius, "Gas sensors based on nanostructured materials" The Analyst 132 (2007) 1083-1099.

[3] C. Zhang, Y. Yan, Y.S. Zhao and J. Yao, "Synthesis and applications of organic nanorods, nanowires and nanotubes" Annu. Rep. Prog. Chem., Sect C: Phys. Chem. 109 (2013) 211239.

[4] L. Zang, Y. Che and J.S. Moore, "One-dimensional self-assembly of planar-conjugated molecules: adaptable building blocks for organic nanodevices" Acc. Chem. Res. 41 (2008) 15961608.

[5] Rajan Saini, A. Mahajan, R.K. Bedi, D.K. Aswal and A.K. Debnath, "Phthalocyanine based nanowires and nanoflowers as highly sensitive room temperature Cl_2 sensors" RSC Advances 4 (2014) 1594515951.

[6] Rajan Saini, A. Mahajan, R.K. Bedi, D.K. Aswal and A.K. Debnath, "Solution processed films and nanobelts of substituted zinc phthalocyanine as room temperature ppb level Cl_2 sensors" Sensors and Actuators B 198 (2014) 164172.

[7] Gema de la Torre, C.G. Claessens and T. Torres, "Phthalocyanines: old dyes, new materials. Putting color in nanotechnology" Chem. Comm. (2007) 2000-2015.

Guidelines For Author(s)

Title

The title must be in Times New Roman Font 14 size in running characters.

Author (s) Names and Affiliation

The Author(s) Names must be in Times New Roman Font 10 size with affiliations and e-mail address of the corresponding author. The affiliations of authors from different institutions must be superscript with small alphabets.

Abstract

The Abstract should be written in Times New Roman Font size 12 in italics followed by 4-5 key words

Text of Paper

The text of paper must be typed in MS Word in single column in Times New Roman Font size 12 in running characters. The page size must be The titles (Introduction, Experimental, Results, Conclusions etc.) will be in bold and numbered in Capital Roman numerals (e.g. I, II, III etc). The subtitles will be numbered with bold capital alphabets (e.g. A, B, C, etc.)

Figure Captions

The figure captions should be typed in font size 10 in italics

(e.g. Fig. 1 XRD diffractogram of decomposed samples)

Table captions:

The table captions should be typed in font size 10 in italics

(e.g. Table 1 Selected characteristic population studies)

Reference Style

The following reference style must be adopted

[1] M. Abdel Rafea, N. Roushdy, "Determination of optical band gap for amorphous and nanocrystalline copper oxide thin films prepared by SILAR technique@, J. Appl. Phys. D, 42(2009)15413

[2] F. Zumpt, " Myiasis in man and animals in the old world", Butterworth (1965) 267.

Peer Review and Publication Policy

- The double blind peer review process has been adopted where both reviewers and authors remain anonymous throughout the review process.
- The research articles are selected through highest quality peer review. The entire peer review and publication process is thorough, objective and fair.
- An initial review of each article submitted for publication is done by an editor.
- The article is sent to the reviewer if it meets with a minimum standard. It is ensured that the reviewer does not know about the identity of the author.
- The comments of the reviewer are sent to the author after making them anonymous to ensure that the author also does not know about the identity of the reviewer.
- The Editorial Board makes a decision on the acceptability of the manuscript based on the reviewers' comments and communicates to the authors the decision, along with referees' reports.
- If significant revisions are proposed, the author is asked to resubmit the paper after incorporating the revisions.
- The paper is again sent to the reviewer for his comments. The final decision on the acceptance is dependent on whether the author has incorporated the suggested revisions satisfactorily and the final comments of the reviewer.
- The journal strongly discourages the act of plagiarism. The author is black listed if found guilty of plagiarism or Self-Plagiarism.
- The Journal follows the COPE guidelines for Retraction of articles: It Can be found at following link:
  http://publicationethics.org/files/retraction%20guidelines.pdf

Ethics Policy

- The journal subscribes to the standards of expected ethical behaviour.
- It must be ensured by the authors that the research articles submitted by them are entirely their original works. The work/or words of others used by the authors should be appropriately cited or quoted.
- In cases of proven scientific misconduct, plagiarism, or fraudulent publication, the appropriate action will be taken.
- The journal may ask the authors to provide the raw data in connection with a paper for editorial review.
- An author should not in general publish manuscripts describing essentially the same research in more than one journal.
- Proper acknowledgment of sources
- Statements of compliance are required if the work involves chemicals, procedures or equipment that have any unusual hazards inherent in their use, or if it involves the use of animal etc.
- The editors will not disclose information about a submitted manuscript to anyone other than the corresponding author, reviewers or potential reviewers, or other members of the editorial board.
- Manuscripts received for review will be treated as confidential documents and not shown or discussed with other without authorization from the editors.
- If an author discovers a significant error in the published work, the author is obligated to inform the journal editor in order to either correct or retract the paper.